Master Thesis

CFD Study of Piston Cooling Using Oil Jets

Vishal Venkatesh

Technische Universiteit Delft

TU Delft Delft University of Technology

Challenge the future

Master Thesis

CFD Study of Piston Cooling Using Oil Jets

by

Vishal Venkatesh

in fulfillment of the requirements of the course
AE5110 Thesis Aerodynamics and Wind Energy,

as a part of the degree of
Master of Science in Aerospace Engineering

at the Delft University of Technology.

Student number:	4724178
Project duration:	Nov 09, 2018 - July 05, 2019
Supervisors:	Dr. Stefan Hickel, TU Delft
	Dr. Jemil Znaien, DAF Trucks N.V.
Thesis Committee:	Dr. S.J. Hulshoff, TU Delft
	Dr. A.G. Rao, TU Delft
	Dr. ir. J.W.R. Peeters, TU Delft

Acknowledgement

This research work has provided me with great opportunities and experiences to grow and improve myself academically and personally. It would not have been possible without the guidance of my daily supervisor, Dr. Jemil Znaien at DAF. I had the freedom to work autonomously and his timely suggestions were invaluable. His patience in providing feedback to make my report better is highly appreciated. I would also like to thank my other supervisor, Dr. Stefan Hickel for providing critical and helpful inputs during different stages of this research. I express my gratitude to DAF Trucks N.V. for giving me this opportunity as a student researcher.

I am also indebted to my parents Viji and Venkatesh whose struggles and sacrifices have led me to where I am, and I take this opportunity to thank them for everything. I also would like to thank my life companion, Sneha Ravisankar for the constant support and encouragement throughout this period. I owe this accomplishment to everyone of them.

Vishal Venkatesh.

Abstract

For heavy duty diesel engines, piston temperature control is very important in constructing a successful design that meets the demands of increasing power output and stringent emission regulations. Overheating of piston is avoided with engine oil through spray cooling and gallery cooling processes. In this research project, evolution and disintegration of oil jet used for piston cooling by DAF Trucks N.V., is studied numerically using Large Eddy Simulation (LES) and Volume of Fluid (VOF) methodologies. A robust CFD model is built with major focus on the significance of grid resolution in multi-phase LES, and is used to reproduce two test cases. This is followed by characterization of physics involved in oil jet breakup through qualitative inspection. Parameters relevant to the two types of cooling techniques are estimated to see the impact of jet development at different flow rates. Based on the results obtained, the need for grid refinement is assessed and performed for certain cases. Finally, turbulent atmosphere within the crankcase is estimated through a separate simulation and its effect on oil jet is investigated. Results show that for oil in quiescent atmosphere jet turbulence is the dominant force and is the primary cause for disintegration. A clear transition to turbulence is captured with increase in flow rate, as the jet behavior is more and more chaotic with droplet formation and spreading. Importance of grid resolution on droplet capturing is recognized and an isolated analysis shows more droplets being captured with fine meshes. The level of refinement necessary to capture all the droplets still remains an open question. With turbulent atmosphere, no significant change in the jets is obtained until primary breakup and the inertial force of the liquid phase is found to dominate the surrounding flow effects. However, secondary breakup is found to be affected, as aerodynamic interactions increase disintegration and spreading, impacting both the cooling techniques. Results obtained from this research work will be used as primary inputs for further studies in the company on spray cooling and gallery cooling (sloshing flow) leading towards optimization of the piston cooling process.

Contents

Abstract **v**

List of Figures **xi**

List of Tables **xv**

Nomenclature **xv**

1 Introduction **1**
1.1 **Problem description** . . . 1
1.2 **Previous research** . . . 2
1.3 **Research questions/objectives** . . . 5
1.4 **Structure of the report** . . . 6

2 Literature review **7**
2.1 **Liquid Jet Breakup** . . . 7
2.1.1 **Free-surface liquid jet breakup** . . . 7
2.1.2 **Quantities of interest** . . . 8
2.1.3 **Breakup regimes** . . . 9
2.1.4 **Effect of aerodynamics** . . . 10
2.1.5 **Importance of Weber Number** . . . 11
2.1.6 **Breakup length correlations** . . . 11
2.1.7 **Droplets and ligaments** . . . 11
2.1.8 **Computational modeling of liquid jet breakup** . . . 12
2.2 **Crankcase Turbulence** . . . 19
2.2.1 **Source and nature of crankcase flow** . . . 19
2.2.2 **Crankcase ventilation** . . . 19
2.2.3 **Other Dynamics within the crankcase** . . . 20
2.2.4 **Bay-to-bay breathing effect on pressure variation** . . . 20
2.2.5 **Computational models** . . . 21
2.3 **Liquid jet in turbulent atmosphere** . . . 24
2.3.1 **Effect of co-axial flow on liquid jets** . . . 24
2.3.2 **Effect of cross-flow on liquid jets** . . . 25
2.3.3 **Estimation of surrounding flow's impact on piston cooling** . . . 26

3 Validation **29**
3.1 **Description of test cases** . . . 29
3.1.1 **Test case - 1 (Turbulent water jets)** . . . 29
3.1.2 **Test case - 2 (Flow rate efficiency experiment-DAF)** . . . 30
3.2 **Computational setup** . . . 31
3.2.1 **Geometry and meshing** . . . 31
3.2.2 **Boundary conditions** . . . 34
3.2.3 **Physics models and solver settings** . . . 36

3.3 **Validation of test case - 1** . . . 36
3.3.1 **Initialization and sampling** . . . 36
3.3.2 **LES Quality assessment** . . . 36
3.3.3 **Qualitative results - Jet structure** . . . 38
3.3.4 **Quantitative results** . . . 39
3.4 **Validation of test case - 2** . . . 41
3.4.1 **Modifications to the numerical setup** . . . 41
3.4.2 **LES quality assessment** . . . 42
3.4.3 **Flow rate efficiency results** . . . 44
3.5 **Conclusion** . . . 44

4 Oil jet characteristics **47**
4.1 **Typical characteristics** . . . 47
4.2 **Evolution pattern** . . . 50
4.2.1 **Laminar Jet** . . . 50
4.2.2 **Transitioning jets** . . . 50
4.2.3 **Turbulent Jet** . . . 52
4.3 **Droplet size results** . . . 55
4.3.1 **6 L/min** . . . 55
4.3.2 **7 L/min** . . . 56
4.4 **Assessment of grid resolution** . . . 58
4.5 **Small domain analysis** . . . 60
4.5.1 **Modified geometry** . . . 60
4.5.2 **Grid refinement** . . . 60
4.5.3 **Results** . . . 62
4.6 **Conclusion** . . . 68

5 Effect of turbulent atmosphere on piston cooling jets **71**
5.1 **Crankcase turbulence** . . . 71
5.1.1 **Computational setup** . . . 71
5.1.2 **Results** . . . 76
5.1.3 **Estimation of effect of surrounding flow on oil jets** . . . 79
5.2 **LES of oil jets in turbulent atmosphere** . . . 79
5.2.1 **Computational setup** . . . 79
5.2.2 **Qualitative results - 7 L/min** . . . 80
5.2.3 **Quantitative results - 7 L/min** . . . 81
5.2.4 **Results for oil at 3 L/min and 5 L/min** . . . 83
5.3 **Conclusions** . . . 85

6 Conclusions **87**
6.1 **Validation and oil jet characteristics** . . . 87
6.2 **Assessment of grid resolution** . . . 88
6.3 **Oil jet in turbulent atmosphere** . . . 88
6.4 **Engineering perspective** . . . 89

7 Recommendations for future work **91**
7.1 **Present work** . . . 91
7.2 **Future work** . . . 92

Bibliography **95**

A Scalability results **101**

B Precursor simulation **103**

C LES Quality results **105**

D Summary of Jet characteristics **109**

List of Figures

1.1 Flow chart showing the components of piston cooling . . . 2
1.2 Oil jet results obtained by Celik using LES-VOF [3] . . . 3
1.3 Impingement models used by Celik (a) 2D model schematic, (b) 3D model geometry and (c) Quasi-dynamic implementation of piston motion [3] . . . 4

2.1 Classification of breakup regimes for liquid jets [29]. . . . 9
2.2 Typical characteristics of jets in corresponding regimes [30]. . . . 10
2.3 CFD of single-phase jet using different turbulence modelling approaches [46]. . . . 15
2.4 Typical LES approach of scale separation [47] . . . 15
2.5 Illustration of (a) unsuitable grid and (b) suitable grid for two-phase VOF [41] . . . 17
2.6 Typical blow-by from combustion chamber [60] . . . 20
2.7 (a) Isometric view and (b) Cross-sectional view of PACCAR's MX-11 engine. Figures showing the geometric variations within and in-between the cylinders . . . 21
2.8 Typical pressure variation in a cycle by Fogliarino [63] . . . 21
2.9 Overset mesh schematic [71] . . . 23
2.10 Axisymmetry modulations due to KH instability where λ is the wavelength of disturbance[78] . 24
2.11 Rayleigh-Taylor instability on jet surface [78] . . . 25
2.12 Schematic of liquid jet in cross-flow [82] . . . 25

3.1 DAF experimental setup[85]. . . . 30
3.2 Flow rate efficiency results for 6 different PCJ nozzles [3]. . . . 30
3.3 Three dimensional domain used for oil jet simulation . . . 31
3.4 Two dimensional schematic of the domain with dimensions . . . 31
3.5 2D mesh schematic of grids tested within the nozzle . . . 33
3.6 Wall y^+ results obtained for (a) Grid - 1 and (b) Grid - 2. . . . 33
3.7 (a) Velocity profile and (b) Turbulent kinetic energy within the nozzle . . . 34
3.8 (a) Velocity profile and (b) Turbulent kinetic energy within the nozzle . . . 34
3.9 (a) 2D view of the mesh with fine mesh in the jet region and growing mesh outside and (b) Jet region - here grid sizes from Table 3.1 are used . . . 35
3.10 Initialization and sampling stages for validation of test case - 1 . . . 37
3.11 LES quality metric (γ) results . . . 37
3.12 Turbulent viscosity ratio results . . . 38
3.13 Jet structure with different threshold iso-surfaces . . . 38
3.14 Jet structure obtained from LES analysis of test case - 1. . . . 39
3.15 Breakup length sampling. (Black) Instantaneous and (Red-dashed) Mean results . . . 40
3.16 Red dots indicating that the five tested flow rates lie in SWI regime . . . 42
3.17 Turbulent viscosity ratio for oil jet at 7 L/min . . . 43
3.18 LES quality metric (γ) results for oil jet at 7 L/min . . . 43
3.19 Flow rate efficiency validation. Present study (LES) vs DAF experiment (PCJ1 - PCJ6) . . . 44

4.1 Iso-surface for oil jet at 7 L/min (turbulent) . . . 48
4.2 Jet structure for all the tested flow rates . . . 49
4.3 Jet structure at 3 L/min. Two zones are observed and highlighted . . . 51
4.4 Undisturbed and sinuous wave zones for all flow rates corresponding to the transition regime . 52

4.5 Pre-breakup zone for all transitioning jets . . . 53
4.6 Jet structure at 7 L/min. . . . 54
4.7 Piston positions chosen for droplet size quantification, where S is the stroke length . . . 55
4.8 Droplet size results for 6 L/min at TDC, (a) PDF and (b) CDF . . . 55
4.9 Droplet size results for 7 L/min at BDC, (a) PDF and (b) CDF . . . 56
4.10 Droplet size results for 7 L/min at S/4, (a) PDF and (b) CDF . . . 57
4.11 Droplet size results for 7 L/min at S/2, (a) PDF and (b) CDF . . . 57
4.12 Droplet size results for 7 L/min at 3S/4, (a) PDF and (b) CDF . . . 57
4.13 Droplet size results for 7 L/min at TDC, (a) PDF and (b) CDF . . . 58
4.14 (a) Grid required to capture actual droplets and (b) Coarse grid inducing numerical droplet coalescence . . . 59
4.15 (a) Isometric view of the small domain with boundary conditions and (b) 2D schematic of the geometry . . . 60
4.16 Converged results from full LES mapped onto the small domain at a position well ahead of BDC 61
4.17 Schematic of different meshes constructed for present analyses . . . 61
4.18 Jet structure obtained with the small domain for oil at 7 L/min at BDC . . . 62
4.19 Jet structure obtained with the small domain for oil at 7 L/min at S/2 . . . 62
4.20 Jet structure obtained with the small domain for oil at 7 L/min at TDC . . . 63
4.21 Jet structure obtained with the small domain for oil at 3 L/min with Grid - 1 . . . 64
4.22 Jet structure obtained with the small domain for oil at 3 L/min with Grid - 3 . . . 64
4.23 Jet structure obtained with the small domain for oil at 5 L/min with Grid - 1 . . . 64
4.24 Jet structure obtained with the small domain for oil at 5 L/min with Grid - 3 . . . 65
4.25 % of cells with poor LES quality for jet at 7 L/min, for the three grids . . . 65
4.26 Instantaneous LES quality metric results . . . 66
4.27 Mean droplet diameter variation for the three grids . . . 67
4.28 Droplet size PDF comparison near TDC for the three tested grids. . . . 68

5.1 MX-11 engine block and sump . . . 72
5.2 (a) Original MX-11 piston geometry and (b) Simplified piston surface for the present analysis . . 72
5.3 (a) Isometric view and (b) sectional view of the simplified final geometry with cylinder numbers 73
5.4 Sectional view of the structured grid used for present analysis . . . 73
5.5 Piston velocity input data . . . 74
5.6 Modified geometry with inlet and outlet attachments . . . 75
5.7 Pressure measurement locations . . . 75
5.8 Mesh sensitivity analysis results . . . 76
5.9 Pressure fluctuation as a function of Crank angle, in (a) cylinder 1, (b) cylinder 2 and (c) cylinder 3 77
5.10 (a) Planes constructed for estimating breathing effect and (b) mass flow rate across these planes 77
5.11 Velocity components versus crank angle in cylinder (a) 1, (b) 2 and (c) 3. (Change picture to matlab format) . . . 78
5.12 Oil jet at 7 L/min (a) in Quiescent atmosphere, (b) with co-axial flow and (c) with counter-axial flow . . . 81
5.13 Oil jet at 7 L/min near TDC (a) in Quiescent atmosphere, (b) with co-axial flow and (c) with counter-axial flow . . . 82
5.14 Comparison of flow rate efficiencies for the three different surrounding flow conditions . . . 82
5.15 Comparison of mean droplet sizes for the three different surrounding flow conditions . . . 83
5.16 Oil jet at 3 L/min (laminar) (a) in Quiescent atmosphere and (b) with counter-axial flow . . . 84
5.17 Oil jet at 5 L/min (Transitioning) (a) in Quiescent atmosphere and (b) with counter-axial flow . 85

6.1 Piston cooling study at DAF split into previous, present and future work . . . 87

A.1 Precursor simulation geometry [3] . . . 101

B.1 Precursor simulation geometry [3] 103
B.2 Mesh schematic used for precursor simulation 104

C.1 LES quality metric (sufficient condition) for oil jet at (a) 3 L/min and (b) 4 L/min 105
C.2 LES quality metric (sufficient condition) for oil jet at (a) 5 L/min and (b) 6 L/min 106
C.3 Turbulent viscosity ratio (necessary condition) for oil jet at (a) 3 L/min and (b) 4 L/min 106
C.4 Turbulent viscosity ratio (necessary condition) for oil jet at (a) 5 L/min and (b) 6 L/min 107

List of Tables

2.1 Operating conidtion of DAF's piston cooling jets . . . 10
2.2 Sample calculation of liquid-to-gas momentum ratio (M) . . . 26

3.1 Mesh settings in the jet region, and total cell count . . . 32
3.2 Mesh settings for testing the effect on nozzle flow . . . 33
3.3 Breakup length results . . . 40
3.4 Droplet size results - normalized with nozzle diameter . . . 41
3.5 Engine oil (10W-30) properties at 100°C . . . 41
3.6 Jet characteristics at different flow rates . . . 42
3.7 Time step used and CFL number for different flow rates . . . 42
3.8 % of cells with poor quality in the jet region according to sufficient condition . . . 43

4.1 Droplet diameter statistics at 6 L/min . . . 56
4.2 Droplet diameter statistics at 7 L/min . . . 58
4.3 Cells size used for meshing the small domain . . . 61
4.4 Mean diameter results at local piston positions . . . 67

5.1 PACCAR MX-11 engine specification . . . 72
5.2 Liquid to gas momentum ratio for different liquid flow rates . . . 79
5.3 Flow rate efficiency at BDC. Results in comparison with quiescent atmosphere case . . . 80
5.4 Droplet sizes at BDC. Results in comparison with quiescent atmosphere . . . 80

D.1 Characteristics of the laminar jet, at 3 L/min . . . 109
D.2 Characteristics of transitioning jet, at 4 L/min . . . 109
D.3 Characteristics of transitioning jet, at 5 L/min . . . 110
D.4 Characteristics of transitioning jet, at 6 L/min . . . 110
D.5 Characteristics of turbulent jet, at 7 L/min . . . 111

Nomenclature

Abbreviations

BDC	Bottom Dead Center
CFD	Computational Fluid Dynamics
DNS	Direct Numerical Simulation
FR	Flow rate
KH	Kelvin-Helmholtz
LES	Large Eddy Simulation
OP	Operator
PCJ	Piston Cooling Jets
POI	Particle of Interest
$RANS$	Reynolds Averaged Navier-Stokes
RST	Reynolds Stress Tensor
RT	Rayleigh-Taylor
SEM	Synthetic Eddy Method
SGS	Sub Grid Scales
SMD	Sauter Mean Diameter
SST	Shear Stress Transport
TDC	Top Dead Center
TKE	Turbulent Kinetic Energy
TVR	Turbulent Viscosity Ratio
VOF	Volume Of Fluid

List of symbols

$°C$	Degree Celsius
Δ	LES cut-off scale
δ	Kronecker delta
ϵ	Rate of dissipation of turbulent kinetic energy
η	Flow rate efficiency
γ	LES Quality metric

λ	Wavelength of disturbance
μ	Dynamic viscosity
ν	Kinematic viscosity
ω	Specific dissipation of turbulent kinetic energy
ρ	Density
σ	Surface Tension
τ^r	Residual stress tensor
$C_m \; and \; C_r$	Empirical parameters
d	Nozzle Diameter
d_{drop}	Droplet diameter
d_w	Dimensional distance from the wall
E	Total Energy
F	Function used in VOF model
f	Body force
h	LES grid size
K	Heat Conduction
K	Kelvin
k	Kinetic energy of turbulent scales
kpa	kilo-pascal
L_c	Liquid core length
Oh	Ohnesorge number
p	Pressure
pa	Pascal
q	Flux of any flow variable like velocity, momentum or energy
Re	Reynolds number
S	Stroke length
t	Time
u	velocity
$u*$	Friction velocity
V_x	x-component of velocity
V_y	y-component of velocity
V_z	z-component of velocity

We	Weber number
x	x-coordinate (Jet flow direction)
y^+	Dimensionless wall distance

Subscripts and superscripts

g	Gas phase
$i,\ j$	Einstein convention
L	Liquid phase
max	Maximum
min	Minimum
r	Residual
SGS	Sub grid scales
w	Wall

1

Introduction

Heavy duty diesel engines are widely used as an efficient power source, primarily for road vehicles that transport consumer goods and commercial vehicles. These engines are preferred over gasoline engines because of higher power output, durability and reliability [1]. Present research in diesel engine technology is driven toward high efficiency due to the continuous demand for improvement in fuel economy, and eco-compatible designs to meet stringent emission regulations. This has resulted in significant escalation in cylinder pressures, and hence the power density [2], increasing the need for proper thermal management of various engine parts.

One such part that is actively involved in combustion and is non-stationary, is the piston. Close to 60% of the heat from fuel energy can be passed through its surface during operation. This will lead to premature wear and subsequent engine damage if the piston remains uncooled [3, 4]. Thus, its maximum temperature has to be controlled. Apart from structural failure, consequences of improper thermal management of the pistons also include increased NO_x and PM emissions, and greater power consumption [3].

Standard engine cooling methods cannot be used for pistons due to their dynamic nature. Typically, engine oil is used to cool piston surfaces from underneath. This technology has been employed at DAF Trucks through spray/splash cooling and gallery cooling for over 30 years. However, apart from the understanding that such a technique is required to prevent engine failure, there is limited knowledge at the company about the physics involved in this process. The atmosphere, into which oil is injected, is multi-phase and is in constant motion due to various moving components within the crankcase. Presence of such a complex flow field makes conduction of experiments difficult and expensive. Computational Fluid Dynamics (CFD) offers a much more practical and less expensive way to gain better insight about piston cooling, and therefore, the main goal of this research work is to perform comprehensive investigation on the cooling technique using CFD with *StarCCM+ 13.06*.

In this project, piston cooling is divided into several sub-problems based on the physics involved, and the investigations conducted aim at covering the first part extensively. Results of these analyses will serve as main inputs for further studies on the remainder of the piston cooling technique, as discussed in the recommendations chapter of this report. Following sections delineate the problem description, previous research conducted at the company, research questions/objectives of the present work, and the structure of the entire report.

1.1. Problem description

In general, piston cooling process consists of oil jets issued in air which travel a certain distance within the crankcase before reaching the piston surface. Then, a part of the oil enters the gallery enabling gallery

cooling, and the rest splashes on to the under-crown of the piston permitting splash/spray cooling. In the first technique, oil circulates in the gallery and cools piston from the inside. Reciprocating motion of the piston creates sloshing flow and generates turbulence within the gallery augmenting heat removal from the piston surface [3]. In the second technique, cooling is done by hitting (splashing) the hot surface with cold oil [3, 4]. Depending on flow rate and the type of flow development within the crankcase, oil may impact the piston surface as a contiguous stream analogous to liquid jet impingement, or, a disintegrated stream leading to spray impingement. This complex cooling process can be studied by isolating different physics involved as shown in the Fig. 1.1.

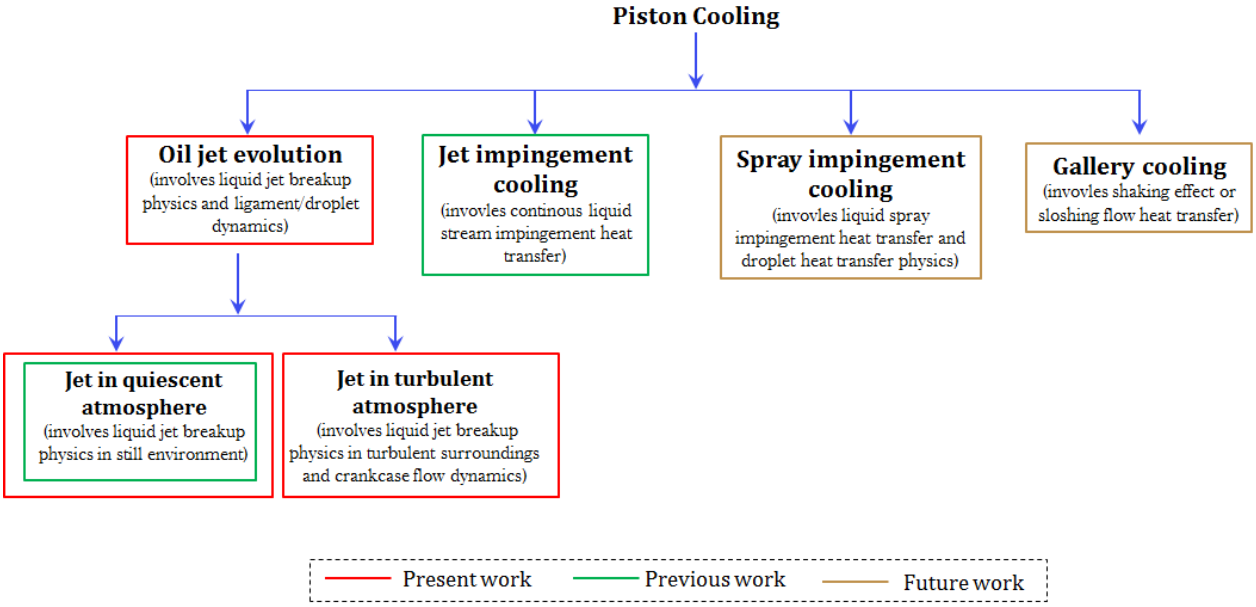

Figure 1.1: Flow chart showing the components of piston cooling

This project covers the first sub problem extensively. Since oil is injected into a gas medium, corresponding jets fall under the category of free-surface liquid jets [3, 5]. Emanating from a nozzle, a free-surface liquid jet can breakup to form ligaments and droplets, and spread en-route to the piston surface in a quiescent atmosphere. These characteristics will affect the amount of oil entering the gallery influencing gallery cooling process, and also the spray properties for splash/spray cooling technique. Further complication in real configurations is the dynamic environment in the crankcase due to reciprocating pistons. This makes the atmosphere turbulent, and may alter the breakup mechanism by modifying the jet structure. Thus, only by understanding the physics and governing forces involved in jet evolution at different operating conditions, impact on both the cooling techniques can be estimated. From an engineering standpoint, this will help in optimizing the process, leading to efficient usage of engine oil. As mentioned previously, due to the complexities and costs related to conduction of experiments, the approach of using computational methods (CFD) is followed in the present study.

1.2. Previous research

The present work is a continuation of previous research performed by Halil I. Celik at the company [3]. His study is the first CFD analysis on piston cooling at DAF and thus, a fundamental approach was opted for with simplified analyses using *StarCCM+ 12.02*. In this section, results obtained and limitations associated with the study are summarized.

Firstly, Celik isolated different sub-problems of piston cooling similar to Fig. 1.1, and studied oil jet evolution in quiescent atmosphere elaborately using combinations of RANS-VOF and LES-VOF methodologies.

Investigations using RANS showed the inability of RANS-VOF combination to reproduce realistic results as the jet remained unbroken. This was attributed to the tendency of the VOF method to maintain a sharp interface between the two phases whereas RANS gives mean properties of the flow that are not separated by such an interface [3]. This paved the way for analysing oil jets using Large Eddy Simulation (LES) which is rarely used in industries, and his work was the first attempt on LES within the company. He built a very simple model, and was hindered by the limited amount of literature on multi-phase LES in these operating conditions. With LES-VOF combination, typical overall jet characteristics such as spreading, disintegration, initial ligament and droplet formation, and the amount of oil entering the gallery orifice, were captured appreciably. An example of his results is shown in Fig. 1.2. Using this model, several trend analyses to test the effect of flow rate, oil temperature and nozzle diameter [3], were performed. The main limitation associated with this CFD model was the insufficient grid resolution for multi-phase LES involving very small droplets. The grid size used by Celik, does not allow capturing liquid structures of all sizes that are present in actual flow conditions. Shortcomings associated with the then version of StarCCM+, lacked availability of any specific methods for droplet size estimation and hindered the possibility of testing the effect of grid resolution. Also, one of his validation materials is not completely reliable and these are discussed further in section 3.2. Qualitative results from his analysis conform with literature in terms of increasing chaotic behaviour of the jets with increasing oil flow rates. However, the dominant mechanism identified to be responsible for the observations was cited as the aerodynamic drag, and this differs from the inferences cited in literature. Accuracies associated with the quantities were obtained in an unsatisfactory manner, and further discussions on these issues are mentioned in this report, initially in sections 2.1.3 and 2.1.4, and also addressed as part of the results in chapter 4.

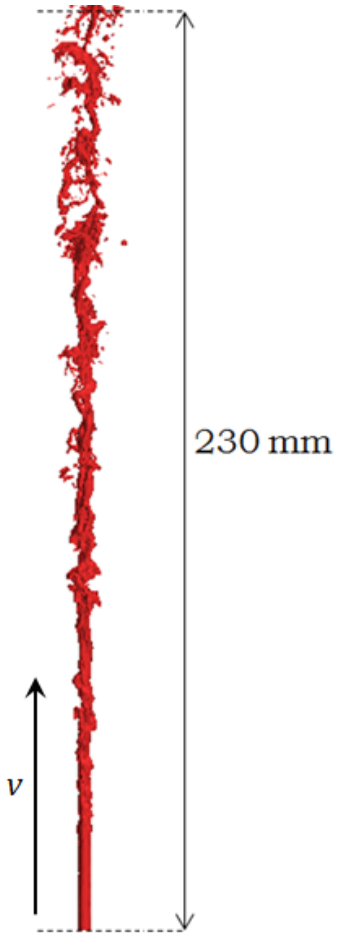

Figure 1.2: Oil jet results obtained by Celik using LES-VOF [3]

Celik also conducted preliminary investigations on jet impingement using RANS. A 2D model, as shown in Fig. 1.3 (a), was constructed and validated, and some trend analyses were performed to study oil jet impingement cooling. Although, accurate heat transfer characteristics were obtained, the model assumes the jet to be axisymmetric which is not true at all flow rates. Later, this issue was addressed with a 3D model (Fig. 1.3 (b)) with which spray cooling was also studied. However, the analyses lack proper implementation of jet characteristics obtained from LES. Only sampled volume fraction and velocity data obtained at definite piston locations were fed as inputs to study the heat transfer of sprays, and no information was given to represent ligament/droplet properties at corresponding flow rates. To add to these limitations, the effect of turbulent atmosphere due to piston motion was not accurately accounted for in the study. Although, some initial analysis with quasi-dynamic approximations were done (Fig. 1.3 (c)), Celik recommends the need for better models to determine the surrounding flow properties [3].

Based on this summary, the present research work is mainly aimed at constructing a better LES model, using *StarCCM+ 13.06*, with improved grid resolution, make better validation, estimate the force(s) that dominate(s) jet characteristics and quantify droplet sizes for spray cooling studies. Similar analysis is extended to oil jet in turbulent atmosphere where the surrounding flow properties are estimated with a separate CFD model. More detailed explanation of research questions and steps involved are given in the following section.

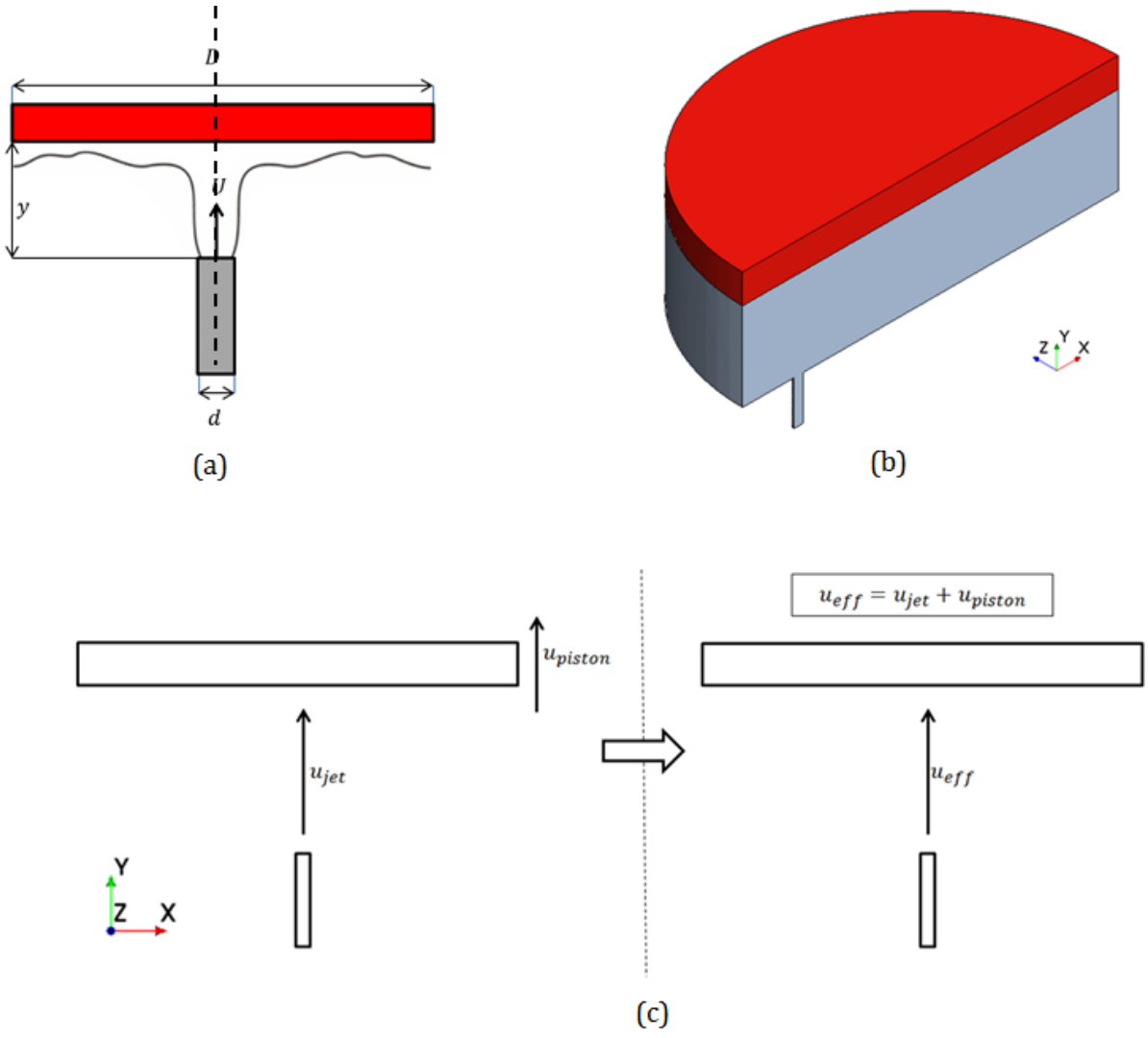

Figure 1.3: Impingement models used by Celik (a) 2D model schematic, (b) 3D model geometry and (c) Quasi-dynamic implementation of piston motion [3]

1.3. Research questions/objectives

Objectives of the present work can be split up into following research questions. Steps to be taken during the search for their answers are listed alongside.

Q1: What are the important variables for constructing a robust CFD model for multi-phase LES simulations?

- Identify appropriate LES grid resolution and its impact on droplet capturing,
- Optimize grid construction based on permissible refinement with respect to the computational constraints at the company and time available for the study,
- Identifying parameters for estimating the quality of simulations, and
- Performing validation using research from literature with closest match and tests performed within the company.

Q2: How is breakup affected with change in oil flow rates?

- Qualitatively assess the jet structure and spreading behaviors and
- Identify the main forces responsible for breakup (dominant mechanism).

Q3: What is the impact of oil jet breakup on gallery cooling and spray cooling?

- For gallery cooling,
  - Quantify oil flow rate entering the cooling gallery with respect to inlet flow rate, locally - at different piston locations such as Bottom Dead Centre (BDC) and Top Dead Centre (TDC).
- For spray/splash cooling,
  - Quantify local droplet/ligament sizes,
  - Quantify effect of grid resolution on droplet sizes, and
  - Compare oil jet disintegration to spray cooling.

Q4: How does crankcase pressure/velocity fluctuations impact the entire process?
Due to reciprocating motion of the piston, pressure and velocity within the crankcase fluctuate within a cycle.

- Predict the pressure/velocity amplitude through another isolated simulation of crankcase with URANS, and
- Using these results as boundary conditions, study oil jet behavior and perform analysis similar to the steps mentioned in Q2 and Q3.

The research objective is to understand the working principle of piston cooling in terms of jet breakup using the CFD model. Also, the aim is to estimate the consequential impact on cooling performance through qualitative and quantitative assessment of pertinent parameters, as mentioned above. Results obtained from the present study will be used for future works within the company, to bridge the knowledge gap in the facets of spray cooling/droplet impingement heat transfer and gallery cooling (sloshing flow). With this and the follow-up studies, the cooling process can be proficiently optimized by identifying ideal flow rates, and hence, suitable pumping pressures. This will eventually lead to efficient usage of engine oil, reduction in pumping power and a much better thermal management of piston surfaces improving fuel efficiency and aiding the company to meet customer demands of increased output power.

1.4. Structure of the report

Literature review related to various sub problems considered in this project is presented in detail in chapter 2. This is followed by construction and validation of the CFD model, for simulating piston cooling jets in quiescent atmosphere, in chapter 3. An intensive analysis on structure of oil jets and quality of the LES model is discussed using qualitative and quantitative results in chapter 4. Then, an analysis on turbulent atmosphere within the crankcase is performed and its effect on oil jets is investigated in chapter 5. Finally, conclusions and recommendations for further studies are presented in chapter 6 and 7 respectively.

2

Literature review

This chapter presents an overview of literature and past research relevant to the various sub problems of this project. Corresponding computational models required for performing CFD analysis of the problem are also outlined. First, theoretical description and concepts involved in CFD modelling of liquid jet breakup are presented in section 2.1. This is followed by literature on crankcase turbulence in section 2.2. The chapter concludes with a brief description of liquid jets in turbulent atmosphere in section 2.3.

2.1. Liquid Jet Breakup

This section consists of extensive literature review regarding the physics of liquid jet breakup. Through this study, important mechanisms and parameters relevant for PCJ operating conditions are identified. After a brief description of early research on jet breakup process in section 2.1.1, the quantities of interest are presented in 2.1.2. Technical classification of breakup regimes is given in section 2.1.3. Effects of major forces involved, are discussed in sections 2.1.4 and 2.1.5 followed by some correlations in 2.1.6. Formation and evolution of ligament and droplet structures post disintegration are discussed in section 2.1.7. This is followed by theoretical description CFD models with their limitations in 2.1.8.

2.1.1. Free-surface liquid jet breakup

When a liquid is issued from a nozzle, disturbances form and grow on the jet surface leading to its disintegration [5]. This hydrodynamic instability of the liquid jet is a result of opposing cohesive and disruptive forces. Cohesive forces include surface tension and viscous forces; disruptive forces are turbulence of the jet, inertial forces, and aerodynamic interactions [6, 7]. Apart from these, nozzle diameter, aspect ratio, and surface roughness are also found to influence the breakup, especially for high-speed jets [5, 8].

Rayleigh [7, 8] was among the first to study this breakup process. According to his theory, an inviscid liquid jet becomes unstable under the action of surface tension when subjected to a disturbance of wavelength greater than circumference of the jet (Plateau-Rayleigh instability) [6, 9]. Effects of gravity and interaction with the ambient were neglected. Weber [11] included the effects of liquid viscosity and ambient density. He assumed that disturbances result only in rotationally symmetric oscillations on a jet. According to his theory, surface forces either mitigate or amplify the perturbations based on the wavelength of initial disturbance [5, 11]. Several researches extended these basic theories by incorporating effects of density ratios [12–15], high-velocity jet breakup [14–18], and droplet formation [13, 14, 19–21]

Early investigations on liquid jet breakup were done primarily with water as the working fluid. Post Rayleigh and Weber, several researchers performed stability analysis to identify the factors governing amplification of disturbances [6, 8, 17, 18, 22, 23]. Grant and Middleman [22] carried out experiments on distilled

water, glycerine-water and ethanol-water mixtures to identify the relation of breakup length and liquid properties. Phinney [17] attempted to apply the knowledge available on laminar jet breakup to turbulent jets using an electrical method of detecting the breakup points. Both studies concluded that, the onset of breakup was mainly affected by turbulence at the jet exit. Wu. et. al conducted a series of shadow graphic analysis with turbulent water jets over a wide range of Reynolds and Weber numbers [13, 14, 16, 24, 25]. Their phenomenological analysis on the onset of breakup and drop/ligament formation provides excellent insight into the physics behind the process [13, 16, 24]. Based on the operating conditions, they classify breakup as weakly turbulent breakup (Re ~ 2 x 10_3 – 5 x 10_3), turbulent breakup (Re ~ 10^4) and bag/shear breakup (Re ~ 10^5) [16, 25]. They also provide several correlations for breakup length, mean droplet diameters and droplet velocities based on their measurements. A follow-up study by Sallam *et. al* [26] analysed the secondary breakup process and identified ligament tip breakup as the primary source of drop formation in water jet breakup process.

Several researchers have studied the physics of liquid jet breakup and none of the experiments focus on analysing oil jets or water jets at piston cooling operating conditions. Also, though abundant literature on jet impingement and/or spray cooling of flat surfaces are available, there is dearth of data for piston cooling applications.

2.1.2. Quantities of interest

From literature, for steady injection of liquid into a quiescent gas through circular nozzle, the breakup is classified based on Reynolds and Ohnesorge numbers [3, 5]. Reynolds number (Re) represents the relative strength of inertial and viscous forces. Ohnesorge number (Oh) relates viscous and surface tension effects. Ohnesorge number can be represented using Weber and Reynolds numbers, as shown below, where Weber number (We) is the ratio of kinetic energy to surface energy of the liquid.

$$Re = \frac{\rho.u.d}{\mu} \tag{2.1}$$

$$We = \frac{\rho.u^2.d}{\sigma} \tag{2.2}$$

$$Oh = \frac{\mu}{\sqrt{\rho.\sigma.d}} \tag{2.3}$$

$$Oh = \frac{\sqrt{We}}{Re} \tag{2.4}$$

These dimensionless quantities constitute all relevant fluid dynamic properties of the liquid and dictate the type of impact on breakup. However, none of the equations account for aerodynamic interactions and this effect is represented by liquid-to-gas density ratio $\frac{\rho_L}{\rho_g}$ [12].

The entire breakup process can be split into primary and secondary breakup. Primary breakup is the initial detachment of liquid core and secondary breakup is the subsequent disintegration of ligaments and droplets into further smaller structures [13, 14, 24]. For primary breakup, the focus is to identify the point of disintegration which is defined by the breakup length or liquid core length $\left(\frac{L_c}{d}\right)$. This is the length between the nozzle exit and the first point of detachment, that leads to the formation of liquid drop/ligament structures [5, 6]. At this point, disturbances present at the jet exit amplify and reach jet axis, i.e., their amplitude increases to equal jet radius. This enables droplets to pinch-off from the continuous stream of liquid [27]. The nature of the structures formed as a result of this primary breakup, and magnitude of secondary breakup, essentially reflect the dominant factors involved in the disintegration process and classify the type of breakup. Apart from breakup length, another significant parameter is the size (or diameter) of these structures. Both these quantities can be expressed as,

$$\left(\frac{L_c}{d}, \frac{d_{drop}}{d}\right) \sim f\left(Re, We, \frac{\rho_L}{\rho_g}\right) (or) f\left(Oh, \frac{\rho_L}{\rho_g}\right) \tag{2.5}$$

2.1.3. Breakup regimes

Based on Re and Oh, breakup is classified into four different regimes as shown in Fig. 2.1

Rayleigh regime occurs at low jet Re. Axisymmetric oscillations of the jet surface, induced by interaction of inertial and surface tension forces on primary disturbance (Plateau-Rayleigh instability), cause the breakup. Dynamics of this mode are usually uniform and predictable [28]. The jet breaks up in the form of drops [3, 5, 6, 28]. Droplet diameter is usually larger than jet diameter, as shown in Fig. 2.2 and breakup length is found to be inversely proportional to the jet velocity [3, 5, 6].

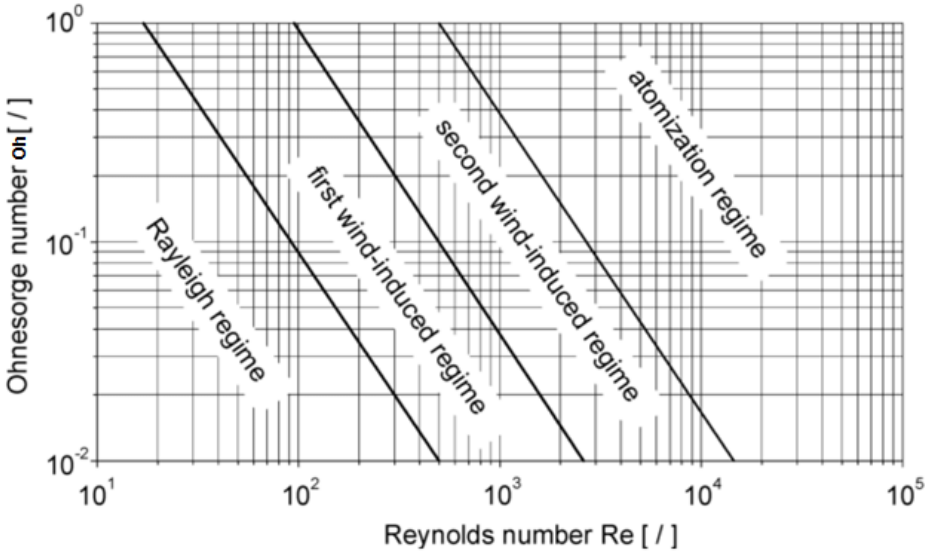

Figure 2.1: Classification of breakup regimes for liquid jets [29].

Increasing the velocity enhances the effects of jet turbulence on disturbances. Surface tension effects are reduced, and the jet enters into the **first wind-induced (FWI)** regime where oscillations with respect to jet axis grow and axisymmetric properties are lost. Unstable surface waves, called sinuous waves, are produced and distort the stream-wise jet in cross-flow direction, resulting in formation of ligament like structures [3, 28]. Beyond this, the aerodynamic drag no longer acts as an instability dampner, and oscillations increase breaking the jet waves and ligaments into droplets. These droplets are of varying sizes, from larger sizes to smaller but within the same order as of jet diameter, as shown in Fig. 2.2 [5, 28].

With further increase in jet velocity, the flow becomes fully turbulent [31] and disruptive forces are predominant. This augments growth of shorter wavelength disturbances along the jet surface, causing the jet to disintegrate [3, 5, 28]. This is the **second wind-induced (SWI) regime**, and the jet breaks very close to nozzle exit, as in Fig. 2.2. Droplet diameters are much smaller and exhibit a wider range than those observed in FWI regime.

Atomization occurs at very high Re where jet disintegrates completely. A conical spray is formed producing unstable ligaments [5] whose lives reduce drastically resulting in formation of much smaller droplets. A particular breakup mechanism for this regime is not identified by previous researchers [3]. A combination of factors like, action of surrounding air, jet turbulence, and/or surface tension effects are found to be responsible. The average droplet sizes are smaller than jet diameter by many orders, as in Fig. 2.2 [28].

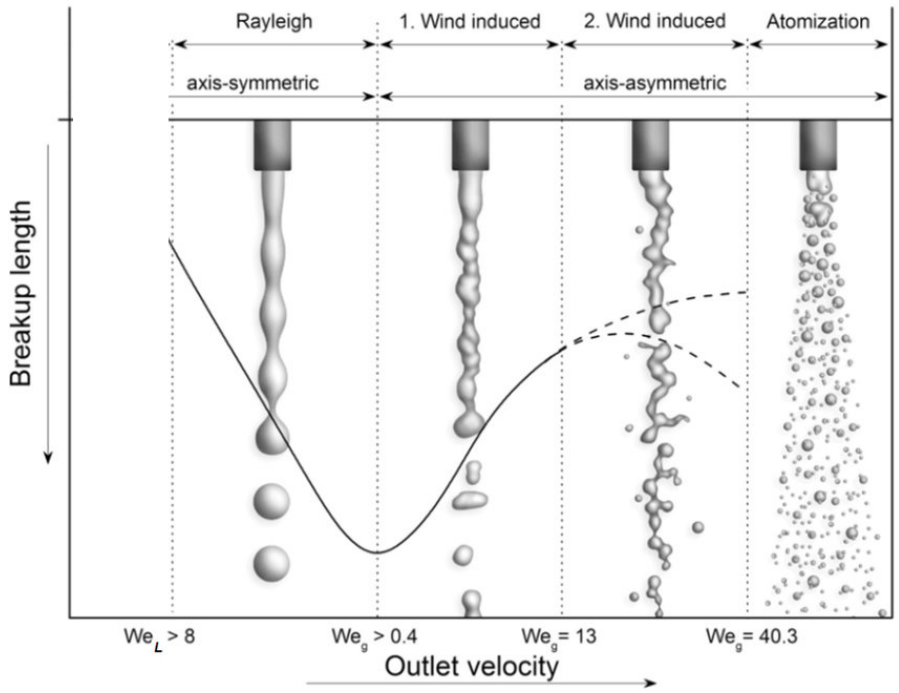

Figure 2.2: Typical characteristics of jets in corresponding regimes [30].

Based on the operating conditions of piston cooling jets given in Table 2.1.3, the jets are found to lie in the second wind-induced regime. They are expected to have shorter wavelength disturbances on the jet surface with primary breakup occurring close to nozzle exit, similar to the example shown in Fig. 2.2. Post detachment, formation of very small ligaments and droplets is anticipated.

Re	3600-4800
We	20000-36000
Oh	0.0395
$\frac{\rho_L}{\rho_g}$	810

Table 2.1: Operating conidtion of DAF's piston cooling jets

2.1.4. Effect of aerodynamics

Primary breakup theories [12, 32] suggest that, in quiescent atmosphere, aerodynamic effects have least influence. Wu *et. al* [13, 14, 24] and Hoyt *et. al* [33] performed experiments to analyze effects of aerodynamics and concluded that, it has little impact when $\frac{\rho_L}{\rho_g} > 500$. Liquid properties at the nozzle exit like boundary layer along the nozzle passage, inherent turbulence of the jet etc., control the breakup mechanism. Far away from the jet exit, primary breakup and aerodynamic induced secondary breakup, where ligaments break due to drag, occur at comparable times and tend to merge resulting in increase of droplet sizes [13, 24]. At these locations, jet does not have sufficient energy to overcome aerodynamic drag.

For the present study, oil jets have liquid-to-gas density ratio around 810, and travel a maximum of 230 mm. At these conditions, preliminary results from the previous study [3] indicate that the jets have sufficient kinetic energy even at maximum distance. Thus, aerodynamics are anticipated to have little influence on jet breakup contrary to the conclusions of by Celik [3].

2.1.5. Importance of Weber Number

For liquid jets at standard conditions, Ohnesorge number is always less than one (Oh < 1), typically Oh ~ $O(10^{-3})$ for water and Oh ~ $O(10^{-2})$ for oil. Hence, it is reasonable to neglect the effect of viscosity which makes surface tension, the major cohesive force. Relative magnitude of surface forces in comparison to the inertial forces control the amplification/dampening of initial disturbances, following Webers theory [12]. Lesser the surface tension, easier the breakup. Thus, neglecting the interactions of jet with surrounding air, Weber number is the governing factor that controls breakup length and droplet diameters for a given liquid.

$$\left(\frac{L_c}{d}, \frac{d_{drop}}{d}\right) \sim f(We) \tag{2.6}$$

At lower We, (i.e., We ~ O(100)), because of increased surface tension the interface roughness is very low [15]. Breakup occurs because of the large-scale turbulent eddies that carry sufficient energy to overcome cohesion, distorting the jet and forming ligaments and droplets [15, 16]. This mechanism is typically found in FWI jets (shown in Fig. 2.2), where bigger ligaments/droplets pinch-off from the liquid core due to large-scale turbulence. Smaller eddies are visible only with increasing We. At this point, ligaments formed are much thinner and droplets are much smaller and the jet breaks very close to the nozzle exit.

2.1.6. Breakup length correlations

Based on approximations explained in the previous section, a simple analysis of Rayleigh breakup results in the following correlation [25],

$$\left(\frac{L_c}{d}\right) = C_r We^{0.5} \tag{2.7}$$

C_r is an empirical parameter which may be affected by turbulence of the jet at nozzle exit, and is of the order of magnitude ~ O(1) [25]. This correlation, developed by Weber (1931), is based on turbulent primary breakup concepts [12]. Grant and Middleman [22] developed a similar correlation based on dimensional analysis with the measurements of their own and those of Chen and Davis for water jets [34]. This is widely used and is given as,

$$\left(\frac{L_c}{d}\right) = 8.51 We^{0.32} \tag{2.8}$$

The primary difference between the two correlations is the power of We, which is a result of measurements that extend over several breakup regimes for the latter whereas Weber's correlation is specifically for turbulent liquid column breakup process. However, based on classifications delineated in section 2.1.3 and from Fig. 2.1 and Fig. 2.2, breakup occurs much closer to nozzle exit (especially for SWI and atomization regimes). Both these correlations have a positive power for We indicating increase in breakup length increase in We. This limits the application of these correlations to jets with properties and conditions similar to Grant and Middleman [22] and Chen and Davis [34].

2.1.7. Droplets and ligaments

Post initial breakup, liquid protrusions form ligaments which then rupture to form droplets [15]. Ligaments and droplets are created by eddies of corresponding size [26]. Size of these structures can be understood by comparing the surface energy required to form a ligament and kinetic energy of the corresponding eddy structure [26, 35]. Subsequent formation of smaller structures from bigger ligaments is a result of Rayleigh breakup of ligaments at its tips and this is found to be the dominant drop forming method [26].

Liquid jets in turbulent regime have a larger turbulence spectrum and thus produce structures of varying sizes. This warrants the need for size distributions. However, owing to the limited understanding of relevant

parameters that affect these structures, and the difficulty in capturing the sizes using experiments, very limited studies attempt to provide distribution data [5]. Photographic techniques performed by liquid jet studies provide only mean or maximum diameter results. Thus, popular way of characterizing typical sizes for a given liquid jet, is by determining mean, minimum and maximum sizes. Generally, mean sizes are represented using Sauter Mean Diameter (SMD). It is defined as the diameter of a sphere that has the same volume to surface area ratio as the particle (or structure) of interest (POI).

$$SMD = d_{32} = \frac{Volume\,of\,POI}{Surface\,Area\,of\,POI} \tag{2.9}$$

This value can be used for comparing different jets. Experiments with photographic analysis use similar assumption to arrive at mean or maximum droplet sizes and provide empirical correlations. Such correlations enable a practical way of linking relevant physics and droplet diameters. For the present study two such correlations are selected based on their ability to capture pertinent parameters involved in breakup. Physical properties of the liquid and operating conditions of the flow are found to have significant influence. Properties of the gas phase have little impact. Also, these correlations are liquid independent as all the liquid properties are represented. Theoretical analysis of Harmon [36] and experimental results of Miesse [37] give the following correlations for liquid jets into still gases, neglecting the effects of aerodynamics.

$$Mean\,(Harmon) = d_{drop} = 1.63d(1+3Oh)^{\frac{1}{6}} \tag{2.10}$$

$$Max\,(Miesse) = d_{0.99} = d\,We_L^{-0.33}(23.5+0.000395Re_L) \tag{2.11}$$

However, there exists a conflict among these correlations. Harmon's correlation provides a direct proportionality of droplet size to Weber Number (We), whereas Miesse's correlation suggests an inverse proportionality. Fig. 2.2 indicates that, higher the We smaller the droplets, which warrants Miesse's correlation and questions the application of Harmon's expression to different conditions.

2.1.8. Computational modeling of liquid jet breakup

Following sections delineate the basics behind modelling and simulation of liquid jet breakup. First, basic conservation equations are presented, followed by discussion of multi-phase models and turbulence modelling.

Basic equations of motion

Basic conservation equations are of the form,

$$\frac{\partial \rho}{\partial t} + \frac{\partial(\rho q_i)}{\partial x_i} = 0 \tag{2.12}$$

where ρ is the density and q is any conserved quantity. With equation 2.12, individual conservation equations can be written as shown below.

Conservation of Mass

Conservation of mass or continuity equation states that the rate of change of mass within a fluid element is equal to the sum of mass flow across the inlet and outlet boundaries of the element [38, 39]. This is expressed as,

$$\frac{\partial \rho}{\partial t} + \frac{\partial(\rho u_i)}{\partial x_i} = 0 \tag{2.13}$$

Conservation of Momentum

This is based on Newton's second law of motion according to which, the rate of change of momentum of a fluid particle equals the sum of forces on that particle [38, 39]. The equation is given as,

$$\frac{\partial(\rho u_i)}{\partial t} + \frac{\partial[\rho u_i u_j]}{\partial x_j} = -\frac{\partial p}{\partial x_i} + \frac{\partial \tau_{ij}}{\partial x_j} + \rho f_i \tag{2.14}$$

Here p correspond to pressure and τ_{ij} corresponds to viscous force. f_i represents body forces.

Conservation of Energy

Energy conservation is based on the first law of thermodynamics which states that energy can neither be created nor be destroyed. It can only change from one form to another [38, 39]. This is represented by,

$$\frac{\partial(\rho E)}{\partial t} + \frac{\partial[\rho u_i E]}{\partial x_i} = -\frac{\partial[p u_i]}{\partial x_i} + \frac{\partial[u_i \tau_{ij}]}{\partial x_i} + \rho f_i u_i - \frac{\partial K_i}{\partial x_i} \tag{2.15}$$

Here E is the total energy and K_i denotes heat conduction.

Incompressible Navier-Stokes equations

Incompressiblity assumption is applicable when the flow Mach number is less than 0.3 and the density variations are small enough to be neglected. In the present study, this assumption is valid for liquid flows, as their Mach numbers are always low. Also, gravity is found to have least effect on liquid jets [3] and hence, influence of body forces can also be neglected. Equations 2.13 and 2.14 can be modified to account for these assumptions and together they constitute the incompressible Navier-Stokes equations given by,

$$\frac{\partial u_i}{\partial x_i} = 0 \tag{2.16}$$

$$\frac{\partial u_i}{\partial t} + \frac{\partial[u_i u_j]}{\partial x_j} = -\frac{1}{\rho}\frac{\partial p}{\partial x_i} + \frac{\partial}{\partial x_i}\left(\nu \frac{\partial u_i}{\partial x_i}\right) \tag{2.17}$$

where ν is the kinematic viscosity

Multi-phase modeling

For free-surface liquid jet simulations, it is important to accurately capture the interface between oil jet and surrounding air. The model should estimate the complicated evolution of jet in space and time, capturing jet spreading and disintegration. In this thesis, Volume of Fluid (VOF) model is used and hence, is described below in brief.

VOF is a simple, but powerful method for obtaining complicated free-surface boundaries between phases [40]. It is an interface capturing method and is based on volume fraction. In this method, a function F is defined representing volume fraction. F goes to 1 at points which are occupied by the phase of interest (liquid) and 0 otherwise. By this way, the average value of F in a cell, would represent the volume fraction of the phase in that cell. With this function, entire liquid jet can be reconstructed. The location of the liquid interface within a cell can be computed using normal vector to the boundary which lies along the direction with rapid change in F [40]. To determine this boundary normal, it is important to calculate derivatives of F. This is computed by the following equation, that governs the evolution of volume fraction across the flow field,

$$\frac{\partial F}{\partial t} + u_i \frac{\partial F}{\partial x_i} = 0 \tag{2.18}$$

VOF model assumes that all phases share pressure, temperature and velocity fields [41]. Advantages of VOF is the minimum storage requirements which is beneficial for 3D computations. Also, because the model follows regions rather than tracking surfaces, issues associated with surface intersection are avoided [40].

Limitation associated with this model is the requirement of very fine mesh in the region of interest. This results in increased computational effort. Generally, with VOF, free-surface is not captured sharply and is distributed over the cell and without proper mesh, it might get smeared. Also, the type of convection scheme can impact the solution produced. Typically, VOF with lower order scheme produces similar smearing and inaccurate results [42]. Even with higher order schemes oscillations may be induced into the solution. These difficulties can be overcome with the usage of methods which keep the free-surface sharp and also produce monotonic profiles for F [42]. Thus, in the present study VOF model is used with High Resolution Interface Capturing (HRIC) scheme [41, 43]. With this approach, sharp interfaces can be captured by proper estimation of spatial variation in liquid volume fraction. More about this scheme can be found in StarCCM+ user guide [43].

Turbulence modeling

Proper modelling of flow field turbulence is necessary to accurately capture the breakup process, as turbulence at jet exit is the dominant factor for breakup [17, 22, 24, 25]. Generally, in any turbulent flow, there exists rotational structures or eddies with a wide range of length and time scales [44, 45]. These eddies can be solved for or modelled, using suitable strategies already available. Based on this choice, there exists different techniques for turbulence modelling in CFD. Direct Numerical simulation (DNS) is the method where all scales are solved for, in an exact manner. However, this method requires a very fine mesh and huge computational resources.

In Reynolds Averaged Navier Stokes (RANS) approach, all scales are modelled. This method is computationally inexpensive and is widely used for industrial simulations [3]. However, only mean results can be obtained. Reflection of large scale turbulence on the flow field is predicted only as mean value by these models. Small scale eddies, relevant for ligament and droplet formation in liquid jets, cannot be estimated using RANS. Fig. 2.2.5 shows an example of a single phase (air-in-air) jet, and the amount of information lost using RANS when compared to the actual jet (DNS) is visible. The chaotic nature of the jet boundary, its disintegration into smaller turbulent vortices away from the jet axis, and the actual jet spreading, are absent in RANS' solution. Also, development of surface instabilities cannot be captured which will result in an unbroken jet, as obtained during the analysis of Celik [3]. Thus, for estimating the behaviour of liquid jet interface accurately, RANS is insufficient.

Intermediate to these two approaches lies the Large Eddy Simulation (LES) technique. Here, the large scale eddies are solved (resolved scales) and the small ones are modelled (unresolved scales or sub-grid scales). Fig. 2.4 shows a schematic of resolved and unresolved scales. The idea behind this method is that, major part of the flow energy is contained in large eddies. These structures are subjective to the problem of concern as they are dependent on properties of the nozzle (like length, shape, roughness), boundary conditions, liquid type, and have to be solved for different cases/conditions. The smaller structures are more or less universal to all turbulent flows and can be assumed isotropic, enabling their representation with models [48]. Thus, with feasible computational cost, LES encapsulates majority of the physics involved. The parameter that separates resolved and unresolved scales, in LES, is the grid resolution (cut-off scale) whose impact will be addressed in detail in section 2.1.8. This scale separation process is called low-pass filtering. Here, any field variable(ϕ) can be split into filtered (or resolved scales, $\overline{\phi}$) and sub-filtered (or unresolved scales, ϕ') quantities using a filter kernel [45, 47, 49].

$$\phi = \overline{\phi} + \phi' \tag{2.19}$$

Equation 2.19 substituted into the Navier-Stokes equations 2.16 and 2.17 to obtain LES filtered, governing equations of motion as shown below,

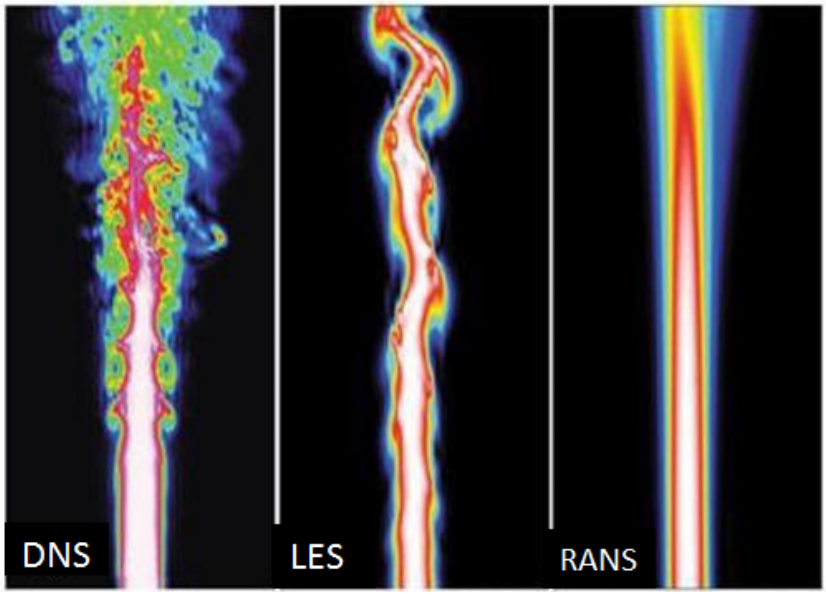

Figure 2.3: CFD of single-phase jet using different turbulence modelling approaches [46].

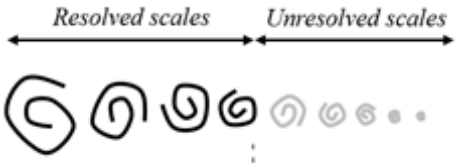

Figure 2.4: Typical LES approach of scale separation [47]

$$\frac{\partial \overline{u_i}}{\partial x_i} = 0 \tag{2.20}$$

$$\frac{\partial \overline{u_i}}{\partial t} + \frac{\partial \overline{u_i u_j}}{\partial x_j} = -\frac{1}{\rho}\frac{\partial \overline{p}}{\partial x_i} + \nu \frac{\partial}{\partial x_j}\left(\frac{\partial \overline{u_i}}{\partial x_j} + \frac{\partial \overline{u_j}}{\partial x_i}\right) \tag{2.21}$$

The non-linear term $\overline{u_i u_j}$ is the main difficulty in LES. It is called the filtered advection term and it requires knowledge of the unfiltered velocity, which is unknown and so it must be modeled. This term can further be split, following Leonard [50], as

$$\overline{u_i u_j} = \tau^r_{ij} + \overline{u_i u_j} \tag{2.22}$$

Substituting this into 2.21,

$$\frac{\partial \overline{u_i}}{\partial t} + \frac{\partial [\overline{u_i u_j}}{\partial x_j} = -\frac{1}{\rho}\frac{\partial \overline{p}}{\partial x_i} + 2\nu \frac{\partial}{\partial x_j}\overline{S_{ij}} - \frac{\partial \tau^r_{ij}}{\partial x_j} \tag{2.23}$$

Here, S_{ij} is the rate of strain tensor and τ^r_{ij} is the residual stress tensor (or SGS stress tensor) that groups all unclosed terms [47, 48]. This term is represented as,

$$\tau^r_{ij} = \frac{1}{3}\tau_{kk}\delta_{ij} - 2\nu_{SGS}\overline{S_{ij}} \tag{2.24}$$

where δ_{ij} is kronecker delta. ν_{SGS} is the sub-grid scale viscosity that has to be modelled using various methods, few of which are described in the following section. Although, several models are present in literature, only those available in StarCCM+ are described below,

SGS models

For modelling unresolved scales, three options are available in StarCCM+.

- Smagorinsky SGS model,
- Dynamic Smagorinsky SGS model, and
- WALE SGS model.

SGS viscosity is represented by Smagorinsky models similar to Prandtl's mixing length hypothesis as,

$$\nu_{SGS} \sim \Delta^2 \mid S \mid \tag{2.25}$$

The proportionality constant or the Smagorinsky coefficient that brings equality to the above relation is case dependent [47]. This is resolved using Dynamic Smagorinsky, where the coefficient is calculated during the simulation and adjusted. Both models assume that production equals dissipation and this assumption leads to non-zero ν_{SGS} at the wall [51]. To solve this, correction functions, such as Van-driest damping are necessary, which are also not universal. Further, ν_{SGS} is represented only by strain rate, $\mid S \mid$, and energy contained around the sources of vortices are neglected. This yields Smagorinsky models inadequate. Wall Adapting Local Eddy viscosity (WALE) model is a modern sub-grid scale model [51, 52] which represents eddy viscosity using an operator function,

$$\nu_{SGS} = C_m \Delta^2 OP(x,t) \tag{2.26}$$

This operator is invariant to coordinate transformation and is a function of both strain and rotation rate. It is easily assessed on a computational grid and goes to zero at the wall without the need for any additional damping functions. However, similar to Smagorinsky, the model constant is not universal. But, validations with StarCCM+ have shown less sensitivity to model constant variation for the WALE model, than Smagorinsky model. Therefore, this is recommended by StarCCM+ and is used in the present study [53].

Effect of grid resolution and LES quality

Selection of grid size is a challenging task even for single phase LES. This parameter affects the quality of results. There are no universal criteria used for selecting appropriate grid size. Popular ones, useful for present analyses are mentioned below.

Criteria - 1: Kolmogorov's length scale (η) < cell size in region of interest (h) < Taylor Micro scale (λ). This criteria is recommended by StarCCM+ [48]. Komogorov and Taylor scales can be estimated with analytical expressions available in any turbulent flows book [45] or with preliminary RANS analysis. For canonical flows, several experiments and simulations have been performed and these values can be obtained from such investigations as well. For scale resolving simulations, this criterion is found to produce good results[48].

Criteria - 2: If the number of points used to resolve the integral length scale of turbulence is between 12 and 20, then the grid resolution is found to be sufficient [54–56]. For free turbulent jet, the integral length scale is of the order of nozzle diameter (d). Thus, grid size should be between $\frac{d}{12}$ and $\frac{d}{20}$.

These criteria are for single phase LES. For multi-phase, involving droplets, no such recommended criterion exists. Typically, for liquid jets in SWI and atomization regime, droplet sizes can go to the order of micrometers [13–15, 24]. Added complexity with VOF model is that, the technique requires a fine mesh in

the region where interaction is expected to occur [41]. Usually two or three cells are required to capture the periphery of the droplet as shown in figure Fig. 2.5.

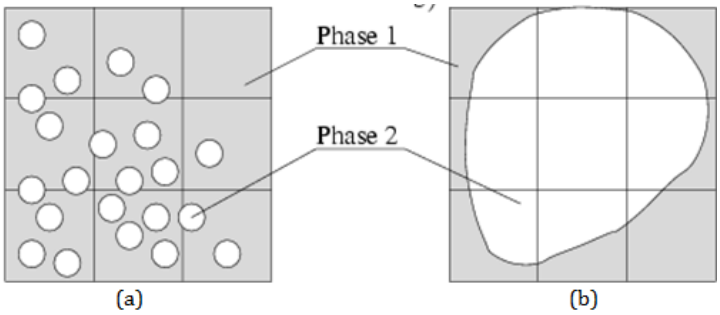

Figure 2.5: Illustration of (a) unsuitable grid and (b) suitable grid for two-phase VOF [41]

Thus, in order to capture all droplets, a very fine mesh should be constructed which will result in a computationally expensive simulation. This is not practical with the time period available for the present work. Hence, another criteria,

Criteria - 3: Total computational time < 48 hours

is considered to construct and perform several simulations and produce sufficient results. Some sacrifice is made and a coarser grid size, that satisfies single-phase LES criteria, may have to be selected. The smallest droplet that can be captured will be bigger than the cell size in the region of interest. This is acceptable because the overall breakup mechanism is expected be unaffected as the flow energy relevant for piston cooling is contained mostly in the larger structures. Nevertheless, the need for grid refinement is assessed based on the results obtained and the qualitative/quantitative (in)consistencies with typical physics from literature.

The impact of selected grid size on LES results can be verified by checking the quality of the simulation. In a proper simulation, cut-off scale should be small enough. Otherwise, the isotropic assumption for small scales will be invalid and some large scale eddies will also get modelled [43]. This can be verified with the LES quality metric (γ) given (2.27). The ratio indicates turbulent kinetic energy (TKE) of resolved scales relative to the overall TKE.

$$\gamma = \frac{TKE_{resolved\ scales}}{TKE_{resolved\ scales} + K_{SGS}} \tag{2.27}$$

where K_{SGS} is the unresolved scales TKE or sub-grid scale TKE. When this ratio is > 0.8, more than 80% of large scale TKE is solved during the simulation and the LES analysis is deemed to produce reliable results [45, 55, 56]. However, this is difficult to achieve in industrial simulations and requires extremely fine mesh and larger computational resources. Hence, this is taken as a sufficient condition in the present work.

There is another simple parameter which is the turbulent viscosity ratio (TVR). This criteria is recommended by StarCCM+ support based on their experience and is found to be achieved easily for industrial LES. Turbulent viscosity is proportional to the cut-off scale. This means that higher the turbulent viscosity, bigger the cut-off scale and hence a large range of length scales remain unresolved and get represented by SGS models. This results in modelling of some large scale eddies that are not isotropic. To avoid this, the criterion serves as an indicator and hence is taken as a necessary condition in the present analysis. According to this condition,

$$TVR, \frac{\nu_T}{\nu} < 100 \tag{2.28}$$

where ν_T is the turbulent viscosity and ν is kinematic viscosity (property of the fluid).

LES inflow generation

Accuracy of numerical simulations is strongly affected by the inlet boundary condition specified [57]. For LES and DNS applications, generation of inflow data is a complicated issue. The best method is to use precursor simulations where data of large-scale turbulence at the inlet can be obtained. However, this method is restricted to flows where inflow corresponds to fully developed turbulent boundary conditions. Also, the computational load for such simulations are very heavy [57, 58].

Other ways of generating inflow conditions are,

- **Synthetic Eddy Method (SEM):** involves superposition of unsteady fluctuations, generated by various ways, over the inlet mean velocity field, and
- **Recycling and Re-scaling method:** involves construction of an auxiliary LES simulation with periodic boundaries from which the unsteady flow field is extracted at a particular plane and is used for spatial evolution analysis of the actual problem.

In this study, Synthetic Eddy Method (SEM) available in StarCCM+ is used for generating turbulence at the inlet and is described as follows. As mentioned before, fluctuations are superimposed on the mean field. These fluctuations can be random, without any spatial or temporal correlations. In that case, the energy generated is uniformly spread and large-scale turbulent structures are absent. This leads to fast dissipation of this pseudo turbulence with spatial evolution [58]. With proper correlations, the method produces fully developed turbulence and has been validated for isotropic turbulence and spatial development in channel flows [57]. Each eddy is represented by a specific shape function that describes its spatial and temporal behaviour. In StarCCM+, eddies are specified with the help of turbulent intensity and length scale or, Reynolds stresses and length scale [59], obtained from RANS simulations or experiments. The size of the eddies is the characteristic scale of turbulence and is the most important parameter to be specified as it generates turbulent inflow structures with proper discretization on the inlet mesh. More details about this method can be found in [3, 59].

Advantages of this method are the reduced set of statistics required as preliminary conditions for creating synthetic turbulence [57]. The computational load is also minimal which is based on the quality of input conditions specified from RANS or other sources. Limitations of this method are that, it produces only an approximation of real turbulence, and must be allowed to evolve with proper correlations that develop naturally as eddies are convected downstream. But for this to occur, it is important to leave enough distance between the inlet and the region of interest [58] which is not a universal value. Also, length scale and other turbulent variables required as input for this method are not always available and are very subjective [58].

Blob Detection Model

To analyse ligament/droplet structures in two-phase flow and to quantify droplet sizes, it is imperative to detect these grid-resolved structures within the VOF field. This can be done using the blob detection model available in StarCCM+. This model identifies droplets or "blobs" by selecting the cells in which, the volume fraction of the required phase is equal to or greater than a specified threshold value [41]. Each blob is made of numerous cells and upon detection, a blob is treated as a sphere. This is similar to the assumption involved in determination of SMD. Diameter of these blobs are computed by considering the detected ligament/droplet volume as a sphere [41].

Past computational studies

Numerical efforts on liquid jet breakup cover basic laminar breakup or focus on liquid atomization. Several DNS and quasi-DNS studies exist for high Re applications where water sprays or diesel sprays are simulated for combustion. No literature is available for liquid jets at the operating conditions given in Table.2.1.3.

Very few studies are present for piston cooling applications, but they do not have sufficient information regarding oil jet breakup and corresponding droplet sizes.

Moghe et. al [56] performed LES analysis of oil jets and quantified turbulent kinetic energy using spectral analysis. However, they lacked quality validation data, as they compared instantaneous spreading results to the corresponding experimental values. Wendling et. al [60] studied oil jet breakup using level set method and volume of fluid (VOF) approach. They used space time finite element method with level set and analysed jet breakup at higher flow rates leading to primary atomization. Their results show increased disintegration with increase in inlet flow rate. Spreading behaviour also increases. They also incorporated moving piston and determined oil-filling ratio (amount of oil entering the cooling gallery with respect to the amount of oil exiting the nozzle) for laminar and turbulent oil jets. Their results showed that both VOF and level set models provide similar results for laminar jets [60]. Results for turbulent jets are not presented properly to validate their statement of superiority of level set method over VOF. Also, the level set method was found to lack mass conservation, which is possible to achieve using VOF.

2.2. Crankcase Turbulence

In previous sections, liquid jet breakup process in quiescent atmosphere was discussed. In actual piston cooling process, oil is injected into a turbulent atmosphere in the crankcase where flow is in constant motion due to several moving parts. Liquid jets in such an environment may behave differently due to the significant enhancement in aerodynamic forces. Interaction between the two phases will increase leading to disintegration different from breakup in a quiescent atmosphere. Thus, it is important to estimate relevant flow properties by investigating flow within the crankcase based on which effect of surrounding flow on oil jet can be investigated.

In this section literature review on crankcase flow and pressure fluctuations is presented. Source of crankcase flow is discussed in section 2.2.1 followed by a short description of ventilation in 2.2.2. Various dynamics present within the crankcase are mentioned in section 2.2.3. Based on their relative magnitude of impact on crankcase flow, significant contributors are identified to facilitate the simplification process during the analysis. Breathing effect is outlined in section 2.2.4 followed by relevant computational models in section 2.2.5.

2.2.1. Source and nature of crankcase flow

Primary source for the crankcase flow is the leakage of 'blow-by' gases from several regions [60]. The most significant contributor is the combustion chamber, giving ~ 60 % [60, 61]. Typical schematic of the same is shown in Fig. 2.6. Other sources are turbocharger shaft, air compressors and valve stems [60]. Apart from these gases, mist of engine oil, used for cooling and lubrication, is also present resulting in a multi-phase flow domain. This is further affected by bay-to-bay breathing in the crankcase. A bay is part of the crankcase volume below the cylinder block, as shown in Fig. 2.6. This is explained in detail, in section 2.2.4

2.2.2. Crankcase ventilation

To prevent the closed crankcase volume from getting pressurized due to continuous blow-by, a ventilation system is necessary. Typical engines contain small holes drilled on the walls, leading the gases to flow into the environment after treatment (Open crankcase ventilation, OCV, like in PACCAR engines) or back to the intake manifolds for reuse (Closed crankcase ventilation, CCV) [60, 62]. Apart from pressurizing, other consequences of improper (or lack of) ventilation include increased emissions, engine surface damage, increased engine oil consumption etc [60, 62].

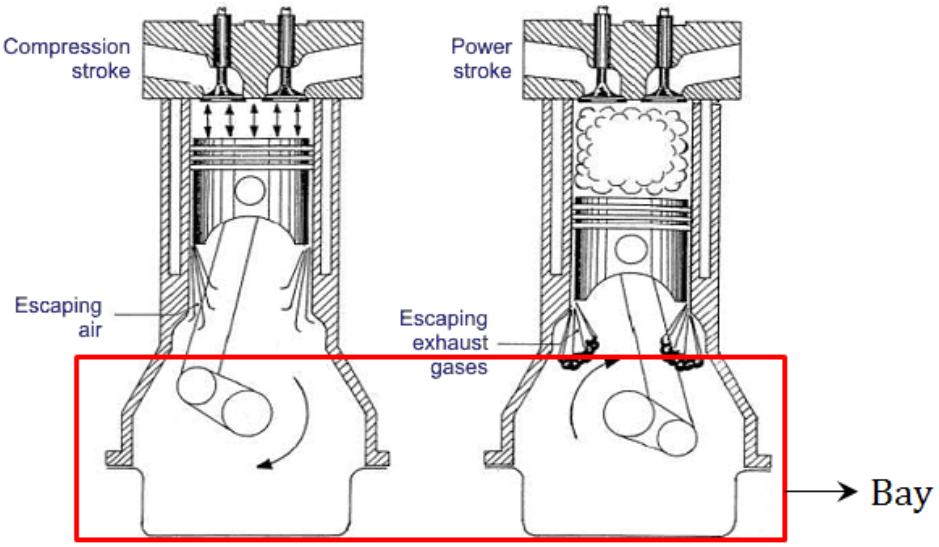

Figure 2.6: Typical blow-by from combustion chamber [60]

2.2.3. Other Dynamics within the crankcase

Apart from blow-by and ventilation, crankcase flow is further complicated by the presence of other dynamics that are listed below. In this section, these are discussed and the most significant contributor(s) to crankcase flow physics is(are) identified. This is done using review of relevant literature and, aids in constructing a simplified, in-expensive model during the analysis.

- Reciprocating piston motion,
- Crankshaft rotation,
- Movement of connecting rod,
- Engine vibrations, and
- Oil free-surface motion.

These dynamics lead to a three dimensional, multi-phase and unsteady system which is cumbersome to simulate. Hence, it is important to make several approximations based on their physical significance on piston cooling jets' evolution process. For example, engine vibrations and oil free-surface movement are very small when compared to the rest of rigid body motions, and can be neglected. Flow can be assumed to be single phase, purely gaseous, in order to predict pressure/velocity fluctuations in the bulk flow. Amongst the remaining dynamics, dominant mechanisms can be identified through detailed review of literature, which is summarized as follows.

Reciprocating motion of pistons and crankshaft rotation are the two dominant dynamics in the crankcase [58, 60]. Crankshaft rotation is responsible for creating vortices around its surface. However, this is found to mainly affect the lubrication process and has lesser impact on pressure variation in the bulk flow when compared with piston motion [61, 62]. Piston motion is the highest contributor for turbulence within the crankcase, as flow displaced by the piston is greater than that displaced by crankshaft and/or any typical blow-by [61, 63, 65].

2.2.4. Bay-to-bay breathing effect on pressure variation

Consider an ideal configuration of closed single cylinder engine. Pressure variation in the crankcase is dictated by the polytropic expression shown below,

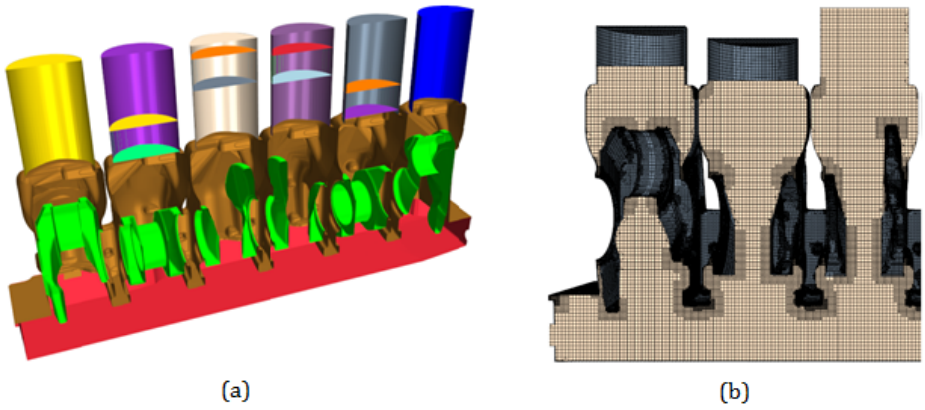

Figure 2.7: (a) Isometric view and (b) Cross-sectional view of PACCAR's MX-11 engine. Figures showing the geometric variations within and in-between the cylinders

$$p_{crankcase}.V^{\gamma}_{cranckase} = cosntant \tag{2.29}$$

Periodic piston motion means periodic change in volume and pressure increases with decrease in volume (piston moving down) and vice versa [61–64], making the work per engine cycle zero.

In real engines, pressure under one cylinder is affected by its location within the engine and relative motion of other pistons. For example, in a four-cylinder engine, cylinders 2 and 3 (middle) have two-way communications whereas, cylinders 1 and 4 (ends) are hindered on one side by the presence of walls. Hence, pressure fluctuation due to reciprocating motion of pistons is different for those bays and finite losses occur.

Fogliarino performed 1D simulations of crankcase flow and observed periodic variation of pressure but different from ideal sinusoids, as shown in Fig. 2.8. This deviation was due to bay-to-bay breathing. Cylinders with least breathing area were found to have greatest amplitude variation [63].

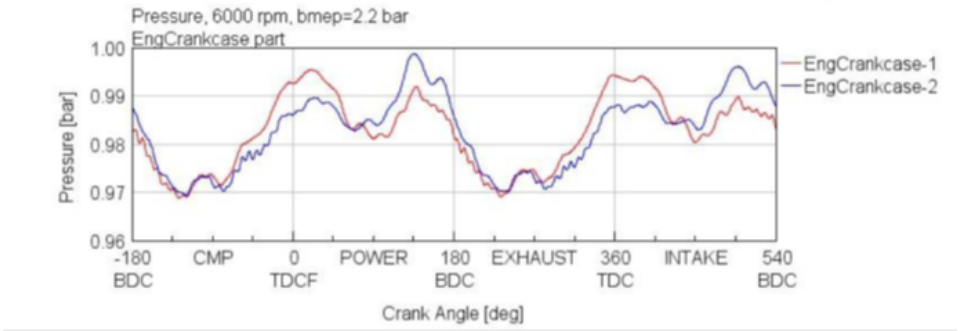

Figure 2.8: Typical pressure variation in a cycle by Fogliarino [63]

2.2.5. Computational models

In this section, brief descriptions of numerical models relevant for crankcase flow simulation are presented. Turbulence is modelled with RANS technique which is discussed shortly followed by various wall models available in StarCCM+. Fianlly, piston motion is modelled by overset meshing method and this is outlined with its theory, advantages and limitations.

RANS Turbulence modeling

As mentioned in section 2.1.8, RANS turbulence is based on modelling all turbulent length scales present in the flow field. Equations for RANS modelling are obtained by using the averaging operator ($\langle . \rangle$) on basic Navier-Stokes equation given by (2.16) and (2.17). First task is to perform Reynolds decomposition where the flow field variables are divided into mean ($\underline{.}$) and fluctuating parts.$\underline{'}$ as shown in equations 2.30 and 2.31.

$$Velocity, u = \underline{u} + \underline{u'} \tag{2.30}$$

$$Pressure, p = \underline{p} + \underline{p'} \tag{2.31}$$

These are then substituted into equations 2.16 and 2.17 to obtain Reynolds Averaged Navier Stokes equation [44, 45, 66],

$$\frac{\partial \langle \underline{u_i} \rangle}{\partial x_i} = 0 \tag{2.32}$$

$$\frac{\partial \langle \underline{u_i} \rangle}{\partial t} + \frac{\partial [\langle \underline{u_i} \rangle . \langle \underline{u_j} \rangle]}{\partial x_j} = -\frac{1}{\rho} \frac{\partial \langle \underline{p} \rangle}{\partial x_i} + \frac{1}{Re} \frac{\partial}{\partial x_i} . \left(\frac{\partial \langle \underline{u_i} \rangle}{\partial x_i} \right) - \frac{\partial \langle \underline{u_i' u_i'} \rangle}{\partial x_i} \tag{2.33}$$

Here the non-linear term $-\langle \underline{u_i'} \underline{u_j'} \rangle$ is the Reynolds stress tensor (RST) which is represented by various turbulence models, few of which are discribed below.

Amongst the various RANS models available in StarCCM+, realizable $k-\epsilon$ is a popular model for industrial simulations because of its simplicity and inexpensive computational requirements. In general, $k-\epsilon$ models work well in estimating turbulence in the free-stream or the bulk flow in the domain [67]. Their performance is relatively poor in the near-wall region and also for unconfined flows [3]. Standard $k-\omega$ by Wilcox [68] works well near-wall and is ineffective in the bulk flow. It is also very sensitive to free-stream or inlet conditions. The shear stress transport $k-\omega$ (SST $k-\omega$) model by Menter [69] provides a blending of standard $k-\omega$ and standard $k-\epsilon$ model and can be applied to flow fields which have significant contributions from both near-wall and bulk flows. Assumptions involved with RANS leading to its inability in predicting the entire Reynolds stress tensor limits application of these models to highly anisotropic turbulent flows.

Wall modelling

An important parameter used in near-wall modelling is the dimensionless wall distance (y^+) given by,

$$y^+ = \frac{u^* d_w}{\nu} \tag{2.34}$$

Based on this y^+ , three different approaches are available in StarCCM+ [70]. Description of these approaches are summarized from StarCCM+ user guide [70] and are presented below.

Low y^+ wall treatment

This approach is based on resolving viscous sub-layer and the transport equations are solved in the cells present within this layer. With this method, the condition of $y^+ \leq 1$ should be met and this requires fine mesh in the near-wall region, resulting in increased computational effort [3, 70].

High y^+ wall treatment

In this approach, wall functions are used to model the near-wall flow. This reduces the computational cost, as coarser mesh can be used, but the accuracy of results are affected. With this method, the condition: y^+>30 must be met [70].

All y^+ wall treatment

This is a combination of the above two methods where y^+ can be varied and the approach automatically selects the appropriate treatment within the domain. However, this blending model is found to have least accuracy out of all three wall treatment approaches [70].

Overset meshing method

Overset meshing is a technique used to discretize the computational domain with overlapping meshes when moving bodies are involved in the problem [71]. In this method, there is a stationary background mesh overlapping which the moving region's mesh is generated. An interface is created over or around the moving surface through which the two meshes communicate. Fig. 2.9 shows an example of overset mesh schematic. The highlighted cell with center C is the active cell and can be part of the background region or moving/overset region. The cell adjacent to this is called the acceptor or ghost cell, shown by dashed lines in the figure, whose cell center is 'o'. For each acceptor cell in one mesh, there are a number of neighboring donor cells in the other mesh (whose cell centers are denoted by N_i) [71]. The relationship between donor and acceptor cells depends on the interpolation scheme used at the interface between two regions [71].

In StarCCM+, background and overset regions are coupled via the hole cutting process. This is done by cutting a hole in the background mesh according to the position of the moving region. When small gaps are encountered like in the near wall region, an acceptor may fall outside the background mesh. Such cells with vertices outside background mesh get deactivated by default. This results in very few number of cells available and causes a communication error between the two meshes. This can be rectified by using 'close proximity' option. With this, the hole cutting process judges whether a cell is outside or not, based on its centroid, allowing for increased number of cells at smaller gaps. It is also possible to model zero-gap which is encountered when the two regions come in contact with each other. This can be done by using separate zero-gap algorithms [71]. These are the primary advantages of using overset method.

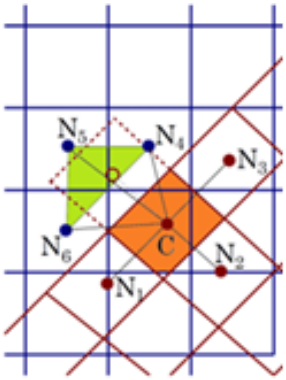

Figure 2.9: Overset mesh schematic [71]

Compared to re-meshing technique, overset method models the physics of rigid body motion accurately. It allows greater control of local grid and is flexible [72]. Another advantage of overset meshing is that, it can be applied to structured, unstructured grids or a combination of both [73]. For piston motion modelling, cells below or above the piston that do not contribute to the flow field, can be deactivated. This results in reduction of total cell count at certain instances based on local piston position. For crankcase flow, the region of interest is below the piston and cells above can be removed. Major drawback of this method is the increased computational costs due to interpolation between the two meshes. Also, this method introduces mass conservation errors, especially for closed domain simulations [74]. However, investigations on internal combustion engines with StarCCM+ show that the latter can be reduced to negligible values by optimizing the settings suitable to the relevant model [74].

2.3. Liquid jet in turbulent atmosphere

Pressure/velocity fluctuations in the crankcase may affect jet structure based on amplitude of wavering. Thus, it is important to investigate the characteristics of liquid jets in turbulent atmosphere. Within the crankcase, part of the flow is along reciprocating piston axis (co-axial/counter-axial flow) which is parallel to the axis of oil jets. During upward motion of pistons, decrease in pressure draws air into the crankcase, creating radial flow (cross-flow)[75]. These components are augmented by rotating crankshaft and movement of connecting rods. Also, at the point of change in direction of piston motion, flow deflection increases these radial elements.

No investigations are available in literature that study liquid jet breakup in turbulent atmosphere with both co-axial and cross flows. By identifying the relative magnitude of these flows through a separate CFD model for crankcase turbulence, whose literature was discussed in section 2.2, the process can be isolated to study their respective impacts on oil jets. In this section, liquid jets with co-axial flow are discussed briefly in section 2.3.1. This is followed by jets in cross flow in section 2.3.2. Using these descriptions, effect of co-axial and cross flows on oil jets are estimated in section 2.3.3, with the help of preliminary results from the study of Celik [3].

2.3.1. Effect of co-axial flow on liquid jets

With co-axial gas streams, liquid jet breakup can be divided into two stages: primary breakup due to disturbance near the nozzle exit and secondary breakup due to aerodynamics. Primary breakup of turbulent jets with co-axial flow is due to the eddies present in liquid jet [76]. This is because liquid phase has more inertia than gas [14, 77]. For laminar jets, Kelvin-Helmholtz's instability is found to cause the initial destabilization [77, 78]. Due to shear between the two streams, axisymmetric modulations are triggered on the interface, causing initial breakup (Fig. 2.10).

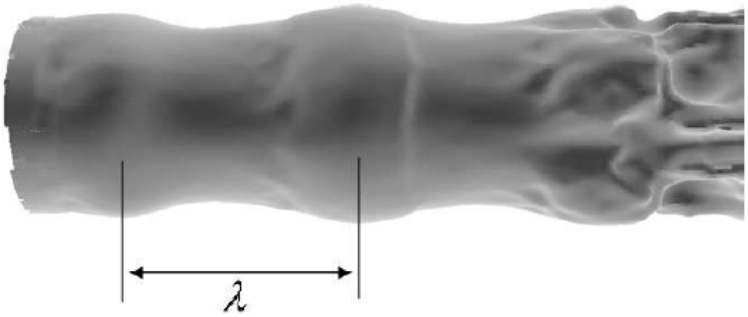

Figure 2.10: Axisymmetry modulations due to KH instability where λ is the wavelength of disturbance[78]

These waves then undergo Rayleigh-Taylor instability leading to development of elongated ligaments and finally suffer secondary breakup to form droplets [78], as shown in Fig 2.11. Post breakup, aerodynamic interactions can affect the evolution of ligaments/droplets and can induce secondary breakup. However, this aspect is not investigated thoroughly in literature. Droplet count and sizes post secondary breakup, and deviation of results from quiescent atmosphere remain unclear.

Typically liquid-to-gas momentum ratio (or the dynamic pressure) is used for estimating the degree of influence of co-axial flows on the jet breakup process [79]. This is given as,

$$M = \left(\frac{\rho_L}{\rho_g}\right)\left(\frac{v_L^2}{v_g^2}\right) \tag{2.35}$$

where, $\frac{\rho_L}{\rho_g} = 810$ for oil, v_L is the liquid velocity and v_g is the gas velocity. For liquid jets in low-speed

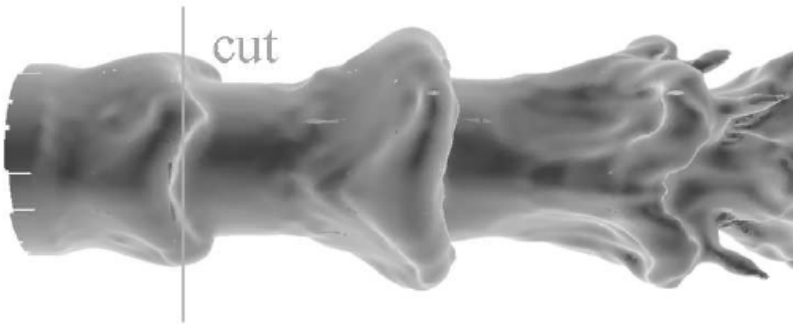

Figure 2.11: Rayleigh-Taylor instability on jet surface [78]

co-axial flows (M>>1), bag-like and rim-like structures are introduced on the jet surface without much effect on reminder of the jet. Inertia of the jet dominates aerodynamic interaction on initial breakup. When M = 1, high amplitude disturbances due to the gas flow are visible on the surface without any disintegration [79]. Only when M < 1, disintegration happens. Initially, pinch-off or surface breakup occurs where ligaments and droplets are stripped off from the jet surface. When gas inertia is significantly higher (M<<1), aerodynamic effects dominate the jet evolution process [79]. For jets with counter-axial air stream, no specific conditions exist in literature. However, similar conclusions can be drawn. Based on Kelvin-Helmholtz instability theory, since the heavier fluid (liquid) is always beneath the lighter fluid (gas), the former will encounter negligible changes in its characteristics [44] if the relative velocity at the interface is small, and vice versa.

2.3.2. Effect of cross-flow on liquid jets

With cross-flows, liquid jet disintegration is caused by waves on the surface due to aerodynamic drag [80]. These waves develop closer to nozzle exit stripping of some droplets from the jet surface (surface breakup). Post this, windward and leeward waves grow on the liquid column, causing full breakup similar to aerodynamic secondary breakup of a droplet (column breakup) [80, 81]. Liquid column is deflected due to the gas stream, gets flattened, and aerodynamic forces increase due to wave growth. This is followed by detachment of small droplets from flattened periphery. Fig. 2.12 shows a schematic of liquid jet in cross-flow.

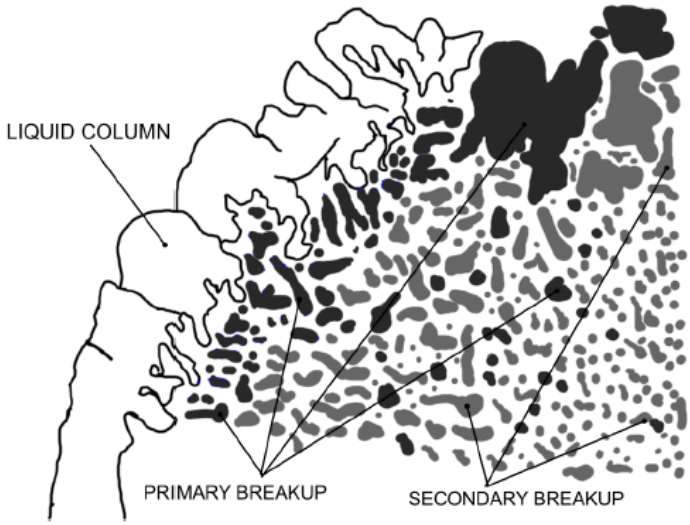

Figure 2.12: Schematic of liquid jet in cross-flow [82]

Cross-flow Weber number given by equation 2.36 is an important parameter that governs the degree of influence on jet evolution,

$$We_{cf} = \frac{\rho_{cf} v_{cf}^2 d_{cf}}{\sigma}. \tag{2.36}$$

For laminar jets in cross-flows, breakup is affected for velocities corresponding to $We_{cf} > 4$ [83]. When liquid flow has relatively higher inertia, jet turbulence dominates cross-flow effects and breakup occurs similar to turbulent jets in quiescent medium, except for some deflection along the cross-flow direction [78, 83]. We_{cf} controls the thickness of liquid structures, and the liquid Weber number is responsible for the shape of droplets/ligaments [82]. However, this parameter does not account for relative momentum between the two phases and cannot be used to see the difference in jet structures when compared with quiescent medium. For this purpose, similar to equation 2.35, quantification of liquid-to-gas momentum ratio for cross flows (M_{cf}) can be made to identify the phase with greater inertia [78]. With this, amount of change that the jet may experience can be estimated. This is given as,

$$M_{cf} = \left(\frac{\rho_L}{\rho_{g,cf}}\right)\left(\frac{v_L^2}{v_{g,cf}^2}\right) \tag{2.37}$$

where $\rho_{g,cf}$ and $v_{g,cf}$ correspond to density and velocity of cross flow gas phase respectively.

2.3.3. Estimation of surrounding flow's impact on piston cooling

(2.35) and (2.37) indicate that, both M and M_{cf} depend on corresponding gas flow velocity components, (v_g and $v_{g,cf}$ respectively). Thus, in order to analyse the effect of surrounding flow on piston cooling jet, it is important to quantify the velocity components within the crankcase. Based on their relative magnitudes, M and M_{cf} can be estimated, using which an initial prediction of jet behavior in co-axial and/or cross-flows can be done.

A sample calculation for different flow rates is presented in Table 2.2 to see the effect of co-axial flows. Liquid jet velocities from the results of Celik [3] are used for v_L. As mentioned in section 2.2.3, reciprocating piston is the main contributor within the crankcase and thus, co-axial components may be higher than cross flow elements ($V_{g,cf} < V_g$). Representative piston velocity, obtained from 1D simulations at the company, is used for co-axial gas flow velocity ($V_g \sim 10$ m/s). Similar values are not available for $V_{g,cf}$ which hinders determination of M_{cf}.

Flow rate (L/min)	**Liquid velocity, V_L (m/s)**	**Gas velocity for co-axial flow, V_g (m/s)**	**M**
3	7.1	10	408
5	11.8	10	1128
7	16.5	10	2205

Table 2.2: Sample calculation of liquid-to-gas momentum ratio (M)

Calculations from Table. 2.2 indicate that liquid phase momentum is higher than that of the gas phase. This means inertial forces of the jet are dominant, and the effects of aerodynamic interactions on primary disintegration will be minimal for the case of co-axial gas flows. Since $V_{g,cf} < V_g$, $M_{cf} > M$ and the effects of cross flows on oil jet can be expected to be even lower.

These dimensionless numbers (M and M_{cf}) are based on experiments and simulations conducted with water jets for spray applications [77, 78, 83], that operate at Reynolds numbers much higher than present conditions (given by Table 2.1.3). Also, these numbers are not liquid independent, and do not account for surface tension which is the major cohesive force, as per section 2.1.5. When surrounding air flow is present, interaction of surface tension with the eddies of gas phase, in comparison to the inertial force of the liquid,

governs the breakup process. Thus, oil may experience more disintegration (primary breakup) due to lesser surface tension, and results can deviate from these estimations made with the help of literature.

Effects of co-axial and cross flows on secondary breakup at these operating conditions are not available in literature. Post primary breakup, ligaments and droplets can experience different dynamics due to aerodynamic interactions. Ligament/droplet strip-off from the surface can increase due to shear between the two streams and droplets can move further away from the center-line resulting in increased spreading. Especially those structures that disperse, slow down because of drag and due to lower momentum, they can get carried away with the gas phase. These dynamics will affect both gallery cooling and spray cooling processes. Hence, it is important to perform preliminary CFD analyses of oil jets with co-axial and/or cross flows, to identify the degree of influence of surrounding flow on typical jet characteristics.

3

Validation

The first objective of this research work is to construct a validated CFD model for oil jets. In this chapter steps taken and analyses performed for achieving this goal are addressed. It was shown in chapter 1 that the piston cooling process can be studied by splitting it into several sub problems. This reduces the difficulties involved in simulating such a complicated cooling technique and enables an isolated investigation of oil jets using better and slightly expensive CFD methodologies like LES and VOF. With these models, it is possible to arrive at a better understanding of the physics involved in oil jet breakup, the spatial flow development and its impact on piston cooling.

In this chapter, the CFD model is validated with two test cases. The first test case (Test case - 1) is obtained through literature review, and the analysis involves reproduction of turbulent water jets of Sallam et. al [16]. The second case (Test case - 2) is an experiment conducted at DAF to determine the flow rate efficiency [3, 85] of piston cooling jets. Once the CFD model reproduces these cases with acceptable accuracy, further extensive analysis on the physics of piston cooling jets and the disintegration process is carried out. The structure of the chapter is given as follows. Description of the test cases are given in section 3.1. Computational setup common to both test case reproductions are presented in section 3.2. First the analysis is performed for turbulent water jets whose results are discussed in section 3.3, followed by reproduction of flow rate efficiency experiment in 3.4.

3.1. Description of test cases

3.1.1. Test case - 1 (Turbulent water jets)

Generally, ideal experimental or numerical references that can be used for validation are those with similar operating conditions as the problem of interest. For piston cooling, values should be same as those in Table 2.1.3. However, as mentioned in section 2.1.1, there is dearth of data in literature corresponding to piston cooling conditions and hence, study with closest match is selected for validation. Since, turbulence at the jet exit is found to have major influence on the breakup process [17, 22], turbulent water jet of Sallam et. al [14] is chosen. This is an experimental study, operating at Re $\sim$ 6000 – 1.36 x 10^5 and We $\sim$ 200 - 4 x 10^4, where water is injected into air at standard atmospheric conditions ($\frac{\rho_L}{\rho_g} \sim 860$). For present analysis, the test case with Re = 6000 and We = 214 is found to have the closest match and is reproduced using the LES model. Difference in Re between this case and oil jet is not a matter of concern as both jets are fully turbulent and the dominant forces are expected to be the same for a given liquid [16, 22]. However, difference in We is of the order, O $\sim 10^2$ because of increased surface tension of water (σ = 0.070 N/m) when compared to oil (σ = 0.024 N/m). Thus, water is expected to be more resistant to breakup than oil at same Re.

3.1.2. Test case - 2 (Flow rate efficiency experiment-DAF)

DAF conducted an experiment to determine the amount of oil entering the cooling gallery orifice, placed at a fixed distance representing TDC of the piston. This was quantified using flow rate efficiency (η) given by,

$$\eta = \frac{FR_{orifice}}{FR_{nozzle}} x100\% \tag{3.1}$$

where $FR_{orifice}$ is the flow rate of oil entering the gallery and FR_{nozzle} is the flow rate of oil injected through the nozzle. Fig.3.1 illustrates the experimental setup and Fig 3.2 shows the efficiency results of six nozzles for different FR_{nozzle} between 3 L/min and 7 L/min. Average of these results is also presented. All nozzles have the same nominal diameter ($d = 0.003m\pm$ tolerance) and are representative of production clearance. Experimental uncertainties are unknown and the spread in efficiency across six PCJs increases with increase in flow rate. This could be due to enhancement in turbulence of the jet which results in chaotic behavior and more spreading. Details about the experiment can be obtained from Celik [3] and DAF report [85].

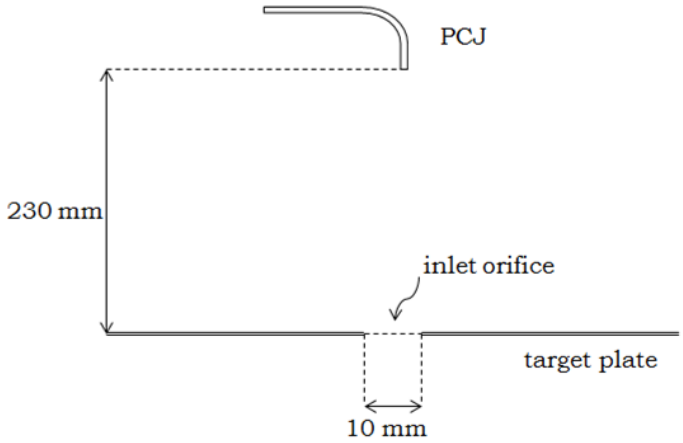

Figure 3.1: DAF experimental setup[85].

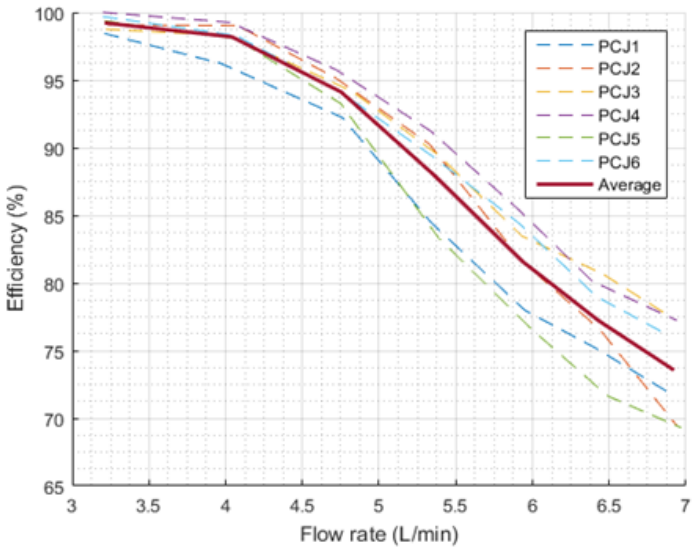

Figure 3.2: Flow rate efficiency results for 6 different PCJ nozzles [3].

3.2. Computational setup

In this section, steps taken to construct the CFD model using StarCCM+ are presented. Note that this simulation setup is common to both test cases and modifications specific to each test case are mentioned before presenting respective results. The computational domain and meshing strategies are discussed in section 3.2.1. Boundary conditions are briefed in section 3.2.2, and various physics models and solver settings are mentioned in 3.2.3.

3.2.1. Geometry and meshing

Geometry

Liquid jet breakup is a three-dimensional phenomenon. Especially, jets in SWI regime are not axisymmetric and hence, a 3D domain is necessary for analyses. A nozzle with circular cross-section and a cylindrical domain is used. Fig. 3.3 shows the 3D domain and Fig. 3.4 shows its 2D schematic. Dimensions are given as dependents of nozzle diameter, d, as it is different for the two test cases (Table 3.1). Length of the domain in Fig. 3.4 is based on actual distance from the nozzle exit to TDC which is 76.67d (0.23 m). The small portion beyond TDC is for removing the effect of outlet, i.e., to ensure that solution at TDC is unaffected by any numerical backflow. Width of the domain (along y- and z- directions) is based on boundary distance used in literature, and most researchers have used between 8 x d and 15 x d [77, 78, 86]. In this study a width of 14 x d is selected for constructing a computationally affordable domain.

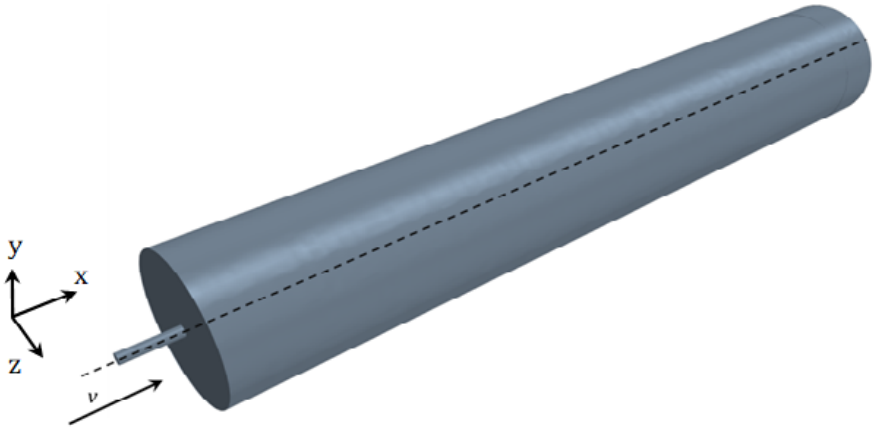

Figure 3.3: Three dimensional domain used for oil jet simulation

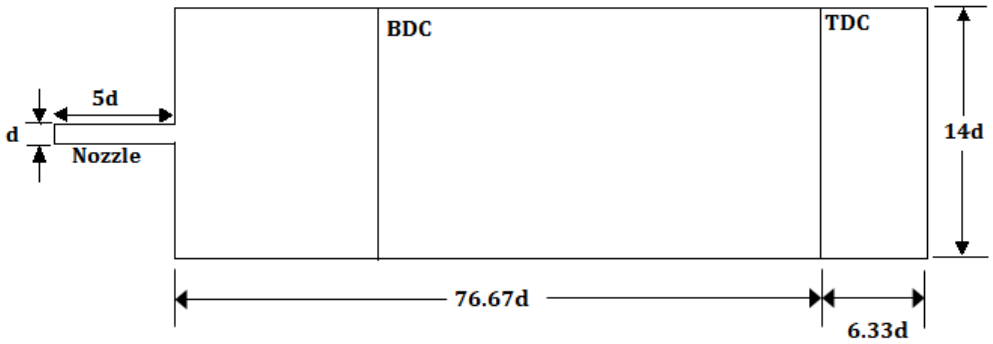

Figure 3.4: Two dimensional schematic of the domain with dimensions

Meshing

Results obtained using LES are always sensitive to mesh resolution. Cell size in the region of interest impacts SGS modelling and influences discretization errors. Varying the grid size will impact the quality of simulation, as explained in section 2.1.8. Based on different criteria mentioned in 2.1.8, cell sizes (h) are selected for the two test cases and are shown in Table 3.1. A comparison with the previous study by Celik [3] is also made. For satisfying criteria -1, Kolmogorov's and Taylor micro scales are calculated analytically using expressions from [45, 46] and predicted by precursor RANS analysis given in Appendix. A.

- **Criteria – 1**: ($\eta < h < \lambda$) 0.2 x 10^{-4} m < h < 2 x 10^{-4} m
  - **Test case - 1**: 0.2 x 10^{-4} m < h < 2 x 10^{-4} m
  - **Test case - 2**: 0.2 x 10^{-4} m < h < 2 x 10^{-4} m
- **Criteria – 2**: $\left(\frac{d}{12} < h < \frac{d}{20}\right)$
  - **Test case - 1**: 0.95 x 10^{-4} m< h < 1.6 x 10^{-4} m,
  - **Test case - 2**: 1.5 x 10^{-4} m < h < 2.5 x 10^{-4} m

Case	**Nozzle diameter,** d (m)	**Grid size in the jet region,** $h(10^{-4}m)$	**Total Cell count** (Millions)
Test Case-1	0.0019	1.17	9.4
Test Case-2	0.003	1.56	9.6
Celik	0.003	2.5	6.1

Table 3.1: Mesh settings in the jet region, and total cell count

It can be seen that the previous study [3] has cell size at the upper limit of criteria-2 which is definitely insufficient for multi-phase analysis involving droplets (section 2.1.8). Also, the study lacks proper validation. Celik [3] followed Moghe et. al [56] for validating his CFD model, and the latter provide spreading measurements obtained from instantaneous snapshots and 2D-image analysis that are not reliable. Though visual inspection of both results give qualitative agreement, deficiency in quantitative outcomes impacts the trustworthiness of his model. Celik's analyses were also hindered by the computational power which was lower than the current facility at DAF Trucks N.V.

Improved facilities allow for application of sizes given in Table 3.1 that result in total simulation time of less than 48 hours. Total computational time is determined by performing scalability analysis whose results are shown in appendix A. Thus, criteria-1, 2 and 3, given in 2.1.8, are satisfied in each case. Any further refinement results in deviation from criteria - 3, affecting time management of subsequent analyses. Hence, these sizes are used as preliminary values for discretizing the region of interest which is showin in Fig. 3.9 (b). This zone is constructed by using the dimensions obtained from spreading estimation of the jet from previous studies [3, 56]. Based on the quality of simulation and droplet size results obtained, the need for grid refinement is assessed and an isolated analysis is performed.

Structured grids are constructed owing to their low memory requirement and reduced computational cost. Also, it is easier to identify LES cell size with hexahedrons when compared to polyhedrons, and simplifies volumetric grid construction. For jets in SWI, turbulence at the jet exit controls its evolution, as explained in sections 2.1.1 and 2.1.4. For this reason, it is important to sufficiently refine the nozzle, as the development of the flow and boundary layer within, control the turbulence at the exit. Prism layers are used to create fine mesh in the near-wall region and two different grids are tested to see the effect on nozzle flow. The base size is maintained the same as grid size given in Table 3.1 and the test is performed for oil jet at 7 L/min (Turbulent flow condition). Table 3.2 summarizes the settings used, and 2D schematic of the grids are shown in Fig. 3.5.

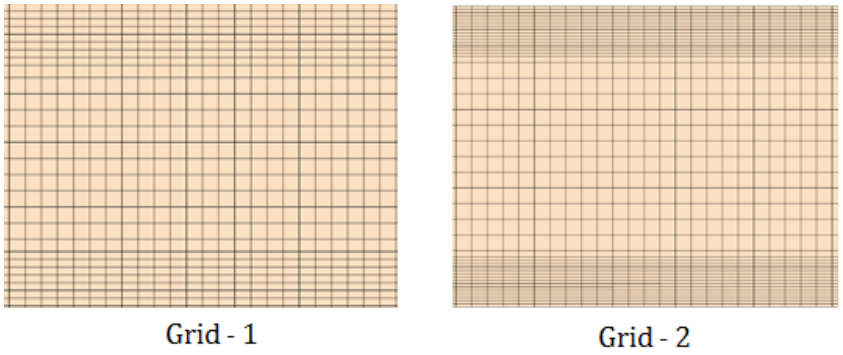

Figure 3.5: 2D mesh schematic of grids tested within the nozzle

Case	**Base size,** $h(10^{-4}m)$	**No. of Prism Layers**	**First cell distance** $(10^{-4}m)$
Grid-1	1.56	8	0.62
Grid-2	1.56	15	0.33

Table 3.2: Mesh settings for testing the effect on nozzle flow

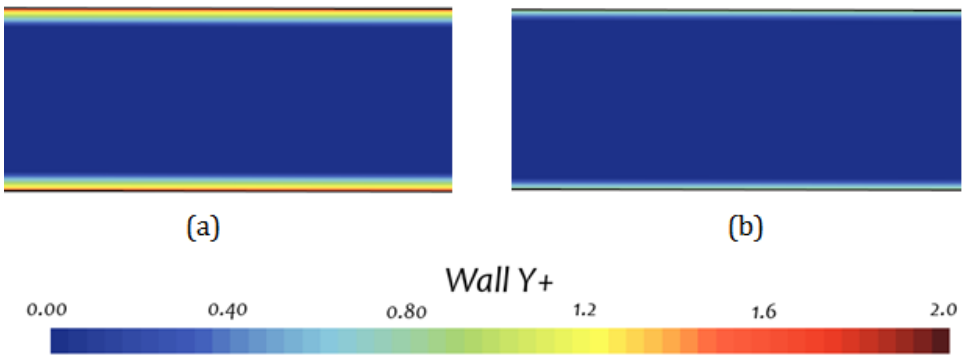

Figure 3.6: Wall y^+ results obtained for (a) Grid - 1 and (b) Grid - 2.

Prediction of wall bounded turbulent flows is dependent on accurate modelling of near-wall flow which can be verified with the dimensionless parameter, wall y^+ [87]. Generally, $y^+ < 5$ is necessary in the region known as viscous (or) laminar sub-layer [45] and $y^+ \sim 1$ is most desirable [87]. Results obtained from present analysis, in Fig. 3.6, indicate that these requirements are well satisfied by both the grids. y^+ is very much less than 5 in the near wall region of Grid-1 and is less than 1 for Grid-2 due to finer resolution. Velocity profile and turbulent kinetic energy within the nozzle are plotted as a function of normalized radial distance from centerline (r/d = 0) to the wall (r/d = 0.5) due to flow symmetry, and the results are presented in Fig. 3.7. Flow field produced by both the grids are similar (<10% difference) based on values in Fig. 3.7(a). Accuracies are ~ 8% and ~ 6% for Grid - 1 and Grid - 2 respectively. Turbulent kinetic energy within the nozzle (Fig. 3.7(b)) also closely match for both grids and minor differences (~ 8%) in the vicinity of the wall (around r/d ± 0.35) are considered to be negligible. This can be better understood with Fig. 3.8 where the near wall region is magnified and the same results are plotted with better resolution, for both grids.

Usage of settings same as Grid -2 is possible for the full LES model (Fig. 3.3) only by increasing the total computational time above 48 hours, thereby violating criteria - 3. Thus, the resolution provided by Grid-1 is considered to be sufficient and the above results warrants its usage in further analyses. Literature also states that for jets with density ratio greater than 500, aerodynamic interactions have least impact on breakup, which is applicable for both test cases. This enables construction of growing mesh outside the jet

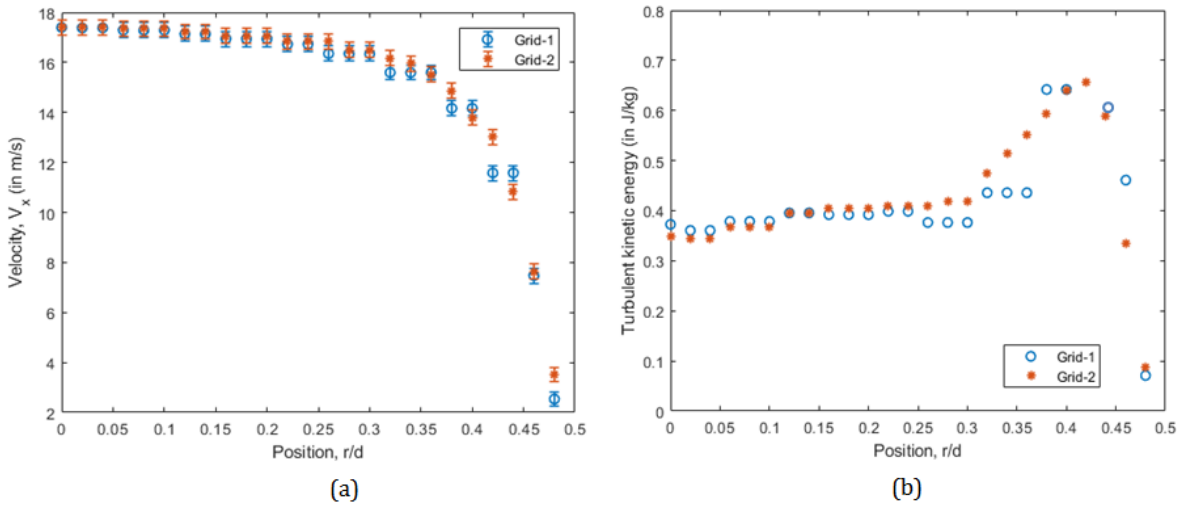

Figure 3.7: (a) Velocity profile and (b) Turbulent kinetic energy within the nozzle

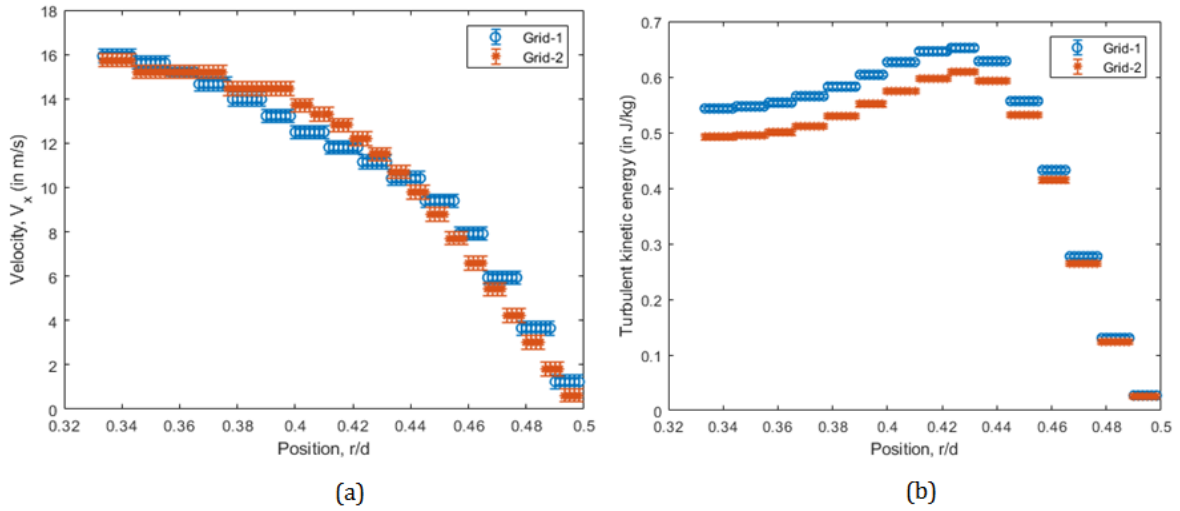

Figure 3.8: (a) Velocity profile and (b) Turbulent kinetic energy within the nozzle

region with maximum cell size of $2x10^{-3}$ m and least cell size of $5x10^{-4}$ m, resulting in a computationally viable simulation. 2D schematic of the final mesh is shown in Fig. 3.9 (a).

3.2.2. Boundary conditions

The nozzle walls are assigned to be no-slip and adiabatic. Nozzle inlet boundary is set to velocity inlet condition. Precursor RANS simulations are performed to obtain velocity and turbulence data at the nozzle inlet. This method used for obtaining inflow data is the same as used by Celik [3]. Details are given in Appendix. B. Other boundaries are set to pressure outlet, as shown in Fig. 3.9, with atmospheric pressure (101325 Pa) as reference and backflow allowed only for the gas phase.

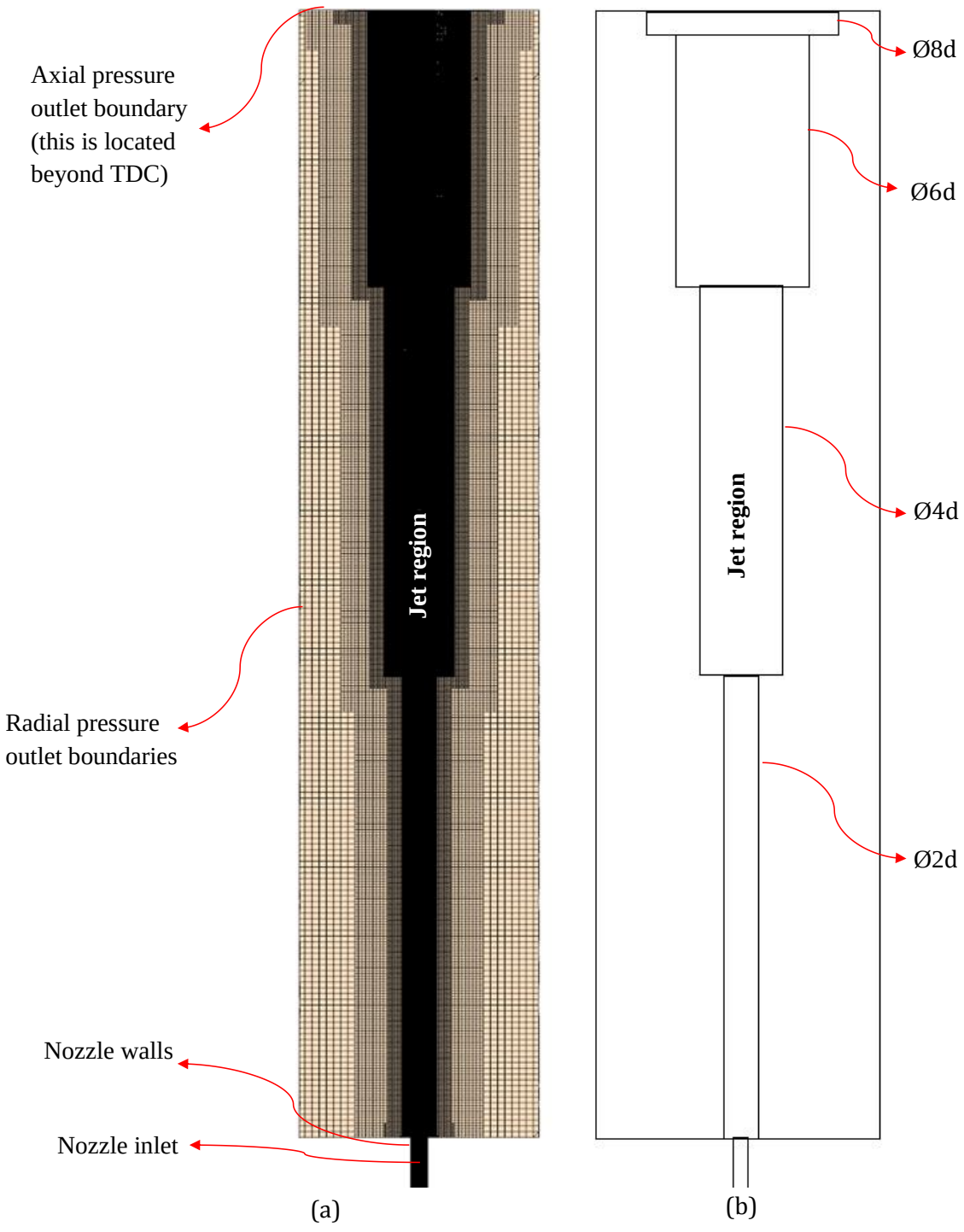

Figure 3.9: (a) 2D view of the mesh with fine mesh in the jet region and growing mesh outside and (b) Jet region - here grid sizes from Table 3.1 are used

3.2.3. Physics models and solver settings

Physics models

Two-phase flow is represented by Eulerian multi-phase model. Oil with homogeneous and constant properties is the working liquid phase. Since the gas phase is quiescent and is found to have little impact on the jet structure [13, 33], air with constant density at standard atmospheric conditions is used. Liquid jet is reconstructed using the interface capturing method, Volume Of Fluid (VOF), described in section 2.1.8. Default VOF-VOF multiphase interaction [41, 84] and surface tension modelling are selected [41]. LES methodology with the WALE sub-grid model is used for turbulence modelling. Gravity is enabled and is assigned along the negative-x direction emulating upward trajectory of actual oil jets in engines. For quantifying droplet sizes, blob detection model available in StarCCM+ is used for determination of droplet/ligament diameters.

Solver settings

Segregated flow solver and implicit unsteady solvers are used with second order discretization schemes. Time step is estimated by calculating CFL number which is given as,

$$CFL = \frac{u\Delta t}{h} \tag{3.2}$$

This number must be < 0.5 for VOF models, and in the present study $CFL < 0.2$ is used following the recommendations of Celik [3].

3.3. Validation of test case - 1

In this section, test case - 1 of turbulent water jet is reproduced with the LES model. Computational domain of this model is same as given in Fig. 3.3 and 3.4, with nozzle diameter, d = 1.9 x 10^{-3} m. Mesh settings are given in Table 3.1 and the models used are the same as in section 3.2.3. Time step used for this case is 1 x 10^{-5} s which ensures $CFL < 0.2$ for the present operating conditions.

3.3.1. Initialization and sampling

Every LES model contains two stages: initialization and sampling. Initialization is the phase taken by the simulation to remove the effect of initial conditions after which, the solution stabilizes and oscillates about an average value. Sampling is the solution-averaging phase. This is carried out until the quantity of interest converges to a certain average, which does not change with further increase in sample size. In the present analysis, these phases are identified by computing plane averaged liquid mass flow entering the orifice at TDC. Fig. 3.10 shows instantaneous and mean mass flow results of water, plotted versus physical time. This quantity is selected as it is useful to determine the mass imbalance of the CFD model and is also one of the main parameters of interests for piston cooling analyses.

Typical initialization and sampling stages are marked in Fig. 3.10. Mass flow remains zero until flow reaches the orifice plane. Sampling stage begins when the solution converges to a particular value (or expected value), which is 4.03 x 10^{-3} kg/s for this case. This stage begins around 0.32 s. Post 0.52 s, the average results do not vary with time and solution is converged. 1.2 % mass imbalance is obtained at TDC and this is considered to be excellent for the present configuration as further reduction is achievable only through mesh refinement that comes at the cost of exceeding criteria-3 of section 2.1.8.

3.3.2. LES Quality assessment

The next step is to verify the quality of LES model. This is done based on the criteria given by (2.27) and (2.28). Fig. 3.11 shows the results of LES quality metric (γ). In most parts of the domain, this value is greater

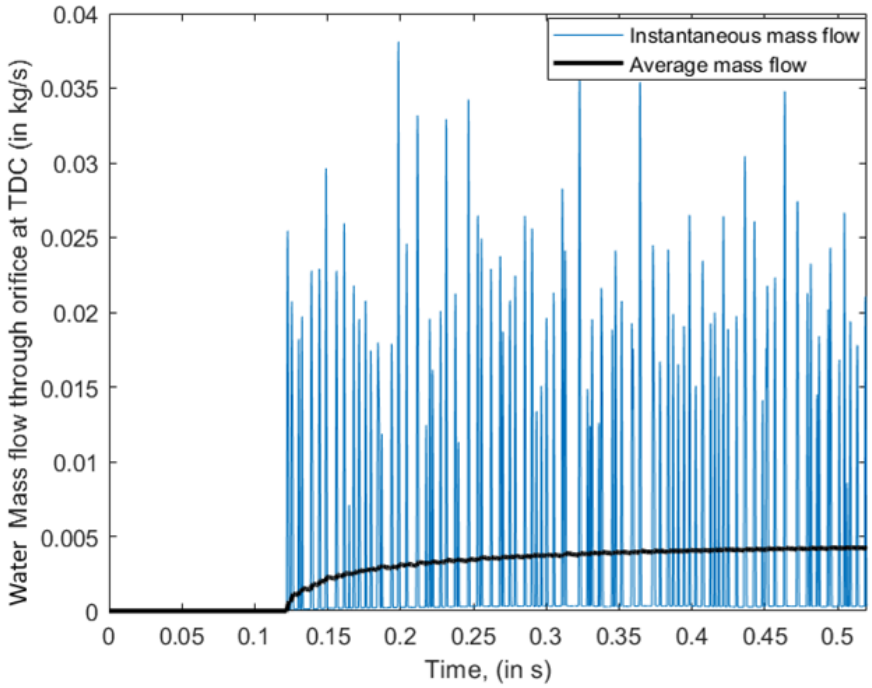

Figure 3.10: Initialization and sampling stages for validation of test case - 1

than 0.8. However, near the jet exit and around the liquid-gas interface $\gamma < 0.8$ which means that the turbulent kinetic energy of large scales is resolved insufficiently by the current mesh in those regions.

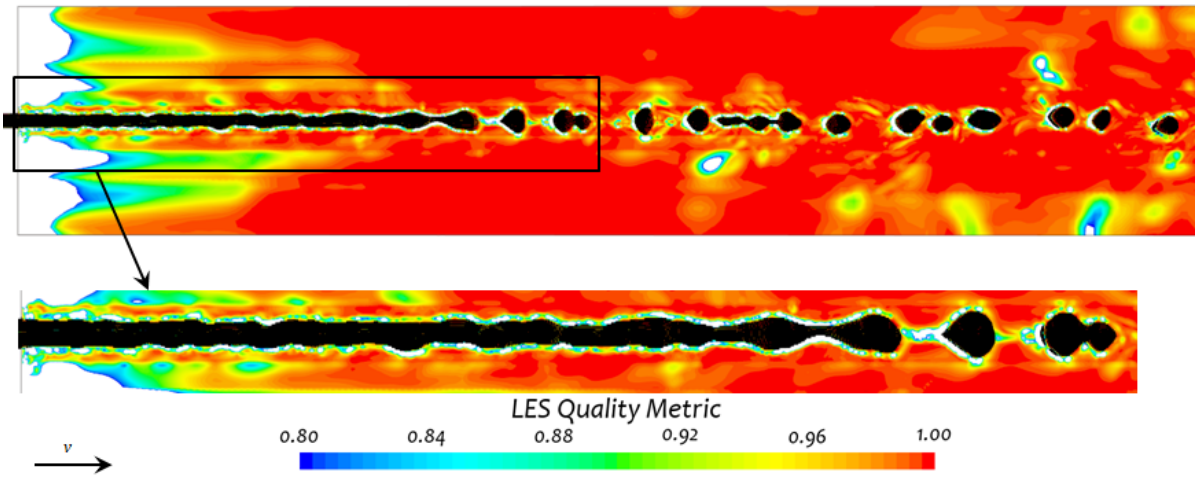

Figure 3.11: LES quality metric (γ) results

This indicates that interaction due to eddies between the two phases is not captured completely within the region of interest and hence, sufficient condition is not satisfied locally. This can be overcome only by grid refinement which comes at the cost of computational effort. However, at these operating conditions, eddies present within the liquid phase are responsible for breakup and not those at the interface (or in gas phase), which will keep the overall jet structure and nature of breakup to be largely unaffected with potential grid refinement. The same argument is also applicable to oil jets. Droplet sizes may be affected but the contrary is obtained with validation results presented in section 3.3.4.

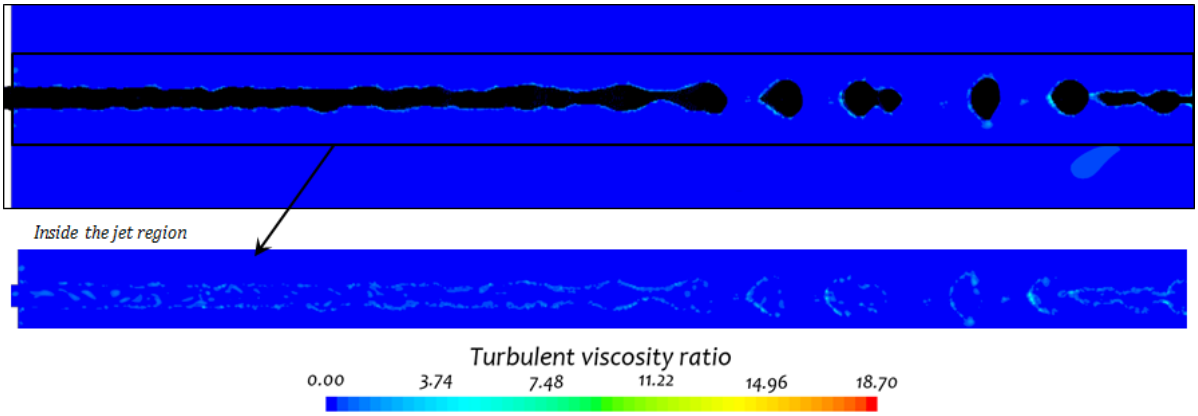

Figure 3.12: Turbulent viscosity ratio results

Results of turbulent viscosity ratio are presented in Fig. 3.12. This is much less than 20 in and around the jet, meeting the recommended criteria. Thus, the necessary condition is satisfied with current mesh settings and results produced are reliable for industrial standards, allowing continuation of further analysis with this LES model. This is ensured by the consistency of qualitative and quantitative observations made in the following sections.

3.3.3. Qualitative results - Jet structure

Iso-surfaces with the threshold volume fraction of liquid phase 0.99 and above, is used for plotting the jet structure. This value helps in reconstructing the liquid core by identifying the cells that are completely filled with oil, which is necessary to locate primary breakup. A comparison of iso-surfaces with several threshold values are shown in Fig. 3.13 for the water jet. No significant differences can be observed in the overall appearance. The iso-surface boundary is slightly modified in each case and it approaches towards the interface when the threshold is set to > 0.1. Nevertheless, for the purpose of visualization and qualitative description, these changes can be neglected and the main liquid core is retained by using the threshold of 0.99. This selection has no impact on quantitative results. Based on Re and Oh, water jet is found to lie in FWI regime (section 2.1.3) and is confirmed by an instantaneous snapshot of the jet structure shown in Fig. 3.14,

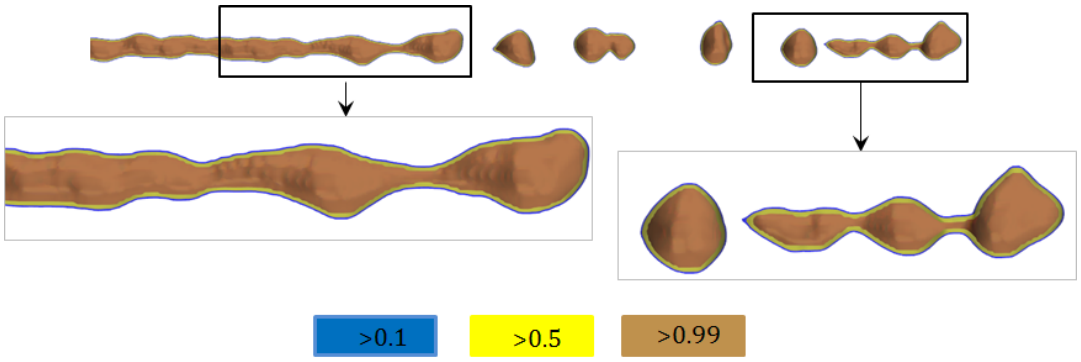

Figure 3.13: Jet structure with different threshold iso-surfaces

Jet schematic is similar to the FWI example in Fig. 2.2 of section 2.1.3. After injection into quiescent atmosphere, unstable waves (sinuous waves) develop on the surface like any typical FWI jet. Cohesive forces due to surface tension try to keep the jet intact and does not allow the waves to develop rapidly, avoiding chaotic disintegration. This results in simple Rayleigh breakup (primary breakup)[3, 16] and droplet pinch-off. Breakup point can be distinctly identified and post disintegration, secondary breakup into further small

structures is absent. These results are consistent with the description in section 2.1.3 and with the observations of Skillone [28]. Droplets that form are generally of similar sizes in terms of order of magnitude because of lower value of We (We ~ O(100)). As seen in section 2.1.5, at this We, large scale eddies present in the liquid phase are responsible for droplet formation leading to the observation of bigger liquid structures. These results are consistent with the theory discussed in section 2.1.1.

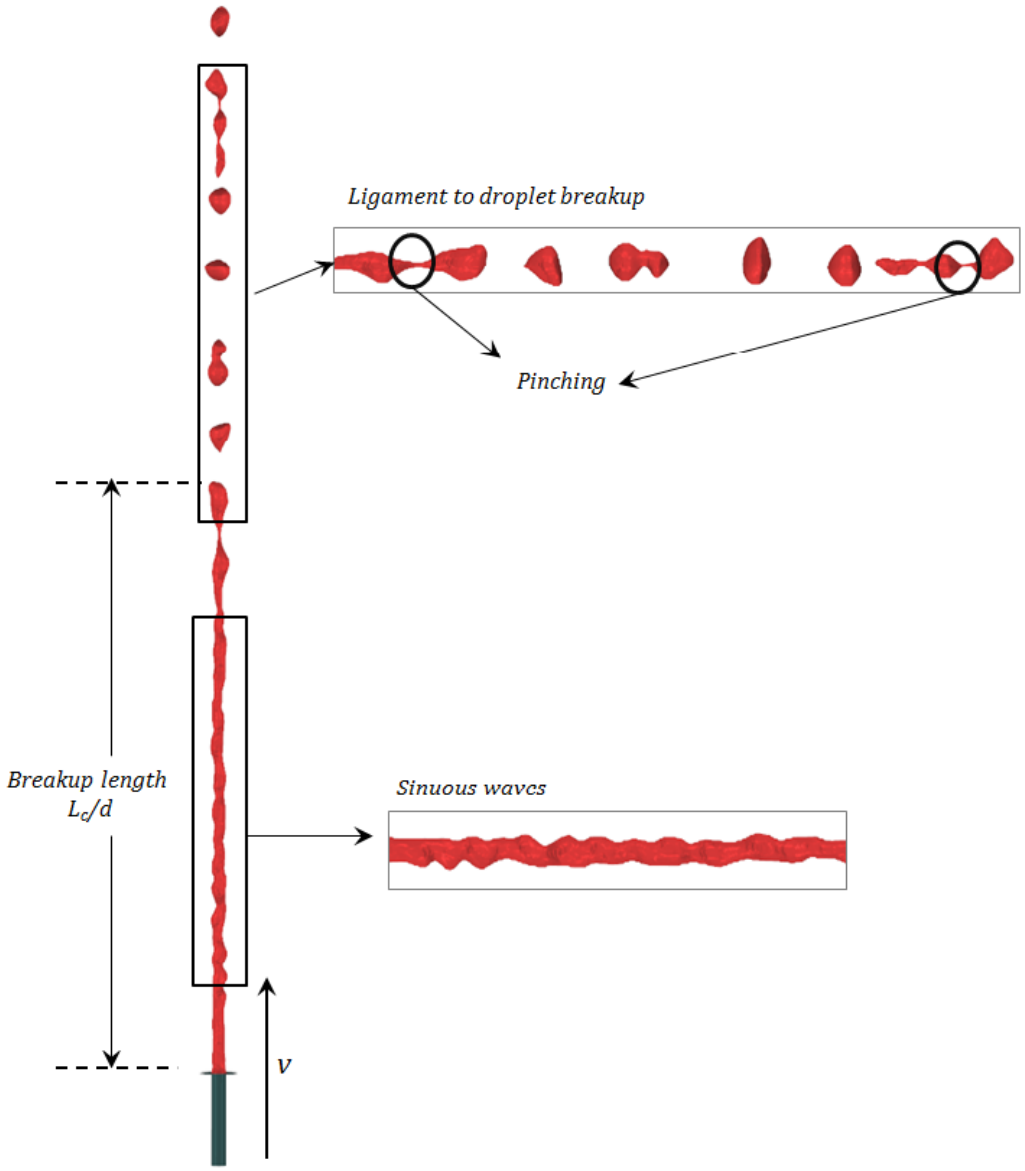

Figure 3.14: Jet structure obtained from LES analysis of test case - 1.

3.3.4. Quantitative results

Parametric validation is performed by predicting breakup length and droplet sizes normalized by nozzle diameter (d) and the results are presented in this section.

Breakup length

Breakup length or liquid core length (L_c/d), indicated in Fig. 3.14, is obtained by plotting volume fraction of liquid along the jet axis. The first point along this axis where volume fraction goes to zero is the breakup point whose distance from the nozzle exit gives the breakup length. This is tracked as a function of time in the simulation as shown by Fig. 3.15.

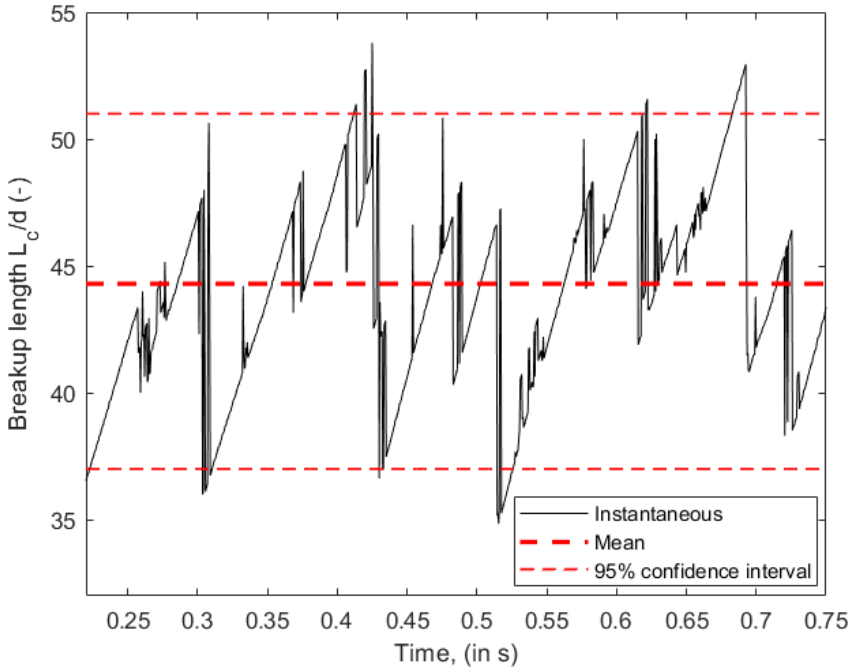

Figure 3.15: Breakup length sampling. (Black) Instantaneous and (Red-dashed) Mean results

Results are obtained through sampling and the following equation is ised to represent the average result (mean) and the accuracy,

$$\left(\frac{L_c}{d}\right) = \left(\frac{L_c}{d}\right)_{mean} \pm z^* . \frac{\sigma}{\sqrt{N}} \tag{3.3}$$

where σ is the standard deviation, N is the number of samples and z^* is the indicator of confidence level. In present analysis, after the initialization phase, solution fluctuates about an average value of (L_c/d)= 44.3. Accuracy is determined based on standard deviation with 95 % confidence level (corresponds to, z^* = 1.96) and is found to be ± 7.23.

Cases	**Breakup length,** $\left(\frac{L_c}{d}\right)$
Present study	44.3 (±7.23)
Sallam et. al [16]	50.0 (±2.5)
Grant and Middleman [22]	47.4

Table 3.3: Breakup length results

Results from Table 3.3 indicate that the computed breakup length differs by 11 % when compared with the experimental results of Sallam et. al [16], and by 7 % from the correlation of Grant and Middleman [22] (given by (2.8)). This shows that the LES model constructed for this study reproduces liquid core lengths sufficiently.

Droplet sizes

Apart from LES quality, grid resolution also affects droplet sizes. Typically, liquid structures are restricted to characteristics lengths above LES grid size, and smaller ligaments/droplets that may be present in the real flow, cannot be captured. Limitation posed by VOF and HRIC models to maintain sharp interface, may combine two droplets, if their peripheries lie inside a single cell [41] leading to formation of a single big structure. Due to these restrictions, the average droplet size captured by the CFD model (in Fig. 3.14) may be larger than that of actual water jet. This can be verified only by quantifying droplet sizes which is done in Table. 3.4. Results are compared with correlations mentioned in section 2.1.7 as no data is available from Sallam et. al [16].

Cases	**Mean diameter, SMD**	**Maximum diameter,** $d_{0.99}$
Present study	1.631 (±0.12)	3.621 (±0.27)
Harmon [36]	1.636	-
Miesse [37]	-	3.973

Table 3.4: Droplet size results - normalized with nozzle diameter

This indicates that the current grid size is sufficient to capture droplets of this test case. The fact that the mean and maximum diameters are an order higher than the grid size used in the jet region (Table 3.1) is an indication that the present resolution is enough to avoid any numerical droplet coalescence imposed by VOF model's limitation. However, the same mesh need not be sufficient for jets at different operating conditions that have chaotic breakup and very fine droplets. This yields grid resolution to be subjective to the fluid and the flow rate, and this will be dealt in the upcoming chapters. Thus, the ability of the CFD model, to capture essential physics and jet structure, is verified based on appreciable reproduction of test case - 1 via qualitative and quantitative observations.

3.4. Validation of test case - 2

Reproduction of the second test case is done with the objective of performing LES of oil jets at selected flow rates and validate the results of DAF experiment shown in Fig. 3.2.

3.4.1. Modifications to the numerical setup

Five flow rates are selected and the same CFD model, constructed and validated for test case - 1, is used with some changes. First, the geometry is modified by setting the nozzle diameter, d = 0.003 m, to represent typical PCJ nozzles. This expands the volume of the domain shown in Fig.3.3, when compared to the previous test case. Mesh is created with the cell sizes given in Table. 3.1. Note that the jet-region indicated in Fig. 3.9 is also larger due to increase in nozzle diameter. This is followed by switching the liquid phase from water to engine oil, whose properties are given in Table. 3.5.

Density	810.1(kg/m^3)
Dynamic viscosity	$9.54210^{-3}(N/m/s)$
Specific heat per unit mass	2170$(J/kg/K)$
Thermal conductivity	0.128 (W/m/K)
Surface tension	0.024 (N/m)

Table 3.5: Engine oil (10W-30) properties at 100°C

Inflow boundary conditions are modified by running the precursor simulation with oil at corresponding flow rates. Characteristics of the jets, obtained from these simulations, at different flow rates, are summarized in Table. 3.6. Jets are classified based on their nozzle exit Reynolds number as laminar or turbulent.

Generally, when Re < 2100, the jet is laminar and Re > 4000 is considered as turbulent. Intermediate Reynolds numbers are in the laminar-to-turbulent transition regime [7, 88]. Corresponding location of the jets within the breakup regime classification of section 2.1.3 is represented through Fig. 3.16.

Flow rate (L/min)	**Velocity** (m/s)	**Re** (-)	**We** (-)	**Oh** (-)
3	7.1	1800(Laminar)	5100	0.0395
4	9.4	2400(Transition)	8950	0.0395
5	11.8	3000(Transition)	14100	0.0395
6	14.1	3600(Transition)	20130	0.0395
7	14.1	4200(Turbulent)	27600	0.0395

Table 3.6: Jet characteristics at different flow rates

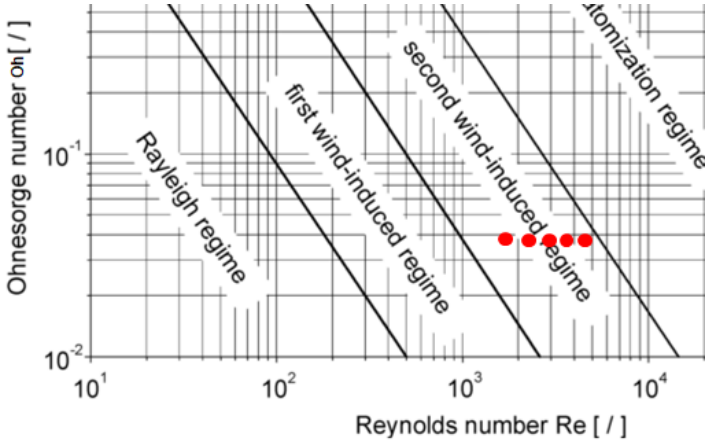

Figure 3.16: Red dots indicating that the five tested flow rates lie in SWI regime

As mentioned in section 3.2.3, time step for each flow rate is set such that the CFL limiting condition recommended by Celik is met, i.e., $CFL < 0.2$. Based on characteristic jet velocity obtained from precursor simulations, time step is calculated and presented in Table. 3.7.

Flow rate (L/min)	**Velocity** (m/s)	**Time Step** (10^{-6} s)	**CFL** (-)
3	7.1	4	0.182
4	9.4	3	0.181
5	11.8	2.5	0.189
6	14.1	2	0.181
7	14.1	1.75	0.185

Table 3.7: Time step used and CFL number for different flow rates

3.4.2. LES quality assessment

Fig. 3.17 and Fig. 3.18 show LES quality results for oil jet. Both necessary and sufficient conditions given by (2.28) and (2.27) respectively, are presented for the case of 7 L/min. Results for other flow rates are similar and are given in Appendix. C. Fig. 2.28 confirms that the LES model satisfies the necessary condition substantially. Turbulent viscosity ratio is always less than 20 in and around the jet. This indicates that, according to industrial standards mentioned in section 2.1.8, the current grid size is small enough to resolve large scale eddies in the region of interest. Away from the jet, the ratio exceeds 20 at few locations where coarser mesh is used. However, these values are still less than 100 meeting the recommended criterion and establishing the robustness of the LES model.

Fig. 3.18 shows results of LES quality metric, γ. This is the sufficient condition and is satisfied in most parts of the jet where, $\gamma > 0.8$. However, there are some cells with poor quality ($\gamma < 0.8$) within this region and along the interface. This shows that turbulent eddies and corresponding liquid structures at those locations are not well resolved, and this may impact disintegration and ligament/droplet production. To verify the impact of quality on the disintegration process, it is important to perform grid refinement study and this is discussed further in detail in section 4.4.

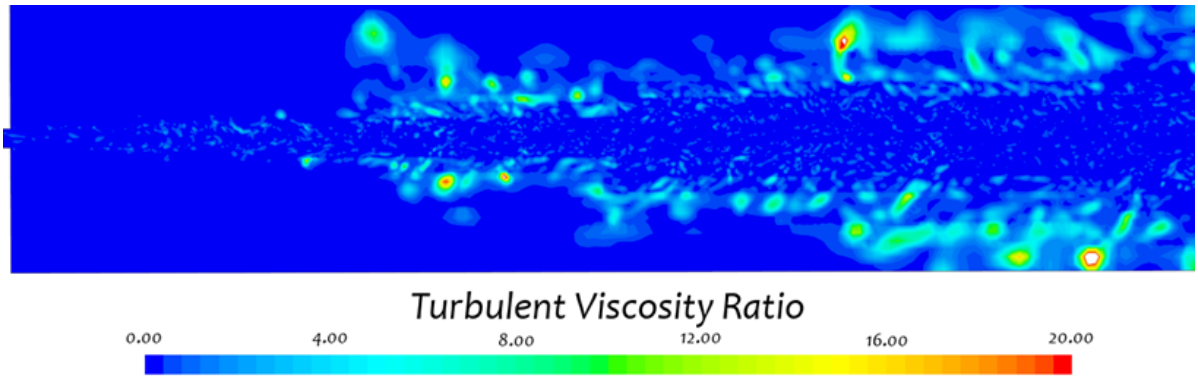

Figure 3.17: Turbulent viscosity ratio for oil jet at 7 L/min

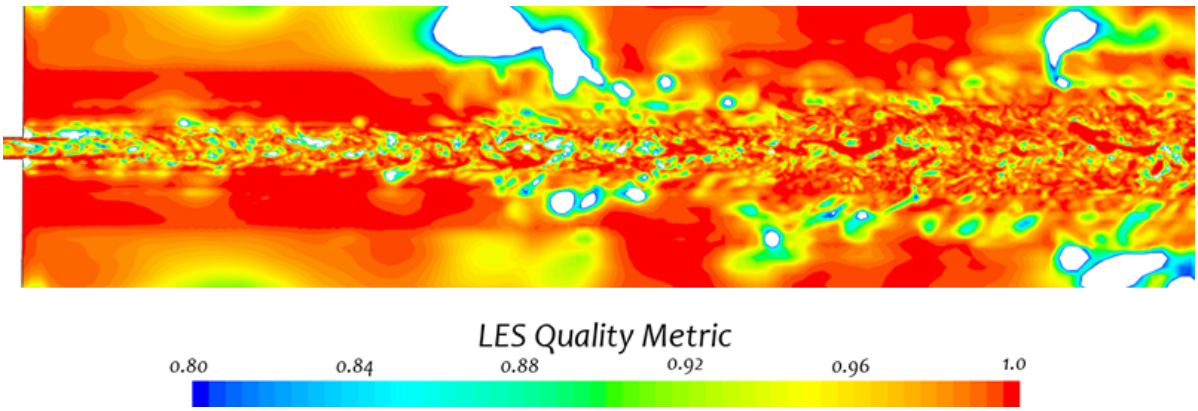

Figure 3.18: LES quality metric (γ) results for oil jet at 7 L/min

Table 3.8 shows the percentage of cells with poor quality in the region for each flow rate. Only a very few cells have $\gamma < 0.8$ as the maximum is always less than 2 %. These numbers will reduce with further grid refinement which comes at the cost of computation time exceeding the limit set by criteria-3 of section 2.1.8. This is discussed further in section 4.4 and 4.5. Outside the jet, several local zones have poor quality due to coarseness of the grid employed. But these regions correspond to eddies of gas phase which do not impact jet evolution, based on the effect of aerodynamics discussed in section 2.1.4.

Flow rate (L/min)	% **of cells with** $\gamma < 0.8$
3	0.6 (±0.5)
4	1.0 (±0.8)
5	0.8 (±0.6)
6	1.0 (±0.5)
7	1.2 (±0.5)

Table 3.8: % of cells with poor quality in the jet region according to sufficient condition

3.4.3. Flow rate efficiency results

Fig. 3.19 presents the efficiency obtained from LES for different flow rates in comparison with DAF experiment. It can be seen that LES results are in excellent agreement as efficiency for the tested flow rates lie within the experimental spread.

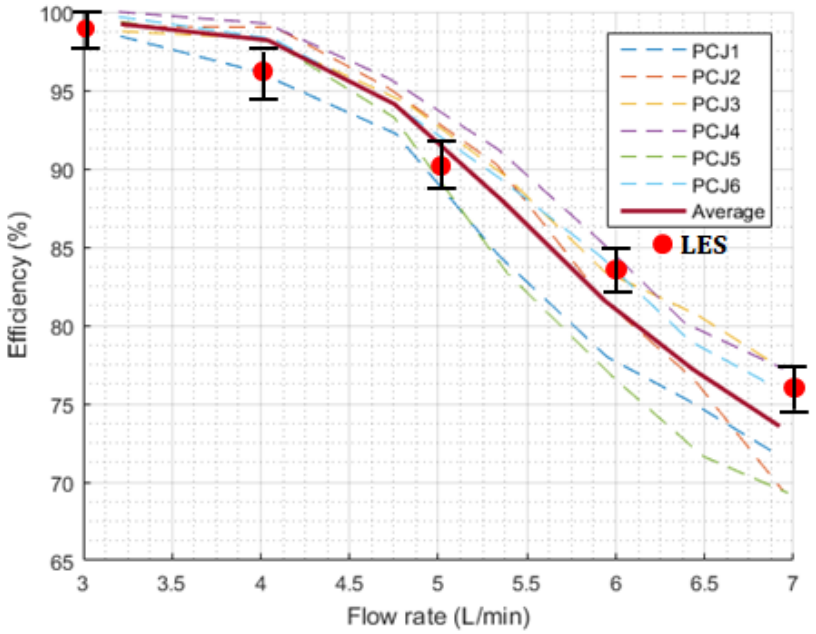

Figure 3.19: Flow rate efficiency validation. Present study (LES) vs DAF experiment (PCJ1 - PCJ6)

In the simulation, mass flow rate of oil entering the orifice at TDC is sampled, and divided by mass flow rate at the nozzle, to determine the sampled efficiency. Error bars are found by determining standard errors with 95% confidence levels, similar to (3.3). These bars correspond to a maximum variation of approximately, $\eta \pm 2\%$ for 4 L/min, 5 L/min and 6 L/min, and a minimum of $\eta \pm 1\%$ for 3 L/min and 7 L/min. Jets at the extreme are either laminar or turbulent, as indicated in Table. 3.6. Intermediate flow rates fall under transition regime and these jets are found to have maximum fluctuation in the solution. This may be reduced with further increase in sampling time with which the intermittent behaviour can be better captured.

Minor differences between the LES results and the experiment, can be attributed to the enhanced turbulent behavior of the jet at higher flow rates, and its impact on efficiency may be reduced by increasing the sample size or mesh resolution. Also, uncertainties during the experiment such as geometric inaccuracies of the nozzles, shorter experimental runtime, and/or measurement errors can be reason(s) for this observation. Nevertheless, efficiencies obtained with this LES model lie within the minimum and maximum experimental results, validating the DAF experiment appreciably. Although, similar results are produced by Celik [3], there is lack of proper explanation for the accuracy of his results apart from insufficient grid resolution, and these are clearly amended in the present study.

3.5. Conclusion

One of the main objectives of this research work is to construct an LES model for oil jets that is well validated, and this goal is successfully achieved by reproducing two test cases. With the help of extensive literature review, appropriate LES grid sizes are selected based on several criteria. The CFD model is built with these preliminary values and some recommendations provided by Celik [3] and StarCCM+ [41, 48, 53, 59].

The first test case of turbulent water jet which is obtained from literature, is simulated with this model.

Validation results and conclusions derived from this analysis are summarized as follows,

- Qualitative analysis of this case shows that the jet characteristics are consistent with observations made in literature.
  - Structure of the jet obtained resembles jets in FWI regime.
  - Typical characteristics such as sinuous waves, and ligament to droplet formation are captured by the CFD model.
- Validation performed with quantitative analysis of breakup length shows that the model is able to produce results similar to the test case with high levels of accuracy.
- Grid size used for this case is sufficient to capture typical droplets present in water jet and this is proved by conformity in droplet diameter results with correlations. However, the same mesh setting may not be sufficient for different jets which exhibit chaotic disintegration with formation of very small liquid structures.

The second test case, which is validation of DAF's flow rate efficiency experiment, is carried out by simulating oil jets at five selected flow rates. The same model with some modifications specific to this case is used and the results obtained are concluded as follows,

- Flow rate efficiency results obtained with the LES model are in excellent agreement with DAF experiment and also have appreciable levels of accuracy.
- The results show a decreasing efficiency with increasing flow rate which is a result of increased chaotic nature of the jet due to increasing jet turbulence. This will be discussed in detail in the upcoming chapter.

For both test cases, the LES quality results show that

- With the current mesh size, the CFD model is able to satisfy the necessary condition substantially, as the turbulent viscosity ratio remains always less than 20 in all parts of the domain.
- The sufficient condition is achieved in most parts of the domain where LES quality metric, γ is greater than 0.8. However, some poor quality cells do exist and they lie within the jet region. Although, only a very few % of cells are present in the region, the inadequacy in capturing turbulence by the current grid resolution may affect the results especially post disintegration. Number of ligaments and droplets forming and the size of these structures may be affected and this has to investigated further by improving grid resolution.

The model used in the previous study [3] was constructed with inappropriate grid size for multi-phase liquid jet simulations and was not properly validated. These issues are rectified in the present work and the resulting CFD model validates both the test cases with appreciable accuracy, and is reliable. The issue with the LES quality metric produced by this model is addressed in the next chapter where qualitative analysis of oil jet structures is presented in detail.

4

Oil jet characteristics

In this chapter, structure of oil jets are presented and analyzed extensively for all the tested flow rates, to identify typical characteristics and patterns involved in their evolution. This type of comprehensive investigation on oil jets is not easily available in technical literature. Each jet is dissected into different zones based on their appearance, and dominant forces observed in their development are identified. Such an interpretation aids in describing jet structures, the disintegration process and also provides better understanding of the physics involved, which was unclear from the results of previous study [3]. It is important to obtain this knowledge because, from an engineering standpoint, it will be possible to estimate typical behaviour of oil at a given flow rate and predict its impact on both types of cooling processes. Also, the inferences can be generalized to any liquid jet that falls under these regimes. Qualitative results are compared to the physics described in literature, and effects of turbulence at jet exit on spreading behavior are also discussed. This aids in explaining the observed flow rate efficiencies in Fig. 3.19.

The chapter begins with a short description of typical characteristics identified across all flow rates in section 4.1. Simultaneous comparison of the jets provides a simple way for establishing similarities and differences, with which jets are broadly classified into: laminar, transitioning and turbulent regimes in section 4.2. These are followed by presentation of droplet sizes in 4.3 which are also not available in literature for oil and/or for piston cooling. Quantifying them is one of the primary objectives of this research work. During these analyses, some discrepancies are noted in both qualitative and quantitative results, and these are summarized in section 4.4 including the LES quality observations made in the previous chapter. With this, a need for grid refinement is assessed and a strategy is developed in section 4.5, where a small-periodic model is built and the effect of grid resolution on the inconsistencies are verified.

4.1. Typical characteristics

In general, when a jet is injected into an atmosphere from a nozzle, it is exposed to sudden change in boundary (from wall to free-stream) at the nozzle exit, which serves as a main source for disturbing the flow. These disturbances feed-off of the energy contained in the flow and grow in amplitude especially when the flow becomes turbulent within the nozzle itself. For a liquid jet coming out of a circular nozzle, disturbances arise along the circumference and develop to reach the jet axis, at which point disintegration (primary breakup) begins (Plateau-Rayleigh instability). This leads to ligaments and droplet formation, and spreading. Such a type of flow development is used as basis for describing oil jet evolution here and in the upcoming sections.

Iso-surfaces with liquid volume fraction above 0.99 are used to visualize the jet similar to section 3.3.3. Comparison of different iso-surfaces is done and a sample is shown in Fig. 4.1 for the jet at 7 L/min. Some differences can be observed along the interface boundary due to the turbulent nature of the jet, and the

appearance of few ligaments and droplets are affected at downstream locations, using the 0.99 threshold. However, as mentioned in section 3.3.3, to identify the liquid core primary breakup, it is important to visualize the cells that are completely filled with oil for which iso-surface with 0.99 is sufficient. At lower flow rates, the variation is even smaller (as in Fig. 3.13) and hence, the differences are neglected. These iso-surfaces are used purely for qualitative purposes and quantitative results presented in later sections remain unaffected.

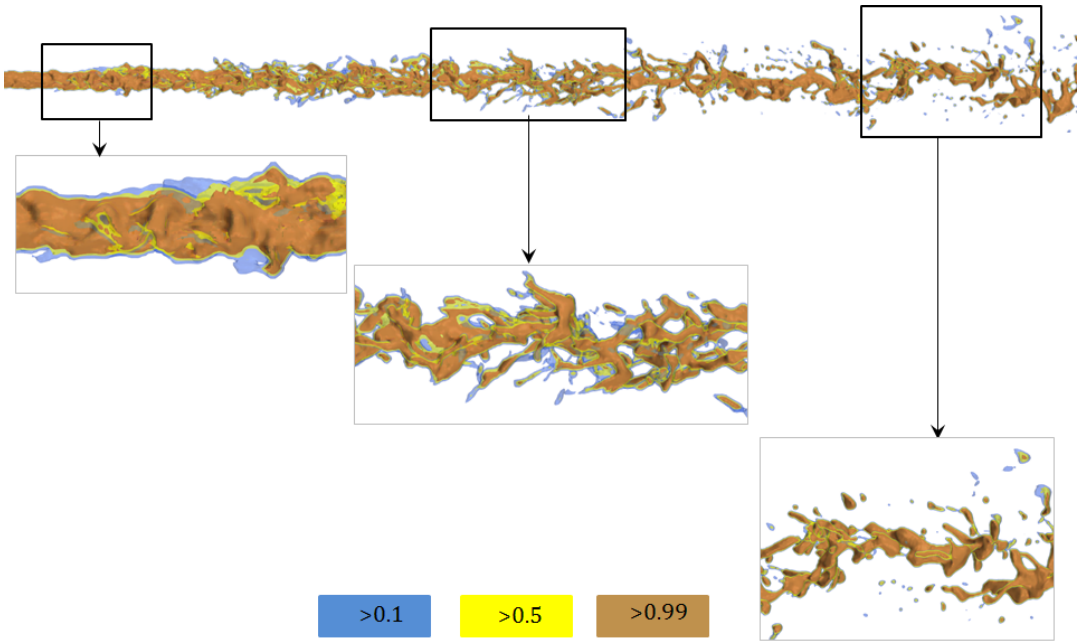

Figure 4.1: Iso-surface for oil jet at 7 L/min (turbulent)

Jets obtained for five different oil flow rates are displayed in Fig. 4.2. BDC and TDC positions of the piston are marked for reference. Although, only instantaneous snapshots of the jets are presented, the figure contains typical characteristics that can be observed at corresponding flow rates. The first observation is the enhancement of disruptive forces and chaotic behavior in the jet structure with increase in flow rate. There is a clear transition to turbulence from 3 L/min to 7 L/min which leads to disintegration. The onset of primary breakup moves closer to the nozzle at higher flow rates which is consistent with literature from section 2.1.3.

At 3 L/min, the jet corresponds to laminar condition. It is fully intact and does not disintegrate even post TDC. The jet at 7 L/min is fully turbulent for which breakup occurs even before reaching BDC, and further evolution is of the form of ligaments and droplets. As a result, spreading increases and lesser amount of oil enters the cooling gallery orifice at TDC which is the cause of reduced flow rate efficiency, observed in Fig. 3.19. Jets at intermediate flow rates (in transition) display intermittent breakup at the vicinity of TDC. However, no significant difference in typical characteristics can be identified. Wavy nature and protruding, elongated ligament structures are the consistent characteristics that can be observed for all three cases. With increase in flow rate surface breakup increases, where the droplets are stripped off at the interface. The jet at 6 L/min is comparable to both 5 L/min and 7 L/min cases. Elongated ligament structures are present in the upper half similar to the jet at 5 L/min, and surface breakup and increased turbulence levels near the nozzle exit resemble the jet at 7 L/min.

These results are different from those of Celik, especially for 5 L/min and 7 L/min, where the latter doesn't observe the undulating nature and protruding elongated ligaments for 5 L/min and increased disintegration for 7 L/min. This difference is purely attributed to the improved grid resolution that allows for better capturing of these characteristics. Simultaneous inspection of these jets show a pattern that can be observed in the structure. This can be described by dividing a jet into four different zones: undisturbed jet, sinuous wave zone, pre-breakup and post-breakup zones.

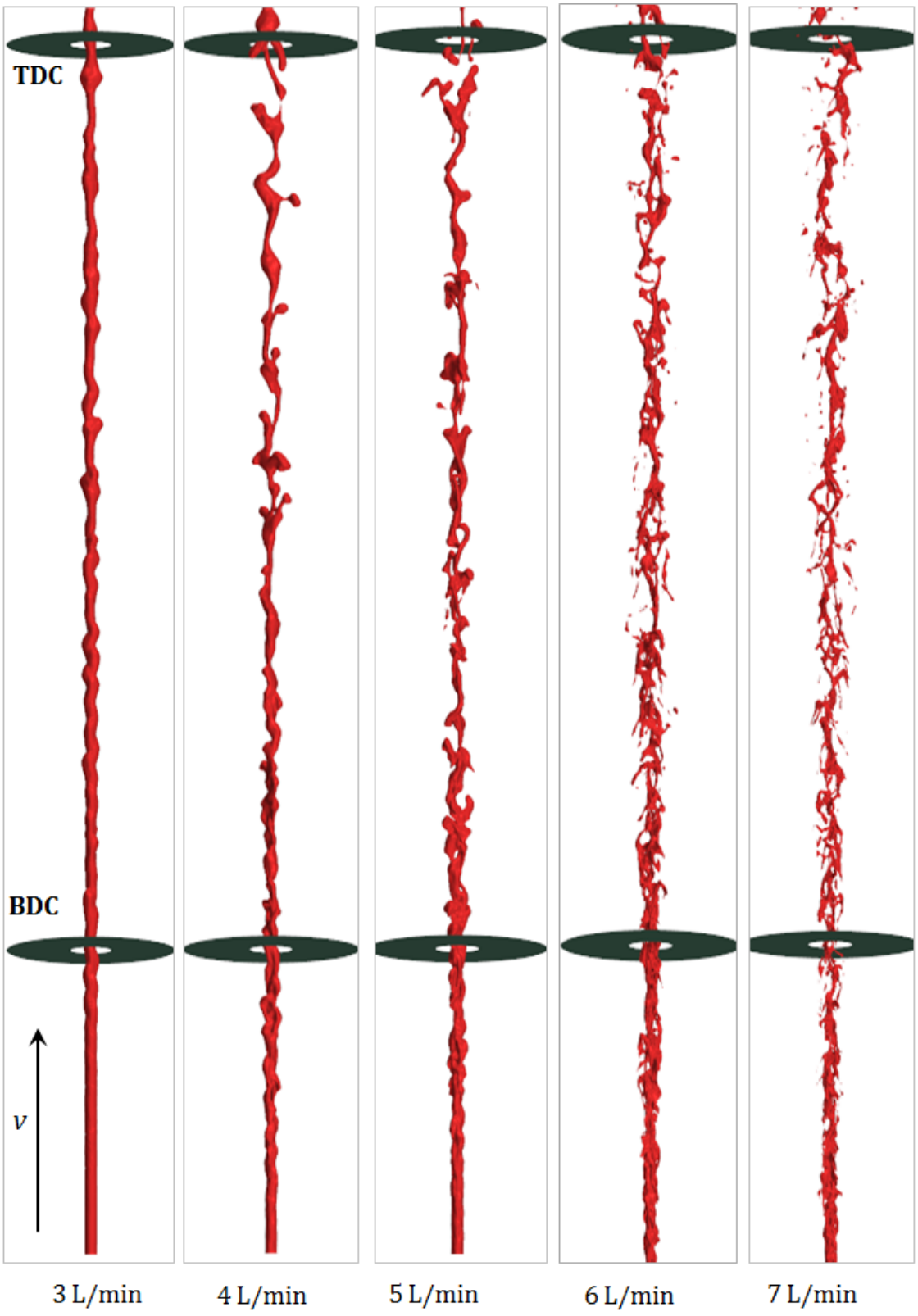

Figure 4.2: Jet structure for all the tested flow rates

Depending on the flow rate, a jet goes through at least one of the four zones while travelling from BDC to TDC. This is elaborated in the following section.

4.2. Evolution pattern

In this section, the four zones are described using qualitative LES results. With this, the flow rate efficiency obtained for gallery cooling and droplet size results for spray cooling can be interpreted convincingly. This will also be helpful in providing an idea of how effective cooling will be with a typical piston cooling jet at different locations from BDC to TDC. Quantitative analysis of these zones are beyond the scope of this project.

Typically, liquid jets are classified and analyzed based on the regimes mentioned in section 2.1.3. However, due to the consistency in characteristics observed at intermediate flow rates, presentation and interpretation of results are done by categorizing the jets as: laminar, transitioning and turbulent.

4.2.1. Laminar Jet

The jet at 3 L/min is low speed and corresponds to laminar flow conditions at the nozzle exit. Fig. 4.3 depicts the jet structure and corresponding zones. At this flow rate, the jet remains completely intact. Near the nozzle exit the jet appears to be steady and the disturbances gradually develop on the jet surface to form a wavy pattern.

In Fig. 4.3, **undisturbed jet** corresponds to the steady region where no perturbations are visible along the surface. Amplitude of disturbance imposed on the jet has not grown enough to produce surface waves, and finally induce breakup. In this zone, liquid column is axisymmetric. The jet neither has enough energy to enhance the disturbance sufficiently, nor does it have enough cohesive forces to damp the perturbations and retain its undisturbed nature. Towards the end of this zone, perturbations gradually develop and they disturb the columnar structure of the jet.

This is followed by introduction of waves, similar to those observed in Fig. 2.2 for FWI regime. These waves are present throughout the remaining portion of the jet giving rise to the **sinuous waves** zone where the jet axis oscillates about the nozzle axis with minimal amplitude. Similar observation is also made during turbulent water jet validation and the jet resembles a twisted rope structure. Axisymmetric property of liquid column is killed as the jet proceeds further. Since the jet does not have sufficient energy to develop the waves and induce breakup, it remains intact even after reaching TDC, as displayed in Fig. 4.2. Breakup length correlations of Grant and Middleman estimate L_c/d = 130.7 for this case, and the distance travelled by oil from nozzle to TDC is only L/d = 76.66, which supports the observation of absence of primary breakup. Near TDC, amplitude of the waves may let the jet exceed the gallery orifice radius at very few instances. This means that during flow rate efficiency sampling, a few samples may show zero oil flow leading to efficiency just less than 100 %. Apart from grid resolution, this can also be the cause for 1 % difference in efficiency between LES and DAF experiment. Similar results are also obtained by Celik [3].

4.2.2. Transitioning jets

Table 3.6 indicates that jets at flow rates 4 L/min, 5 L/min, and 6 L/min fall under laminar-to-turbulent transition regime. These are integral to piston cooling application and no data is available in literature for such jets. Present study stands out from the rest in this regard as these jets are analyzed in detail. At each flow rate, three zones are identified: undisturbed jet, sinuous waves and pre-breakup. Following paragraphs elaborate the description of these zones.

For all three cases, structures of the jet immediately after nozzle exit represents undisturbed jet zone. Nature of this zone is same as the description provided for 3 L/min. A major difference is the reduction in length of the zone with increase in flow rate. This can be seen in the Fig. 4.4 especially at 6 L/min, where disturbances grow faster leading into the sinuous waves zone due to increased disruptive forces. Also, at this flow rate, the distinction between the zones has diminished.

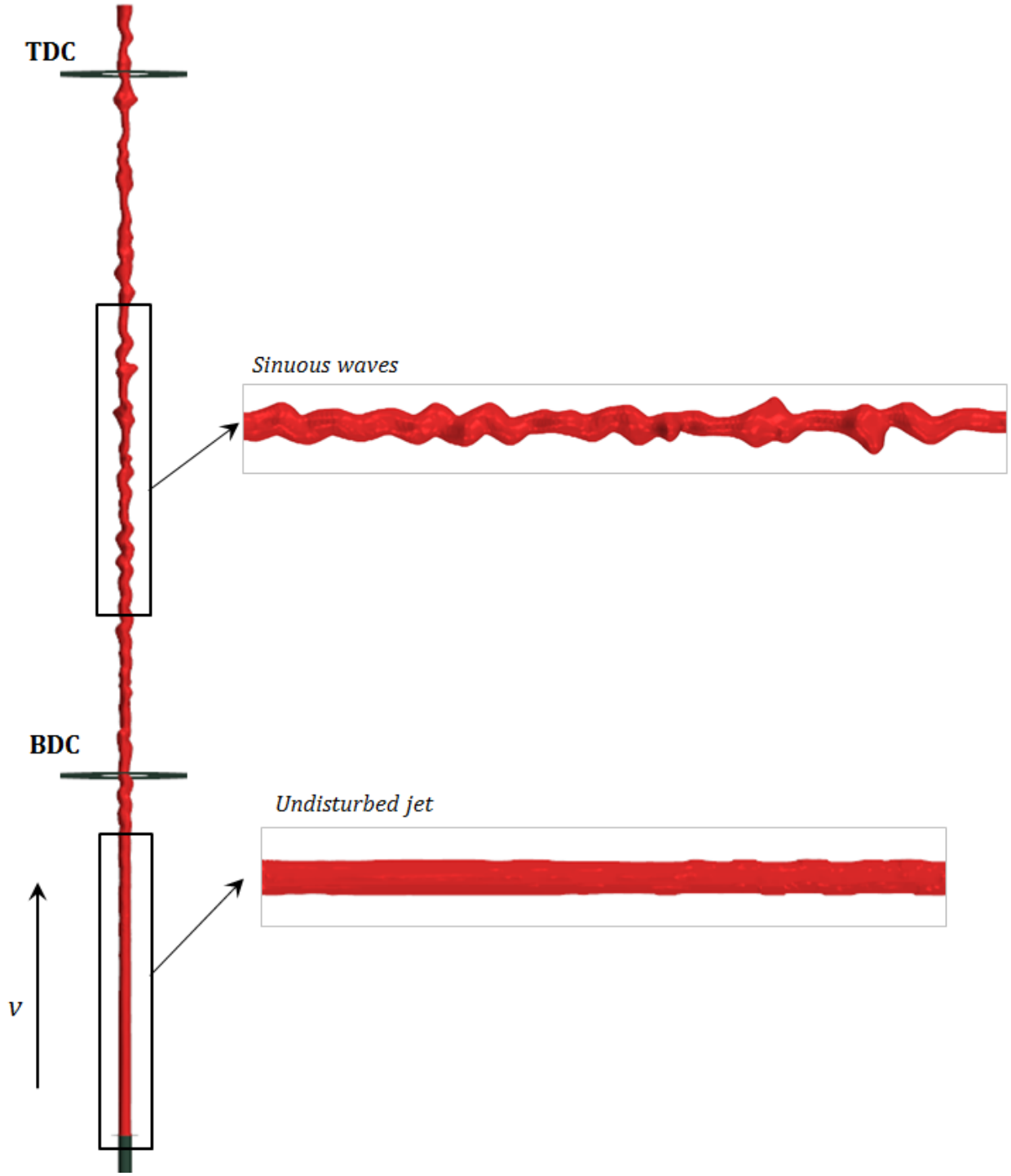

Figure 4.3: Jet structure at 3 L/min. Two zones are observed and highlighted

In the sinuous waves zone, apart from the presence of surface waves, their point of occurrence, wavelengths and amplitudes are different for all three cases. Wave occurrence begins closer to nozzle exit, wavelengths become shorter, and amplitudes are higher, especially at 6 L/min. Axisymmetric properties are lost and jets enter into the pre-breakup zone where disturbances grow further and reach the jet axis. The jet does not break completely, and the vertical columnar structure is destroyed producing ligament protrusions, and yielding a wavy or oscillating jet, as shown in Fig.4.5. Full detachment from the liquid core does not occur in this zone and the ligaments remain connected with an elongated shape. The jet axis fluctuates severely

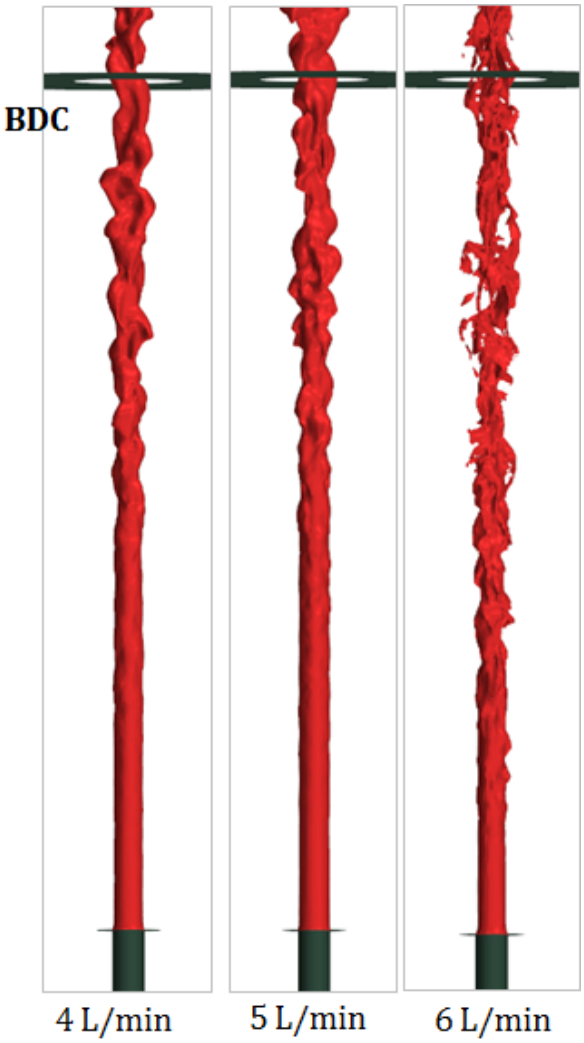

Figure 4.4: Undisturbed and sinuous wave zones for all flow rates corresponding to the transition regime

about the nozzle axis. Very few structures may pinch-off from the jet due to Rayleigh breakup, as indicated in Fig.4.5 for 4 L/min and 5 L/min, and this process is uncertain as pinching may be absent at the next instant. Surface strip-off of ligaments/droplets is enhanced and happens actively at 6 L/min. However, the core remains attached with the help of elongated structures and spreads enroute to TDC. Very close to TDC, complete detachment of the liquid core (primary breakup) can be observed for all three cases. But, this does not produce significantly smaller structures especially in the case of 4 L/min and 5 L/min, and hence, the jet does not enter into the post-breakup zone. Ligaments that form after primary breakup are bigger and have sizes of the order of nozzle diameter (d).

Characteristics such as protruding ligaments, oscillating jet structure, absence of breakup until TDC, and intermittent pinch-off can be due to the transitioning nature of these jets. All of these with enhanced spreading affects the amount of oil entering the cooling gallery resulting in reduction of flow rate efficiency as seen in Fig. 3.19.

4.2.3. Turbulent Jet

Jet at 7 L/min exits the nozzle in a fully turbulent state. This means that the disruptive forces are significantly higher and the disturbances can grow faster leading to an earlier primary breakup as indicated by

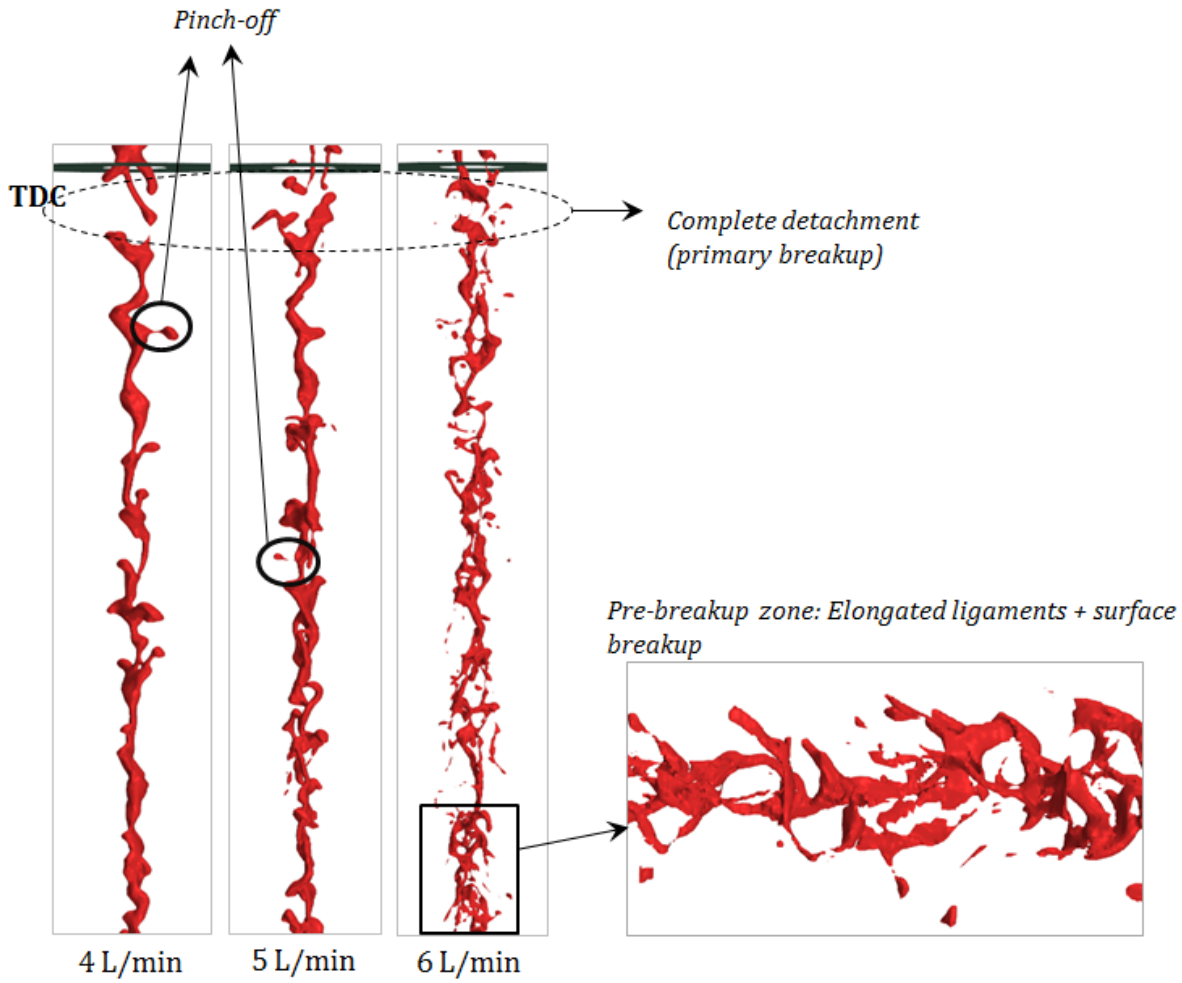

Figure 4.5: Pre-breakup zone for all transitioning jets

Fig. 4.6. The structure of the jet closely resembles jets in SWI regime, presented in Fig. 2.2. Downstream of the nozzle there is a very small portion of undisturbed jet zone which then shifts quickly into sinuous waves without a clear separation between the two zones. Typical to any SWI jet, wavelengths in the sinuous wave zone are shorter [5, 28]. These disturbances develop into the pre-breakup zone, immediately downstream. In pre-breakup, chaotic behavior is observed and ligaments are produced. It is difficult to distinguish the connectivity of ligaments in most parts of this zone and the wavy nature is not noticeably distinct as in previous flow rates. This is due to the turbulence level of the flow.

The three zones occur near the nozzle exit, pulling primary breakup of the liquid core closer, consistent with literature [5, 17, 22, 28]. In Fig. 4.6, location of liquid core disintegration is highlighted. The sudden drop in breakup length when comparing with previous cases may be due to turbulence levels, where breakup remains uncertain till TDC because of the transitioning nature of jets.

Primary breakup occurs mainly in the form of ligaments and very few droplets. After this, there are some typical characteristics to the remaining flow which come under the **post-breakup zone**. In this zone, jet is even more chaotic. Spreading is augmented, as witnessed by Celik [3], and pinch-off happens more frequently. Ligaments break further to form droplets and the number of droplets formed at 7 L/min is more than what was observed at 5 L/min and 6 L/min. Visual inspection shows that droplet sizes are much smaller than jet diameter, as anticipated [5, 6]. Most of the droplets are produced away from the jet axis due to Rayleigh breakup at ligament tips, similar to the observations of Sallam et. al [16, 25]. These droplets move

further away and due to increased dispersion, more spilling happens allowing only lesser oil to enter the cooling gallery. Hence, flow rate efficiency reduces and is the lowest among the tested cases. Such spilling will result in droplets impacting the piston surface which will enable droplet impingement/spray cooling heat transfer.

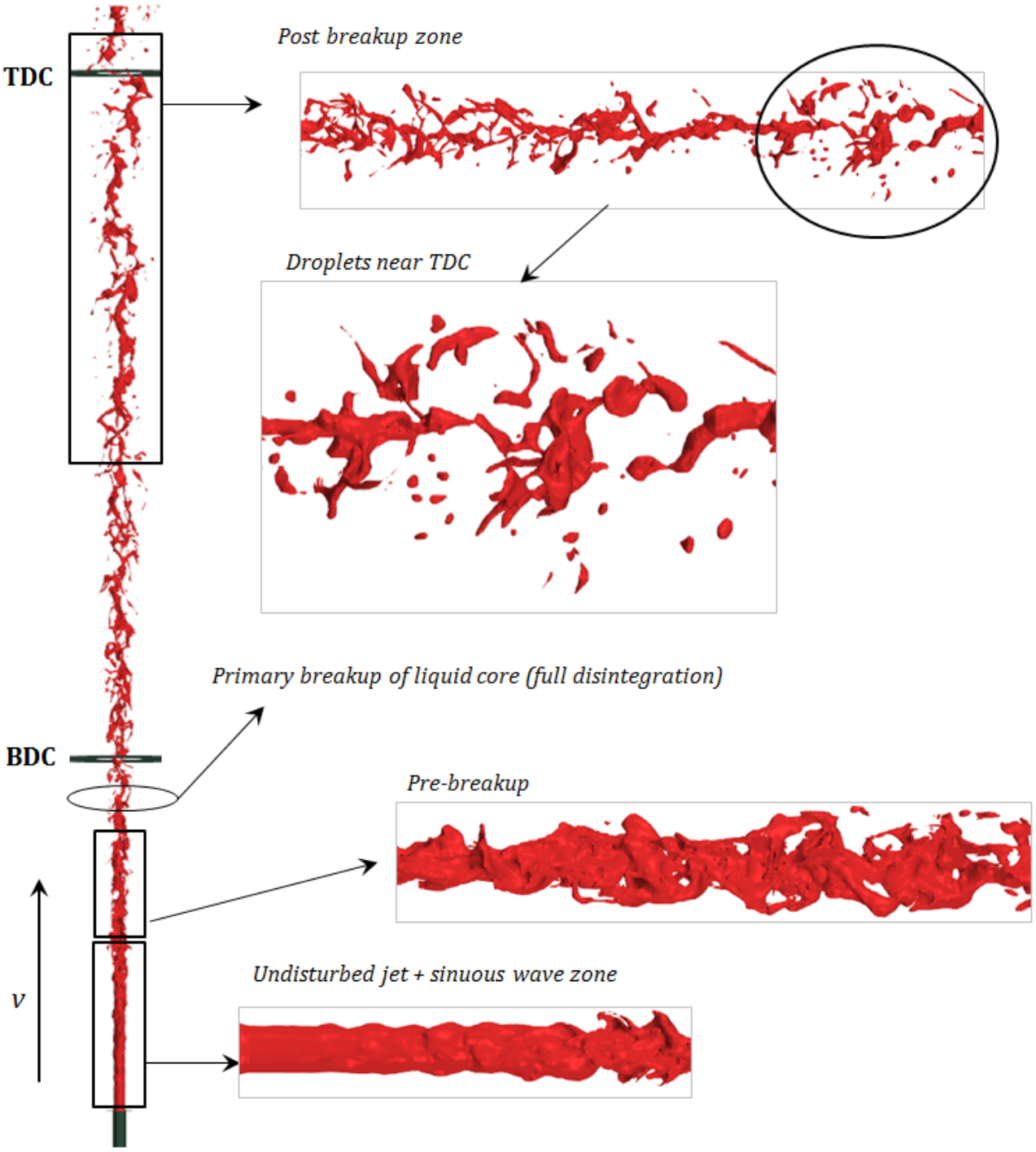

Figure 4.6: Jet structure at 7 L/min.

Fig. 4.6 shows an increased number of ligament structures when compared to the number of smaller droplets. As mentioned in section 2.1.8, typical liquid jet breakup involves very small droplets. The current grid sizes restricts the minimum droplet size that can be captured, and in actual case oil jet at this flow rate

may show increased disintegration. This is discussed further in section 4.4.

4.3. Droplet size results

Droplet size quantification is possible only when the jet disintegrates to form enough number of ligaments and/or droplet structures. Results presented in section 4.2 indicate that the laminar jet does not disintegrate and no liquid structures exist. Jets at 4 L/min and 5 L/min (in the transition regime) break close to TDC. Post breakup, very few ligaments are present and there is insufficient number of samples to obtain a distribution at these flow rates. From Fig. 4.5, jet at 6 L/min shows better droplet count near TDC. Turbulent jet (7 L/min) disintegrates the most and several ligaments and droplets can be seen in Fig. 4.6. Hence, it is possible to compute size distribution for oil jet at 6 L/min only near TDC, and for 7 L/min from BDC to TDC. This is done along the flow direction at five different piston positions for the latter case, indicated in Fig. 4.7. Droplet diameters are quantified using blob detection model which is applied locally in the vicinity of these locations.

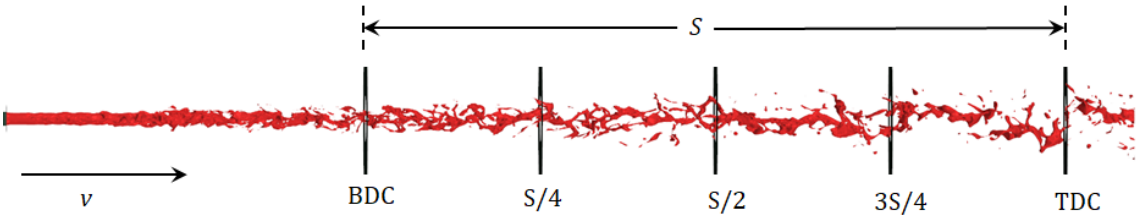

Figure 4.7: Piston positions chosen for droplet size quantification, where S is the stroke length

4.3.1. 6 L/min

Results for 6 L/min at TDC are presented in Fig. 4.8. Alongside, Probability Distribution Function (PDF), Cumulative Distribution Function (CDF) are also plotted, as they are necessary for further studies on impingement/spray cooling of pistons with StarCCM+. This will be addressed, in brief, in the recommendations section at the end of this report.

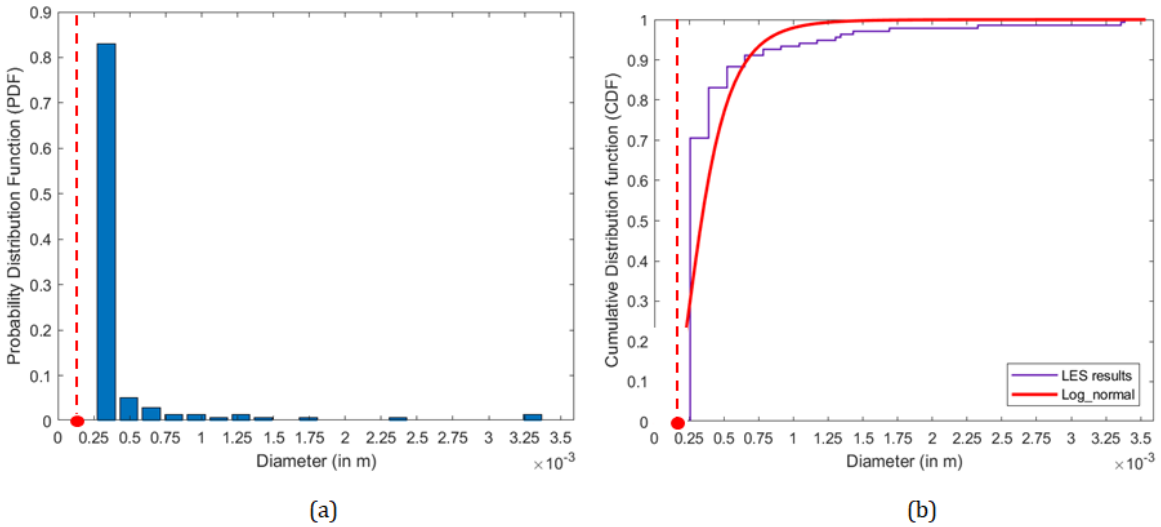

Figure 4.8: Droplet size results for 6 L/min at TDC, (a) PDF and (b) CDF

Fig. 4.8 indicates that the minimum diameter is greater than the current LES grid size indicated by the

dashed red line. This is because, as mentioned in section 2.1.8, the CFD model can capture only grid-resolved liquid droplets which makes the smallest cell size as limiting factor. Smaller droplets cannot be obtained unless grid refinement analysis is performed. Log-normal distribution is found to have the closest match for the obtained results and this is indicated in CDF, Fig. 4.8(b). Table 4.1 shows the mean, minimum and maximum diameters obtained for this case. Accuracies are obtained by determining standard error with 95 % confidence level, similar to (3.3).

	Mean, (x 10^{-3} m)	**Minimum**, (x 10^{-3} m)	**Maximum**, (x 10^{-3} m)
Droplet size at TDC	0.70 (±0.02)	0.25 (±0.03)	2.85 (±0.10)

Table 4.1: Droplet diameter statistics at 6 L/min

4.3.2. 7 L/min

For 7 L/min, results at five different locations are presented through Fig. 4.9 to 4.13. Characteristics observed in the trend of droplet size results at individual locations match with those mentioned previously for 6 L/min. At every location, mean diameter is lesser than that observed for 6 L/min at TDC. This is a result of increased turbulence due to increase in flow rate. Disruptive forces are higher and cause increased disintegration, forming smaller structures. Wu. et. al [14, 24] found maximum droplet sizes in their case to be in the same order of integral length scale of turbulence (or of the nozzle diameter (d)). This is because the large scale eddies are responsible for production of large sized structures in a liquid jet, as mentioned in section 2.1.7. Same observations can be made in the present study as well, as the maximum diameter results are always in the same order of jet diameter (d).

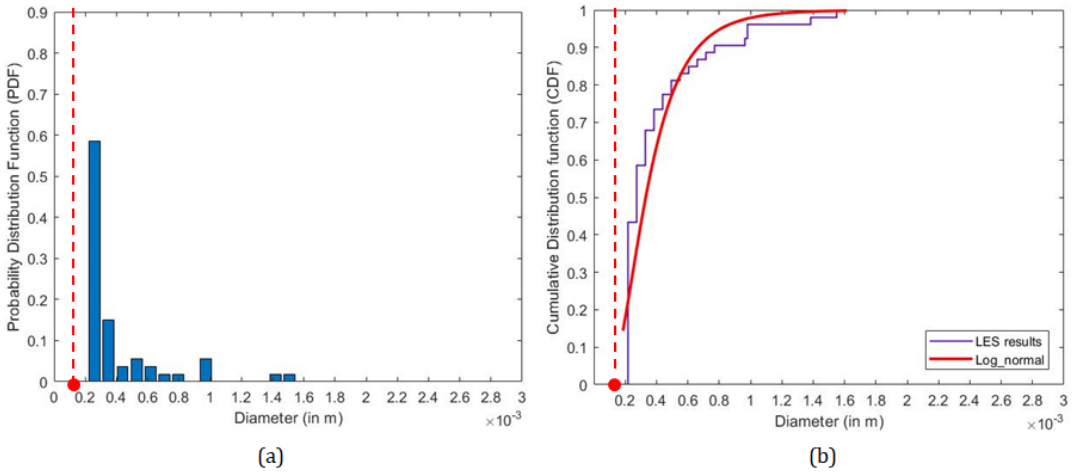

Figure 4.9: Droplet size results for 7 L/min at BDC, (a) PDF and (b) CDF

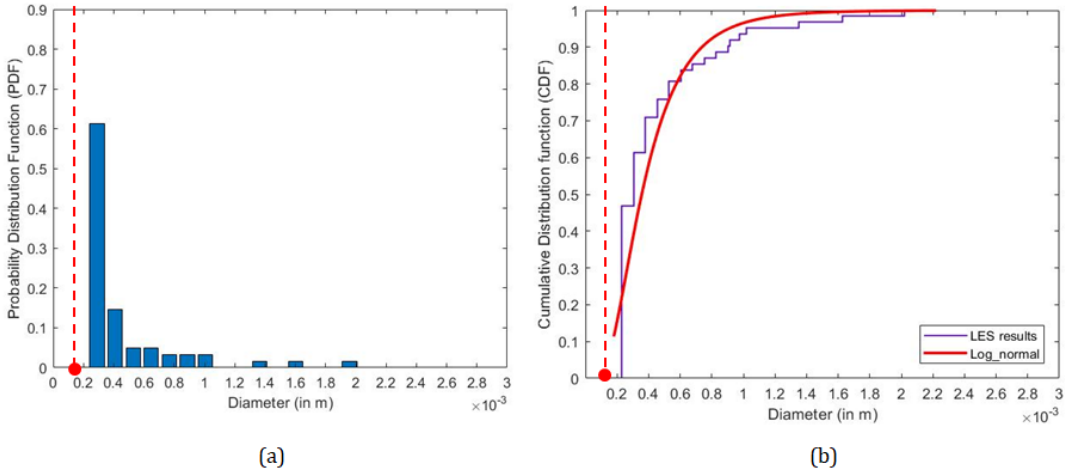

Figure 4.10: Droplet size results for 7 L/min at S/4, (a) PDF and (b) CDF

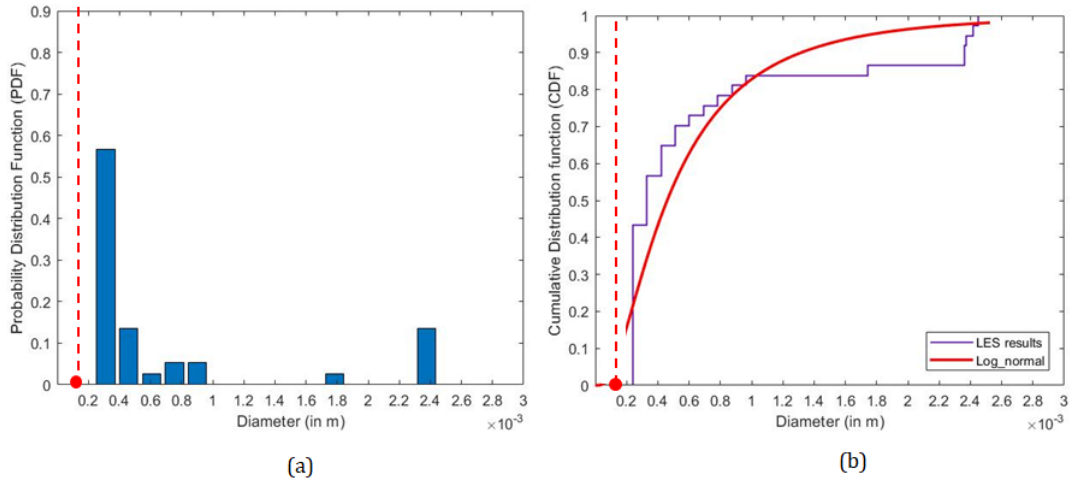

Figure 4.11: Droplet size results for 7 L/min at S/2, (a) PDF and (b) CDF

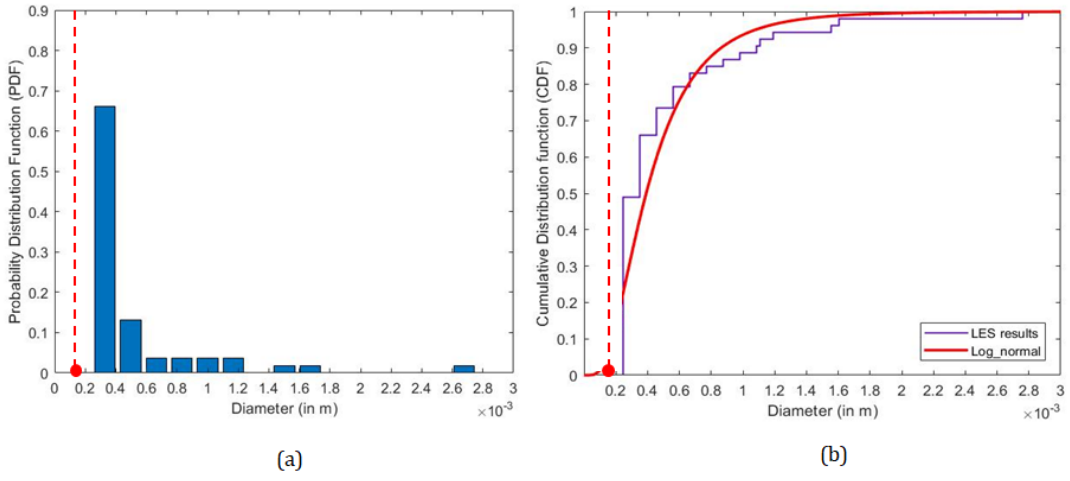

Figure 4.12: Droplet size results for 7 L/min at 3S/4, (a) PDF and (b) CDF

Increase in droplet count can be seen through the increase in PDF values of the minimum sized droplets

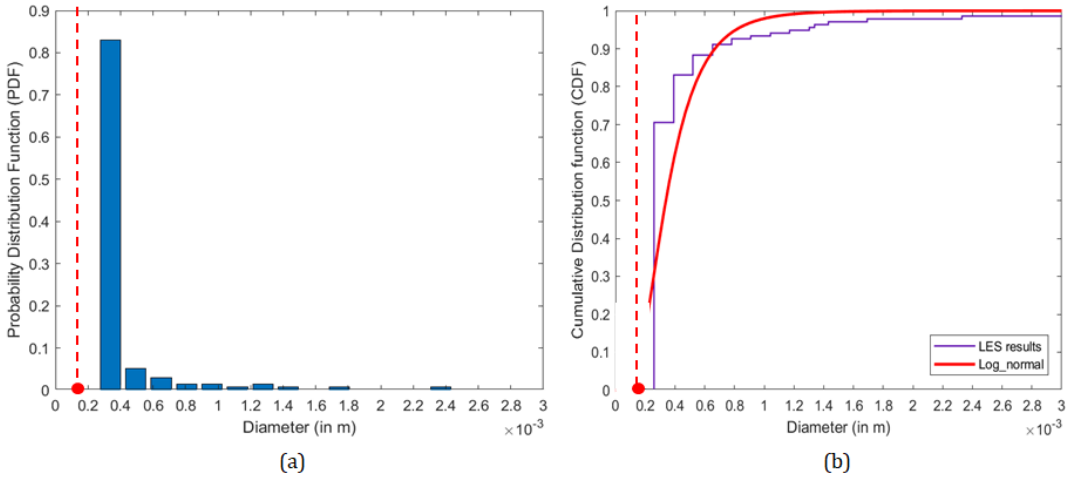

Figure 4.13: Droplet size results for 7 L/min at TDC, (a) PDF and (b) CDF

from BDC to TDC. This indicates an enhancement of secondary breakup along flow direction where ligaments break into smaller structures rising their count. Another important observation is the increasing range of droplet diameters. The minimum size remains around 0.2 x 10^{-3} m while the maximum is increasing from BDC to TDC. This is confirmed by the results quantified in Table 4.2.

Piston position	**Mean**, (x 10^{-3} (m))	**Minimum**, (x 10^{-3} (m))	**Maximum**, (x 10^{-3} (m))
BDC	0.34 (±0.04)	0.22 (±0.02)	1.60 (±0.10)
S/4	0.35 (±0.08)	0.23 (±0.01)	2.00 (±0.20)
S/2	0.47 (±0.08)	0.24 (±0.03)	2.40 (±0.12)
3S/4	0.52 (±0.09)	0.25 (±0.01)	2.45 (±0.15)
TDC	0.60 (±0.09)	0.24 (±0.02)	2.50 (±0.09)

Table 4.2: Droplet diameter statistics at 7 L/min

Both the table, and the figures indicate an increase in droplet size along the flow direction. Mean diameter at TDC is 1.5 times the mean at BDC. Maximum diameter increases from 1.60 at BDC to 2.50 at TDC. Minimum diameter remains approximately the same and varies only by 9%.

Mean and maximum diameter results suggest that the liquid structures are growing in size along the flow direction. Similar observations were made by Wu. et. al [24] and Sallam et. al [16] from their experiments. However, they fail to provide a convincing argument to support their observations. This size increase is a result of droplet coalescence (merging) which could be due to actual flow physics or numerical coalescence because of the restriction posed by current grid size. This is also discussed in section 4.4. Nevertheless, overall structure of the jet and the breakup process indicate that, onwards from this flow rate, spray cooling heat transfer will become almost as significant as gallery cooling.

4.4. Assessment of grid resolution

Mesh size used in the simulation prominently controls its quality and capturing of droplets, as discussed in section 2.1.8. From the qualitative results of jet structures for transitioning and turbulent cases and quantitative results presented in sections 3.18 and 4.3.2 three significant discrepancies related to grid resolution are noted. These do not affect flow rate efficiency quantification as the LES model has sufficient mass balance for both liquid and gas phases. Hence, efficiencies determined to validate DAF experiment (Fig. 3.19) are reliable. The following paragraphs delineate the inconsistencies observed.

- Oil jets in transition are found to lie in SWI regime as per section 2.1.3. For all three intermedaite flow

rates, primary breakup occurs near TDC and does not move closer to the nozzle exit, and this is uncharacteristic to any typical SWI jet. This results in a significant jump in breakup length between 6 L/min, where disintegration occurs closer to TDC, and 7 L/min, where it occurs well before BDC. This can be a physically possible scenario and the discrepancy may be attributed to the transitioning nature of jets at intermediate flow rates. Or, this could be a result of insufficient grid resolution. As mentioned before, the selected grid size may be coarse and this disables the formation of droplets with smaller sizes. Also, the restriction posed by VOF (Fig. 2.5) in capturing the periphery of the droplets may result in merging of two neighboring droplets to form a single elongated ligament structure (numerical droplet coalescence), as illustrated in Fig. 4.14. This could be the cause of an increased number of protruding ligaments, and delayed breakup observed for the transitioning jets.

- For the turbulent jet, post disintegration, Fig. 4.6 shows an increased number of ligaments when compared to the number of droplets. This impacts the droplet count as well as diameter results presented in Table 4.2 and Fig. 4.9 to 4.13, where the mean and maximum diameters increase along the flow direction from BDC to TDC. With grid refinement, the CFD model will be able to capture droplets smaller than those observed in the present case which will rise the droplet count. But the number of ligaments observed may not be the same, since they could be a consequence of actual flow physics at this operating condition or a result of same limitations related to current grid size mentioned in previous paragraph. Presence of numerical droplet coalescence may be the reason for more number of ligaments and for increase in droplet size along the flow direction, as two droplets very close to each other may merge to form one big drop or long ligament.

- With the current mesh, LES quality metric γ results show that a few poor quality cells exist within the jet region, especially at the liquid-gas interface. This indicates insufficient resolution of large scale turbulence in the region of interest. As mentioned in section 2.1.7, liquid phase eddies are responsible for production of ligaments and droplets, and the present inadequacy may affect the disintegration process - both primary breakup and droplet formation. However, Table 3.8, shows a very small % of cells with low quality and thus, the magnitude of impact of this resolution on overall trends may be lower than expected.

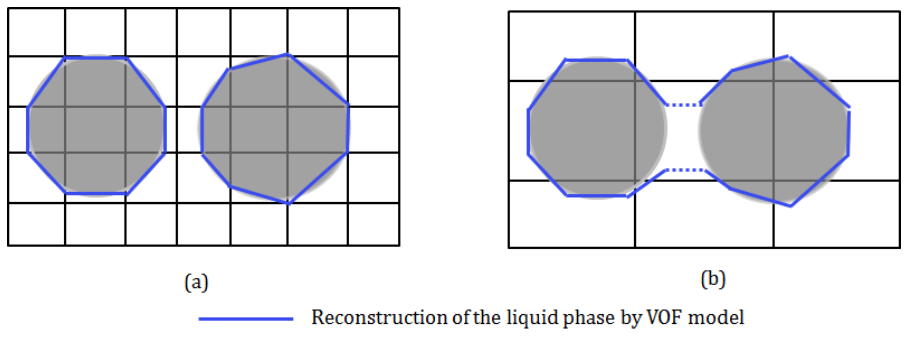

Figure 4.14: (a) Grid required to capture actual droplets and (b) Coarse grid inducing numerical droplet coalescence

All these discrepancies can be addressed only through grid refinement analysis. However, with the present domain, even a small reduction in cell size results in a computationally expensive simulation with total run time exceeding 48 hours. Instead, a small domain with periodic boundary conditions is used to investigate these issues. Similar LES analysis is carried out with this new domain to see the effect of grid on droplet count, droplet sizes, ligament protrusions and LES quality. This model and results obtained are presented in the following sections.

4.5. Small domain analysis

This section is dedicated towards addressing the anomalies observed in oil jet results. For this purpose, a small cylindrical domain with periodic boundary conditions is constructed and a grid refinement analysis is performed with LES. The results help in identifying whether grid resolution or flow physics is the actual cause for the discrepancies observed in section 4.4. First, details about the geometric modifications are presented in section 4.5.1. Grid sizes tested are presented in section 4.5.2. Qualitative and quantitative results obtained are discussed in section 4.5.3

4.5.1. Modified geometry

Fig. 4.15 shows 3D isometric view with boundary conditions and 2D schematic of the geometry constructed for present analyses. A small cylindrical domain is constructed with a length of 4.17 x d (= 1.25 x 10^{-2} m) and diameter of 10 x d (= 3 x 10^{-2} m), where d is the nozzle diameter given in Table. 3.1. The length is selected such that bigger ligaments can be captured, which are of the order $O \sim (10^{-3})$ m. The diameter of the cylindrical cross-section is chosen to be always greater than the spreading distance estimated from the structure of oil jets presented in sections 4.1 and 4.2.

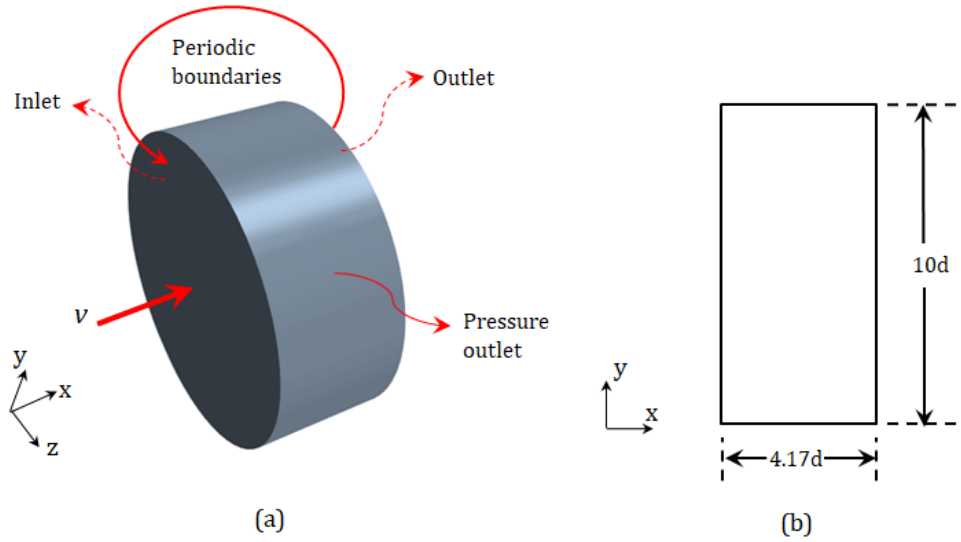

Figure 4.15: (a) Isometric view of the small domain with boundary conditions and (b) 2D schematic of the geometry

Solution from full LES analyses, is mapped onto this new domain, as illustrated in Fig. 4.16. Radial boundary is set as pressure outlet. A periodic interface is created between the outlet along flow direction and the inlet, as shown in Fig. 4.15(a). With this type of boundary, flow within the small domain evolves both temporally and spatially, as the domain resembles a sliding window along the flow direction with increase in time. For initialization, inlet is assigned as velocity inlet, and velocity, volume fraction and turbulence values required at the boundary are obtained from full LES solution. During the simulation, once a solution is observed at the outlet, the control switches to the interface and the solution is mapped periodically onto the inlet, nullifying the specified boundary conditions thereafter.

4.5.2. Grid refinement

Three different grids, one with the same cell size as full LES and other two with smaller sizes are tested. These are chosen based on a similar process to that mentioned in section 3.2.1, satisfying all three criteria of section 2.1.8. With these improved grid resolution, the limiting factor for capturing grid resolved droplet sizes is lowered. Hence, droplets smaller than those obtained from previous analyses are expected in the solution.

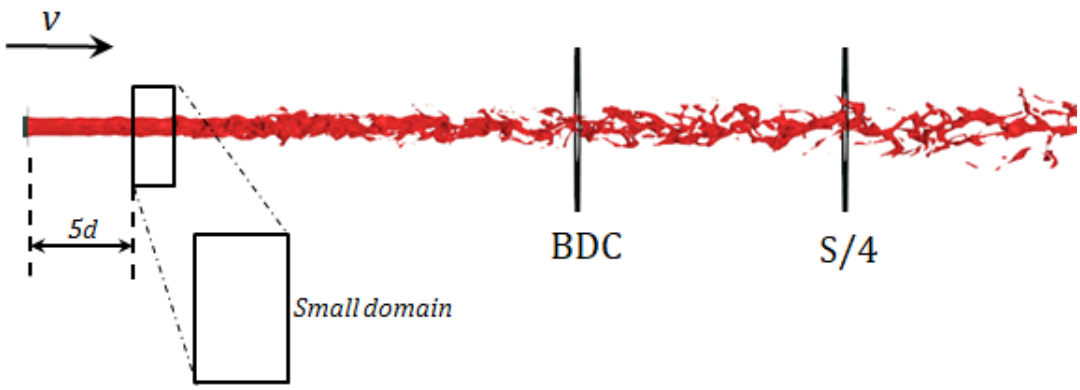

Figure 4.16: Converged results from full LES mapped onto the small domain at a position well ahead of BDC

Table 4.3 contains the mesh settings for each case. It can be seen that the finest grid tested has total cell count lesser than the full LES model. Further refinement beyond Grid-3 is avoided as total cell count exceeds 9.6 Million resulting in increased computational time (>48 hours).

Case	**Grid size in the jet region,** h, (x 10^{-4} (m)	**Total cell count**, (in Millions)
Full LES	1.56	9.6
Small domain analysis		
Grid - 1	1.56	1.1
Grid - 2	0.93	4.4
Grid - 3	0.78	8.8

Table 4.3: Cells size used for meshing the small domain

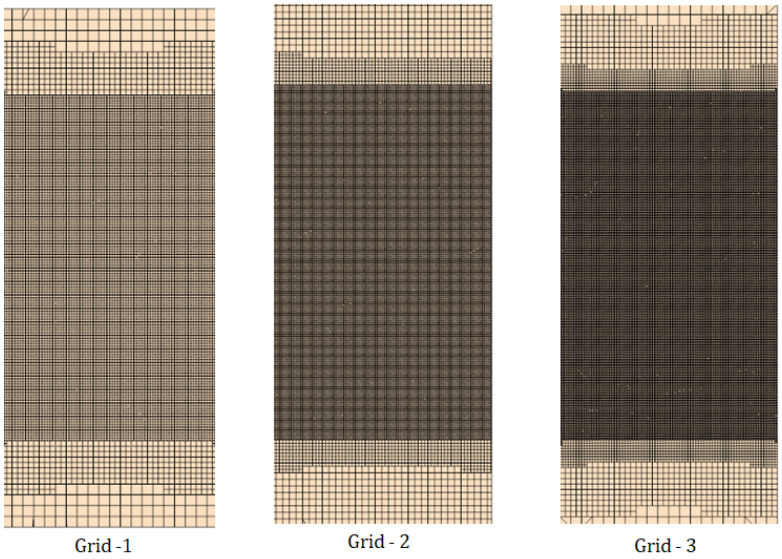

Figure 4.17: Schematic of different meshes constructed for present analyses

In Fig. 4.17, 2D schematic of the three grids are displayed. Width of the refinement zone is 7 x d (= 2.1 x 10-2 m) which is found to be sufficient based on the spreading distance estimated from full LES results. Further increase in the width comes at the cost of increase in computational effort. Time steps are adjusted based on flow rate and values of h, to maintain $CFL < 0.2$. Other simulation settings are kept the same as full LES model.

4.5.3. Results

First, analysis is performed for oil jet at 7 L/min (turbulent jet) with the three grids. Qualitative and quantitative results for that flow rate are presented to outline the effect of grid refinement. This is then extended to other flow rates – 3 L/min (laminar) and 5 L/min (transition), with grids 'Grid-1' and ' Grid-3' alone. Finally, quantitative results of LES quality and droplet sizes are presented.

Turbulent Jet

Structure of the 7 L/min jet at BDC, S/2 and TDC, obtained with the three grids are shown in Fig. 4.18, Fig. 4.19 and Fig. 4.20 respectively.

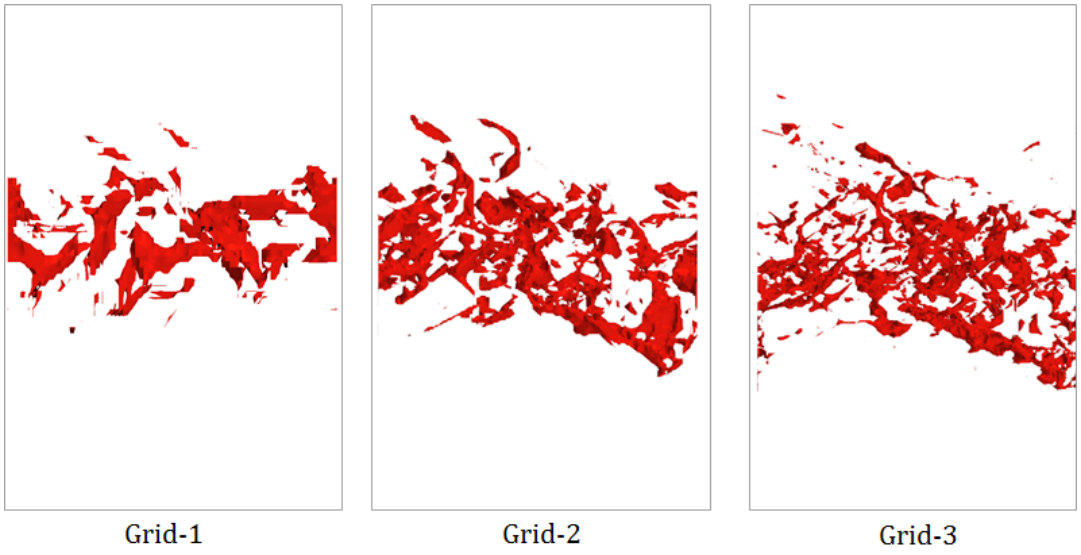

Figure 4.18: Jet structure obtained with the small domain for oil at 7 L/min at BDC

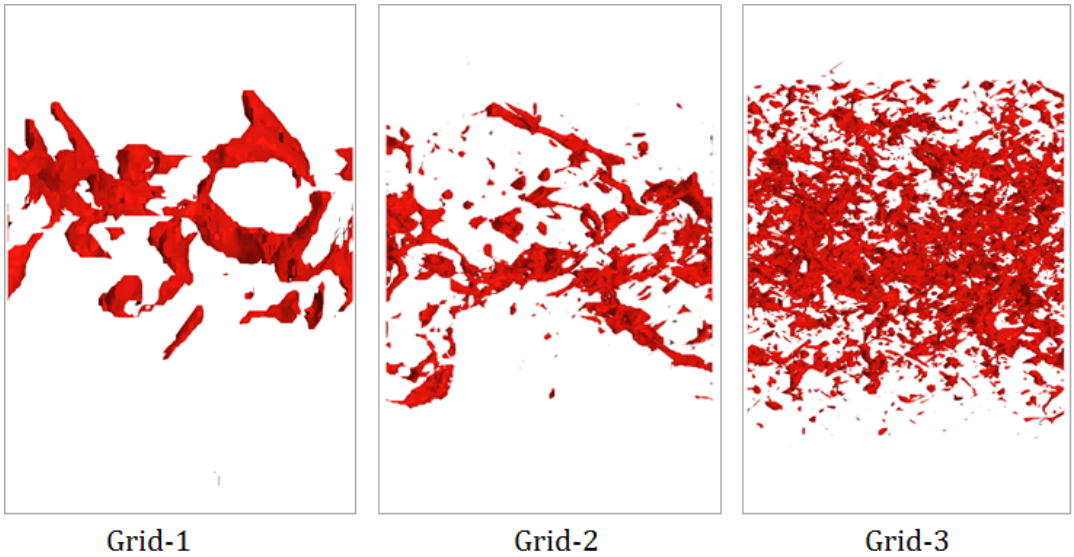

Figure 4.19: Jet structure obtained with the small domain for oil at 7 L/min at S/2

Jet structure obtained for grid-1 conforms with full LES results and qualitatively validates the small domain model. Complete disintegration of liquid core is observed before BDC, followed by ligament and droplet

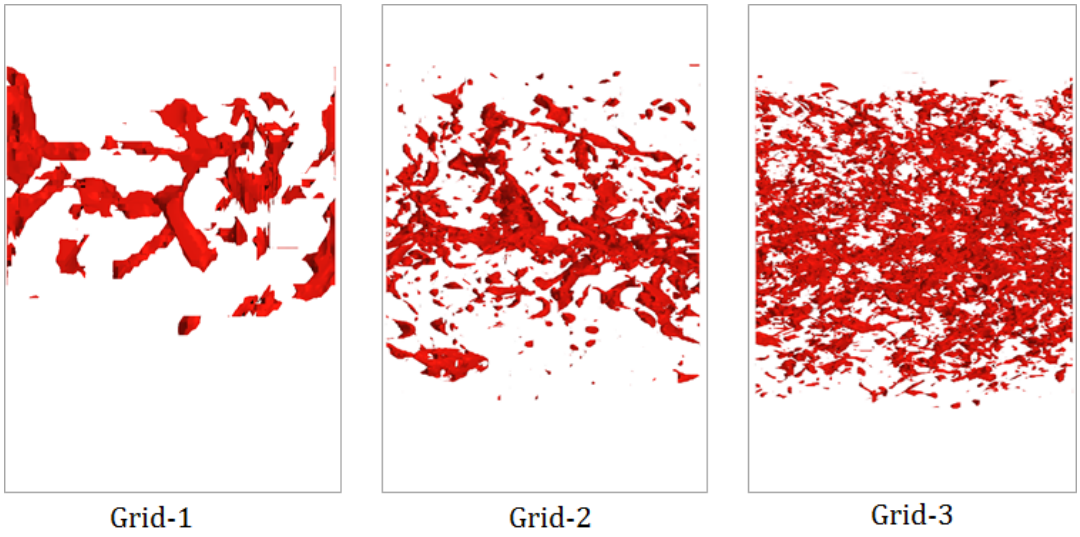

Figure 4.20: Jet structure obtained with the small domain for oil at 7 L/min at TDC

production till TDC. Disintegration increases with mesh refinement near BDC as ligaments and droplets in Grid - 3 are much smaller than those resolved by Grid - 1. Similar observations can be made at other piston positions as well. With the full LES model, increased number of ligaments were observed when compared to the number of droplets affecting droplet count and diameter results. Jet structures obtained with grid refinement show significant increase in droplet count. Ligaments break down to smaller structures and this can be visually identified from Fig. 4.20. As expected in section 4.5.2, fine grids are able to capture smaller droplets as refinement allows cells to numerically resolve structures of these sizes [41].

Apart from these observations, figures also indicate a minor increase in local spreading at corresponding locations, with mesh refinement. This is due to the increased dispersion of smaller droplets which are absent with coarser grid. For the fine grid, Fig. 4.19 and 4.20 show that as the jet evolves post primary breakup, ligaments disintegrate further to form a very high number of droplets near S/2 and TDC locations. This means that the turbulent jet disintegration process is very close to spray atomization. This is consistent with literature because the jet lies in the higher end of SWI regime approaching atomization, as shown in Fig. 3.16. With further increase in inlet flow rate at the nozzle, the jet will enter full atomization regime. This increase in spreading may affect the gallery cooling by inducing a small bu finite reduction in flow rate efficiency. Such lack of spreading with Grid-1 may be the reason for the observed over estimation of η at 7 L/min by the full LES model, during validation of test case - 2 (section 3.4.3). The spreading coupled with increase in droplet count will enhance spray cooling heat transfer of pistons and the quantitative impacts are discussed in the following sections.

Laminar jet

Small domain analysis is extended to laminar jet (3 L/min) with the coarsest and finest grids (Grid- 1 and Grid -3). Jet structure obtained with the grids are shown in Fig. 4.21 and 4.22. Apart from minor differences that exists due to the instantaneous nature of the snapshots, no significant modification can be observed in the overall structure of the jet.

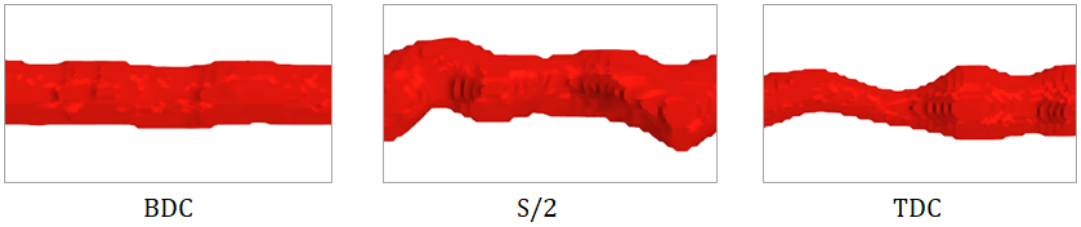

Figure 4.21: Jet structure obtained with the small domain for oil at 3 L/min with Grid - 1

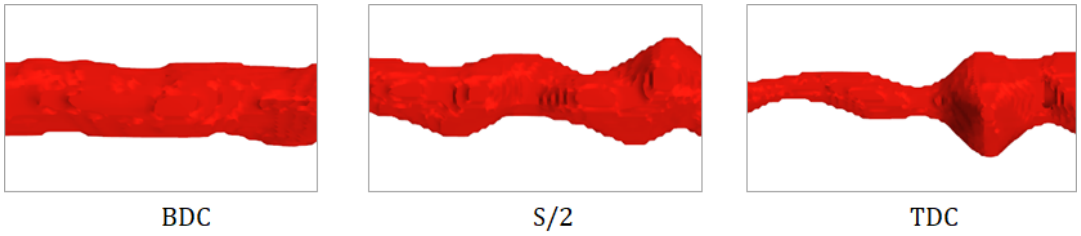

Figure 4.22: Jet structure obtained with the small domain for oil at 3 L/min with Grid - 3

The jet does not show signs of disintegration due to the same reasons mentioned for the laminar case in section 4.2.1. No discrepancies were observed at this flow rate during full LES and both analysis show consistent results. Hence, grid refinement has no effect on laminar jet.

Transitioning jets

Only the case at 5 L/min is considered to study the effect of mesh on transitioning jets. Similar to the laminar case, Grids -1 and 3 are tested. At this flow rate, main discrepancies observed using full LES analysis are the hesitating tendency of the jet to undergo primary breakup and presence of elongated protruding ligaments. Jet obtained with the small domain are shown in Fig. 4.23 and 4.24.

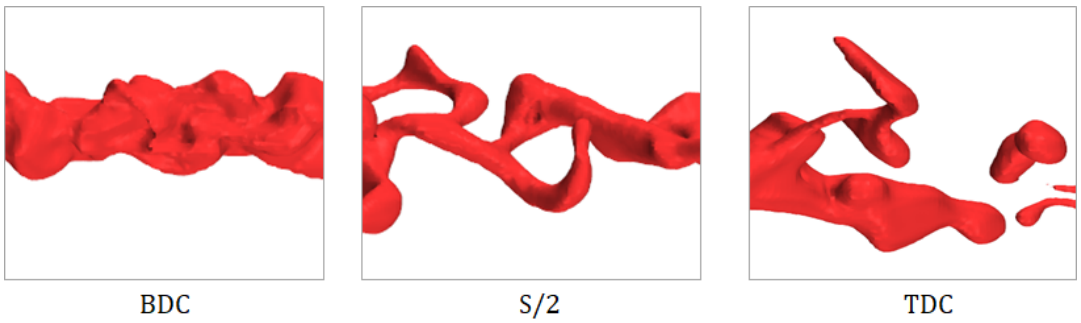

Figure 4.23: Jet structure obtained with the small domain for oil at 5 L/min with Grid - 1

From the figures, grid refinement appears to have no effect on the overall structure of the jet. Moving downstream from BDC, protruding ligaments are still present with finer grid, and refinement has little effect

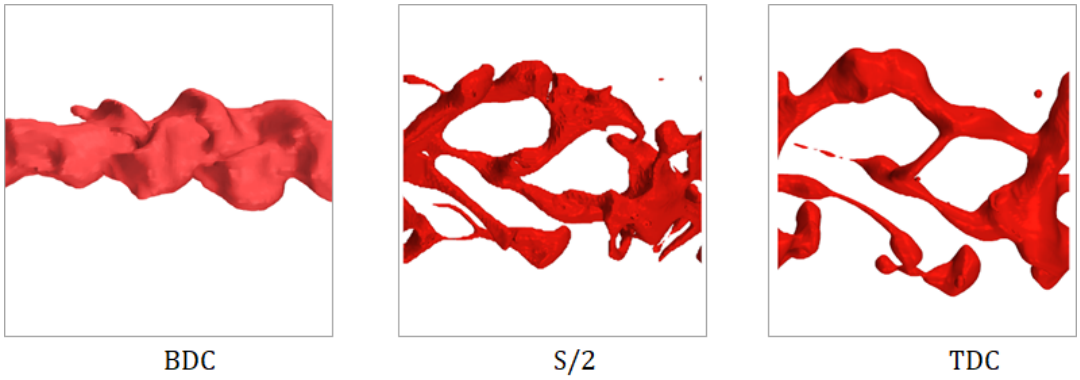

Figure 4.24: Jet structure obtained with the small domain for oil at 5 L/min with Grid - 3

on primary breakup. Surface breakup and droplet pinch-off is more at S/2 but the margin of increase is not enough to quantify droplet diameters and to distinguish the jets in terms of grid size impact. Also, it is difficult to attribute these minor differences to grid refinement purely based on instantaneous snapshots. Hence, for the transitioning jets, it is the flow physics that is responsible for the results obtained with the full LES model.

LES Quality metric

LES quality metric is quantified within the jet region to identify cells with poor quality similar to section 3.4.2. Results for oil jet at 7 L/min are presented in Fig.4.25 for the three tested grids. Similar results are observed at other flow rates and hence, are not presented. Variation in percentage of cells with $\gamma < 0.8$ is plotted along the flow direction, as the domain moves from BDC to TDC with time.

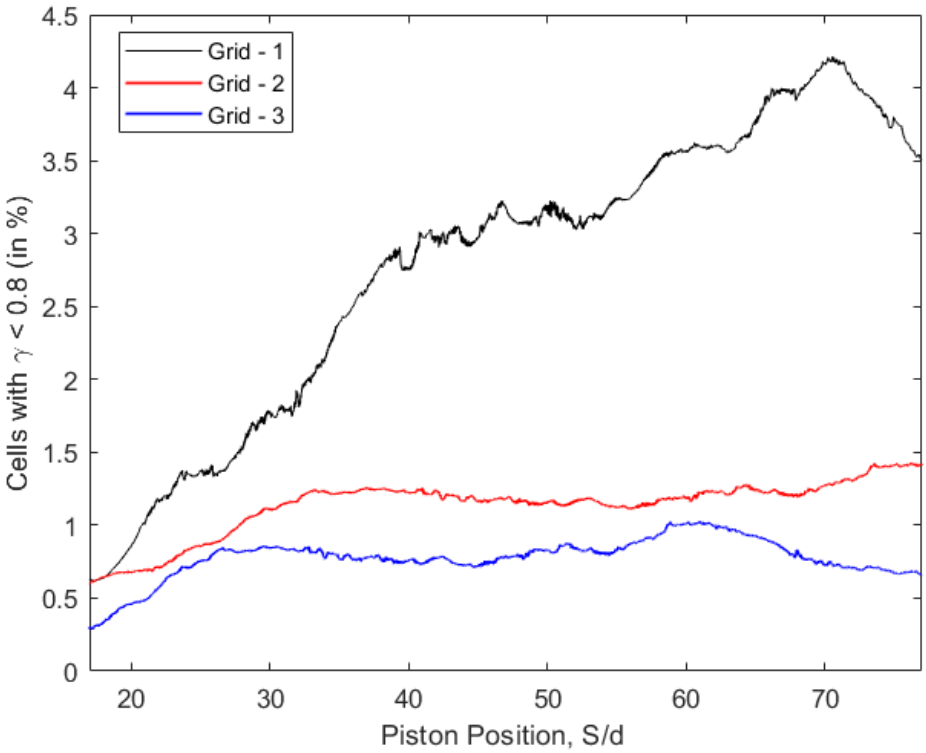

Figure 4.25: % of cells with poor LES quality for jet at 7 L/min, for the three grids

The quality improves with grid refinement: fewer cells are present below the limit for Grid – 3 as the value is always less than 1 %. Even for Grid - 1, although there are more number of low quality cells when compared to other grids, the maximum remains within 4.5%. Fig. 4.25 shows that, for the same grid the number of cells with $\gamma < 0.8$ increases along the flow direction from BDC to TDC due to increased disintegration and spreading. For Grid - 2 and Grid - 3, although there is a slight increase near BDC, variation post this is very less and the percentage of cells remain roughly the same. This indicates that Grid - 1 is not as sufficient as the finer grids in terms of resolving large scale turbulent eddies that form when there is chaotic behavior, disintegration and spreading within the jet region.

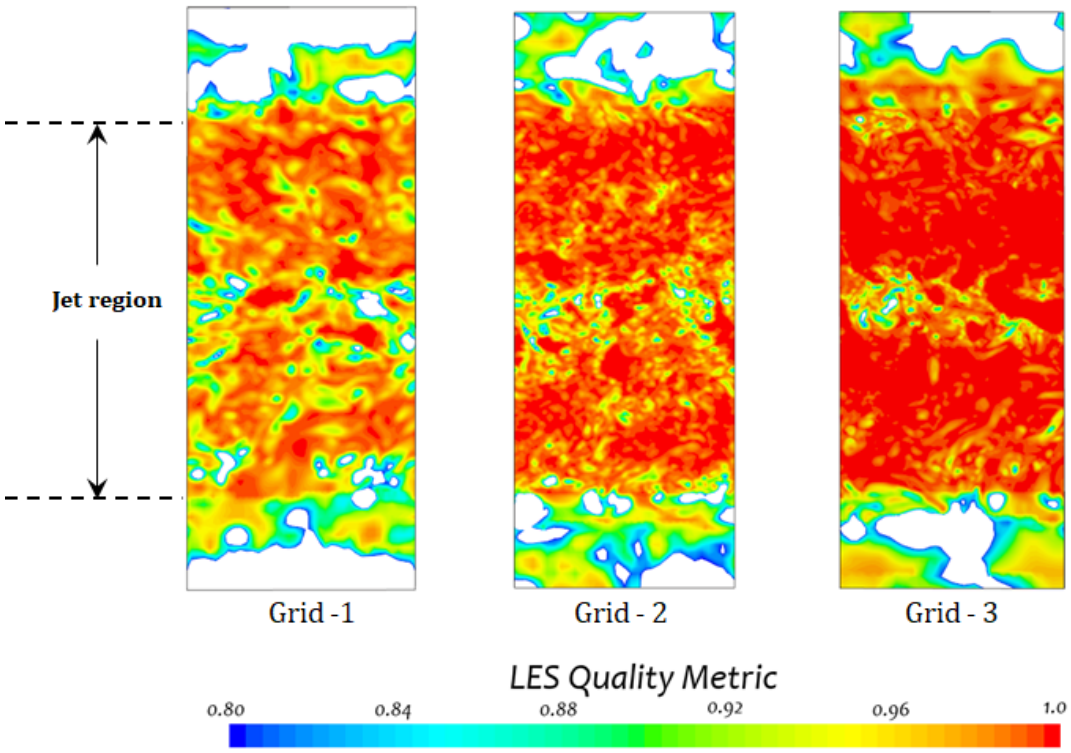

Figure 4.26: Instantaneous LES quality metric results

Fig. 4.26 shows an instantaneous sample, where quality is compared for the three grids on a mid-plane to visualize the location of these poor quality cells in the jet region, where the domain is at the vicinity of TDC. Within the jet region, some cells below $\gamma = 0.8$ can be seen and this reduces with grid refinement. For Grid - 3, it is difficult to locate these cells. With further refinement it is possible remove all the poor quality cells but the present refinement is considered to be sufficient for this study. Hence, the analysis is continued with these grid settings.

Droplet size results

Results presented in 4.3 show that significant number of ligament/droplet structures are present only in the 7 L/min jet. Since periodic boundaries are used, the domain also moves along the flow direction with time and it is not possible to obtain a sampled size distribution at fixed piston positions as done in section 4.3.2. Instead, it is possible to monitor diameter variation as a function of time (or along the flow direction), as in Fig. 4.27. The figure clearly indicates an increase in droplet size with time especially for Grid-1. This trend is also observed with full LES and is one of the main discrepancies for the turbulent jet. With grid refinement, mean diameter shifts to a much lower value due to the presence of smaller droplets as witnessed in Fig. 4.20. Also, there is a reduction to the magnitude of increase in size along the flow direction (Table 4.4). These values are obtained from instantaneous size distributions and accuracies are determined similar to (3.3) by computing standard deviation.

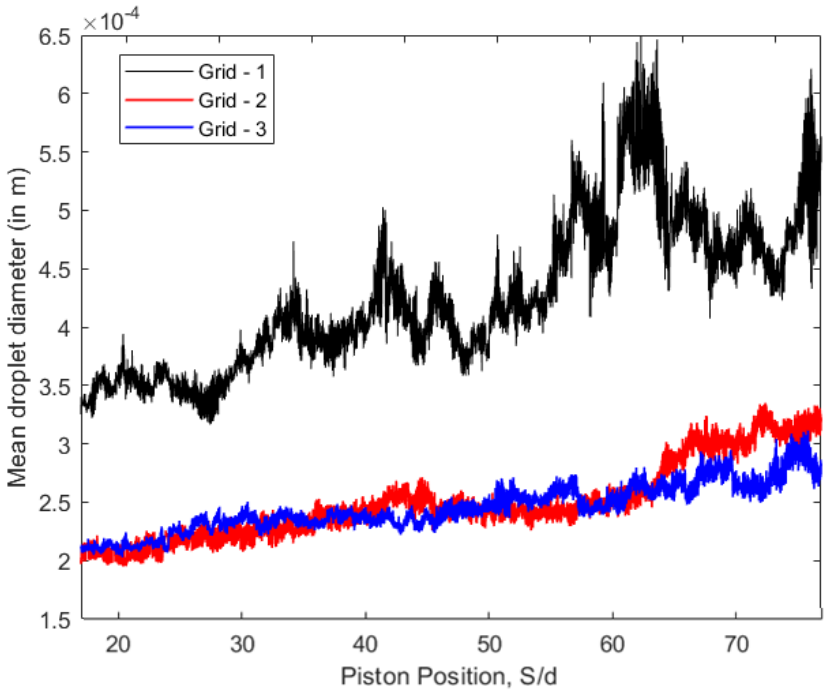

Figure 4.27: Mean droplet diameter variation for the three grids

Results given in the table confirm the decrease in droplet size with grid refinement. At BDC, mean diameter reduces by almost twice with the finest grid. Similar decrease is also observed at other piston positions. Magnitude of increase in size along the flow direction reduces with grid refinement as seen in Fig. 4.27. Results from the table indicate that for Grid – 1, mean diameter increases by 78 % from BDC to TDC whereas for Grid – 2 it is 70 % and for Grid – 3 there is a 50 % increase. With further refinement, it might be possible to minimize or completely eliminate this increase in droplet size.

(x 10^{-3} m)	**BDC**	**S/4**	**S/2**	**3S/4**	**TDC**
Full LES	0.34 (±0.04)	0.35 (±0.08)	0.47 (±0.08)	0.52 (±0.09)	0.60 (±0.09)
Grid - 1	0.33 (±0.02)	0.37 (±0.05)	0.42 (±0.04)	0.50 (±0.06)	0.59 (±0.09)
Grid - 2	0.20 (±0.05)	0.22 (±0.02)	0.24 (±0.08)	0.28 (±0.04)	0.34 (±0.03)
Grid - 3	0.18 (±0.01)	0.21 (±0.03)	0.23 (±0.02)	0.26 (±0.04)	0.27 (±0.03)

Table 4.4: Mean diameter results at local piston positions

Fig. 4.28 shows instantaneous probability distribution of droplets obtained with different girds. PDF is plotted in logscale along the y-axis. Results correspond to the location at the vicinity of TDC and a definite enhancement in droplet count with grid refinement can be observed. Minimum diameter reduces from 2.27 x 10^{-4} m with Grid - 1 to 1.85 x 10^{-4} m with Grid - 3. Differences in the tail of these distributions are evidence of relative coarseness (insufficient resolution) of the grids, Grid - 1 and Grid - 2 when compared to Grid - 3. Bigger structures are still present with the former grids indicated by the finite PDF value. With refinement, these are broken down and add to the count of smaller structures, as they should be. Subsequent improvement in resolution may result in even smaller structures and complete disappearance of bigger ones, and at some point the solution should become grid independent denoting exact reproduction of the actual flow. But, the level of refinement necessary to reach that stage is still unknown and remains as an open question.

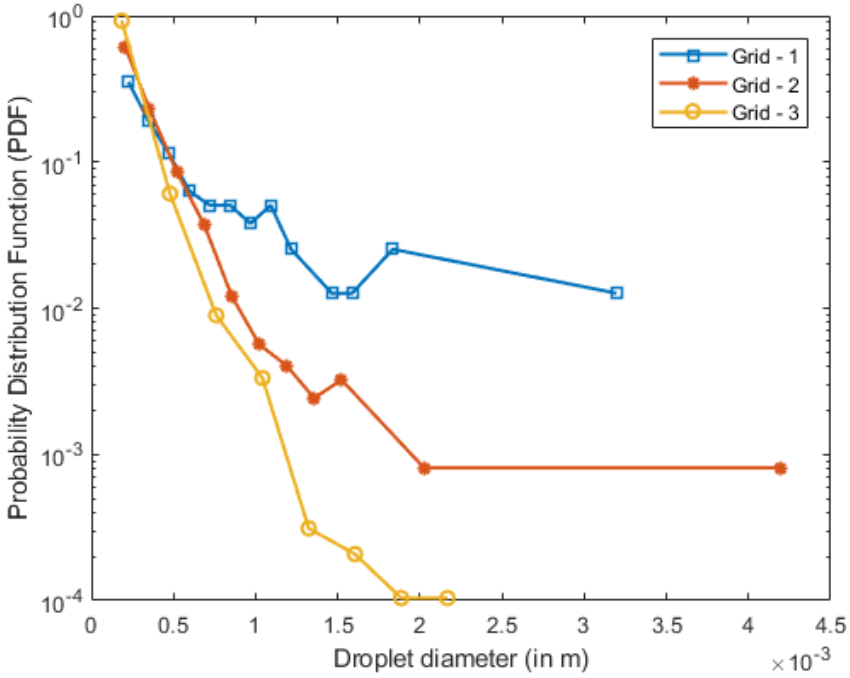

Figure 4.28: Droplet size PDF comparison near TDC for the three tested grids.

4.6. Conclusion

The primary goal of this chapter is to establish the physics of oil jets to provide better insight into the piston cooling process. This is achieved successfully through a detailed investigation of jet structures and critical evaluation of results obtained with validated LES model. Qualitative and quantitative characteristics of the jets studied are summarized in Appendix D. These observations are also applicable to liquid jets in general, that fall under these regimes. Some discrepancies related to flow physics and grid resolution are observed in the results and they are addressed with a separate LES analysis using a modified domain. The main conclusion are as follows.

Typical characteristics and evolution pattern

Overall characteristics of oil jets such as breakup, spreading, production of ligaments and droplets are completely dependent on its flow rate (or turbulence level) which helps to classify the jets as laminar, transitioning and turbulent. Four zones are identified based on jet appearance: undisturbed, sinuous wave, pre-breakup and post breakup. Each jet exhibits characteristics of at least one of them irrespective of its flow rate. There is a clear transition from fully intact jet at 3 L/min to complete disintegration at 7 L/min, due to the enhancement in disruptive forces which is the turbulence of the jet and not aerodynamic interactions as cited by Celik [3]. Thus, flow rate efficiency is maximum for gallery cooling at 3 L/min and decreases thereafter. In between, jets have similar characteristics such as protruding ligaments, intermittent pinch-off and absence of breakup until TDC which are attributed to the transitioning nature.

Droplet size results

Jets at higher flow rates (6 L/min and 7 L/min) spread more and exhibit significant number of ligaments and droplets enhancing spray cooling. Droplet diameter quantification is done for 6 L/min case only at TDC, and for 7 L/min at five selected piston positions. Droplet sizes are always greater than grid size used, due to inability of the grid to capture smaller ones. Results show that CDF trends are very similar to log-normal probability for all cases. Maximum droplet diameter is in the same order of integral length scale of turbulence

and/or the nozzle diameter. Mean Results at 7 L/min show increasing droplet size from BDC to TDC. This is considered a discrepancy and investigated further.

Assessment of grid resolution

Apart from discrepancy in droplet size results, for the turbulent jet, visual inspection shows an increased number of ligaments than droplets. For transitioning jets, protruding ligaments, wavering, absence of breakup until TDC and insignificant variation in breakup length are some of the characteristics which are considered as inconsistencies. These are studied further and verified with a grid refinement analysis using a small domain.

Small domain analysis

A small cylindrical domain with periodic boundary conditions is used with three different grid sizes.

- Grid refinement has no effect on laminar and transitioning jets. Structure obtained with full LES model for transitioning jet and its characteristics are due to the flow physics and not grid resolution.
- For oil at 7 L/min, insufficient grid resolution is found to be the cause of all the observed discrepancies.
  - Droplet count increases with increase in grid resolution. Restriction posed by combination of grid size and VOF model in full LES analysis causes droplet coalescence and results in bigger ligament structures. Ability of grid to resolve smaller droplet structures is verified as the finest grid tested produces mean droplet sizes twice as small as the coarsest grid.
  - Increase in droplet size along the flow direction is also shown to be minimized with fine mesh and may be completely eliminated with further refinement.
  - A minor increase in spreading is observed near TDC, and this will impact piston cooling process by augmenting spray cooling.

Thus, with the refinement analysis all the inconsistencies are addressed.There is an increased droplet production with fine mesh and the level of refinement required to reach actual flow conditions remains an open question at the end of this study. It is computationally inefficient to run the full LES model as the simulation becomes too expensive (using Grid - 3 setting, increases total cell count of full LES model by 8 times). In the following chapter, effect of turbulent atmosphere on oil jets are studied and same set of results are quantified to identify the differences.

5

Effect of turbulent atmosphere on piston cooling jets

The final sub problem of this project is to study the effect of turbulent atmosphere on oil jets. As mentioned in chapter 1, piston cooling jets are injected into surroundings that is in constant motion and it is important to quantify these flow components to test their effects on jet breakup and ligament/droplet production. As mentioned in section 2.3, fluctuating atmosphere in crankcase can be split into co-axial and cross flow elements. These can be imposed on oil jets in isolation, to see their respective impacts on parameters relevant to piston cooling like flow rate efficiency and droplet sizes. For this purpose, first, an analysis on turbulence within the crankcase is carried out. A simple 3D CFD model is constructed and reciprocating piston motion is modelled to simulate crankcase flow. An estimation of fluctuation in co-axial and cross-flow velocity components is obtained which are then used to perform LES analysis of oil jets. In this investigation, a modified domain is used to examine the initial effects of co-axial and/or cross flow on oil jets at selected flow rates. Based on the results obtained, this is then extended to a full domain LES.

This chapter is structured as follows. First, the analysis performed on crankcase flow is presented in section 5.1. Results from this study are used for examination of oil jets with LES which is discussed in section 5.2.

5.1. Crankcase turbulence

In this section, the research performed on crankcase flow is presented. Steps taken while constructing the simulation are given in section. 5.1.1. Pressure, mass flow and velocity results are presented in section 5.1.2. Finally, similar to 2.3.3 estimation of liquid to gas momentum ratios is done in section. 5.1.3, using the computed liquid velocities from LES and gas flow velocities from 5.1.2.

5.1.1. Computational setup

Geometry

PACCAR's MX-11 engine configuration is selected as base geometry for this study. Table. 5.1 summarizes important specifications of the engine and operating conditions under consideration. The CAD version of MX-11's engine block with sump is shown in Fig. 5.1.

Number of cylinders	6
Bore	0.123 m
Stroke	0.152 m
Crankcase operating pressure and temperature	Typically ~ - 1 kPa and lower; 100 ° C
RPM tested	1300

Table 5.1: PACCAR MX-11 engine specification

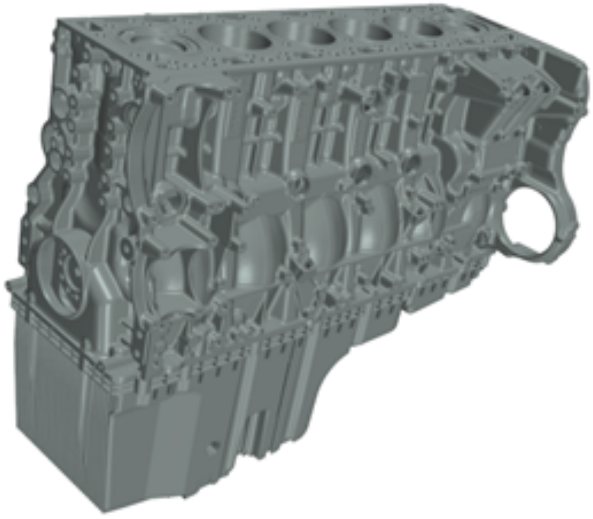

Figure 5.1: MX-11 engine block and sump

From this CAD model of the actual engine, only the regions wetted by air within the crankcase are of interest. Parts that do not have significant influence on the bulk flow motion are removed. These parts include: piston pins, bearings, bolts, PCJ nozzles, oil pipes, outer layer of liners and piston rings. Connecting rod are also neglected: their motion may affect the radial flow components and vortices but does not have as much impact as the pistons in pressure/velocity variation [60, 62, 63]. Crankshaft is assumed to be stationary following the approximation of Fogliarino [63] and others as mentioned in section 2.2.3. Piston shape is modified to represent a simple closed cylindrical structure, as shown in Fig. 5.2.

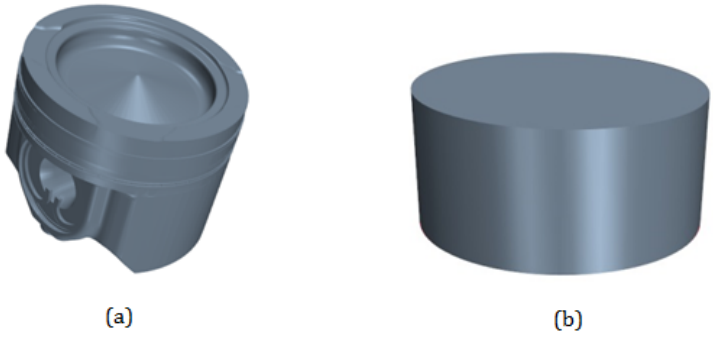

Figure 5.2: (a) Original MX-11 piston geometry and (b) Simplified piston surface for the present analysis

Sump volume is also modified. Actual MX-11 engine sump contains typically around 36 liters of oil and also houses the oil pump in it. Rest of the sump is filled with air. For the present study, assuming that the oil free-surface is stable, the sump volume is reduced by subtracting the volume equivalent to the amount of

oil and the volume of pump from the original sump geometry given in Fig. 5.1. The final simplified model is shown in Fig. 5.3.

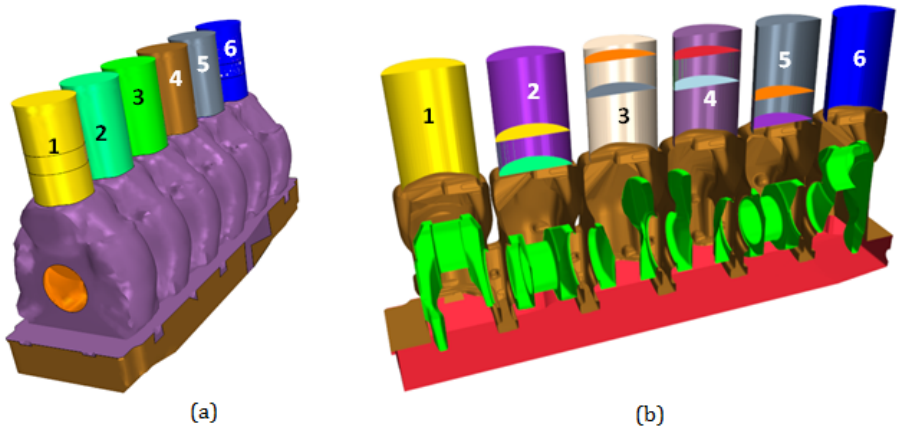

Figure 5.3: (a) Isometric view and (b) sectional view of the simplified final geometry with cylinder numbers

Meshing

Structured mesh is used due to their reduced computational requirements. Uniform mesh with a base size of 5x 10^{-3} m and least cell size of 5x 10^{-4} m is generated, giving a total of 3.3 Million cells. Near-wall region is not refined to account for the boundary layer, as the focus is on the bulk flow and wall effects are minimal. Fig. 5.4 shows the mesh constructed for present analysis.

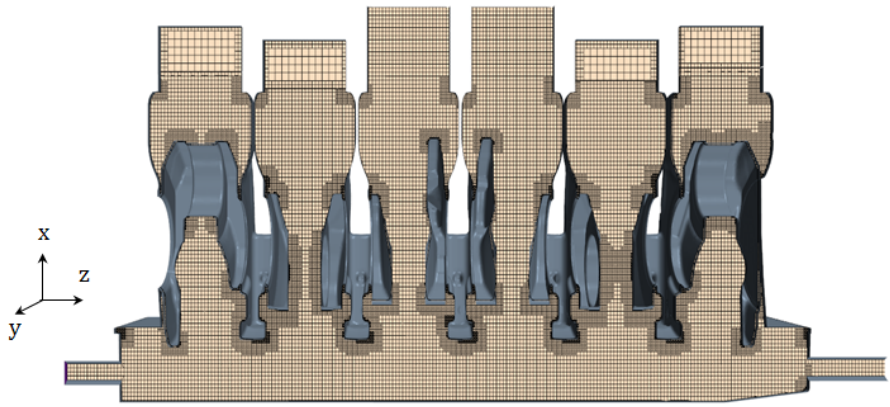

Figure 5.4: Sectional view of the structured grid used for present analysis

Piston motion is modelled with overset meshing, described in section 2.2.5. Overset zero-gap interfaces are created for the pistons. For any zero gap configuration, either the background (stationary region) or the overset region (dynamic region), or both, may approach each other with minimal gap and/or make contact. When the gap reduces to a minimum value which is a user-specified number of cell layers, zero gap algorithm is activated, and those cells become inactive [71]. The default value of 3 layers is used for the simulation. Linear interpolation method is used for overset physics. Additional models such as close proximity and alternate hole cutting are employed, as recommended by StarCCM+ [71]. Piston wall is assigned with a overset topology which detects the motion specified and deactivates the cells above the piston.

Physics models and solver settings

With this mesh, 3D unsteady simulations are carried out with air as the working fluid. Density is modelled with ideal gas due to the presence of continuous pressure fluctuations within an engine cycle. Turbu-

lence is modelled using RANS approach using Realizable k- model. Since the primary focus is to capture the essential physics of bulk flow and not near-wall, this model is sufficient. Near-wall modelling is done using the High y+ wall treatment which allows y+ to be above 30. Piston motion is modelled using overset meshing and specified through tabular data of piston velocity at every crank angle for a cycle. Fig. 5.5 is a representation of velocities of pistons 1, 2 and 3. Symmetry in motion is observed about a plane after cylinder three, i.e., pistons 4, 5 and 6 replicate 3, 2 and 1 respectively. All other faces of the domain are set as adiabatic no-slip walls. Analyses are done using segregated solver. Implicit unsteady scheme is employed and second order technique is used for convection and temporal discretization. Time step of 5 x 10^{-4} s (3.9 ° CA) is used.

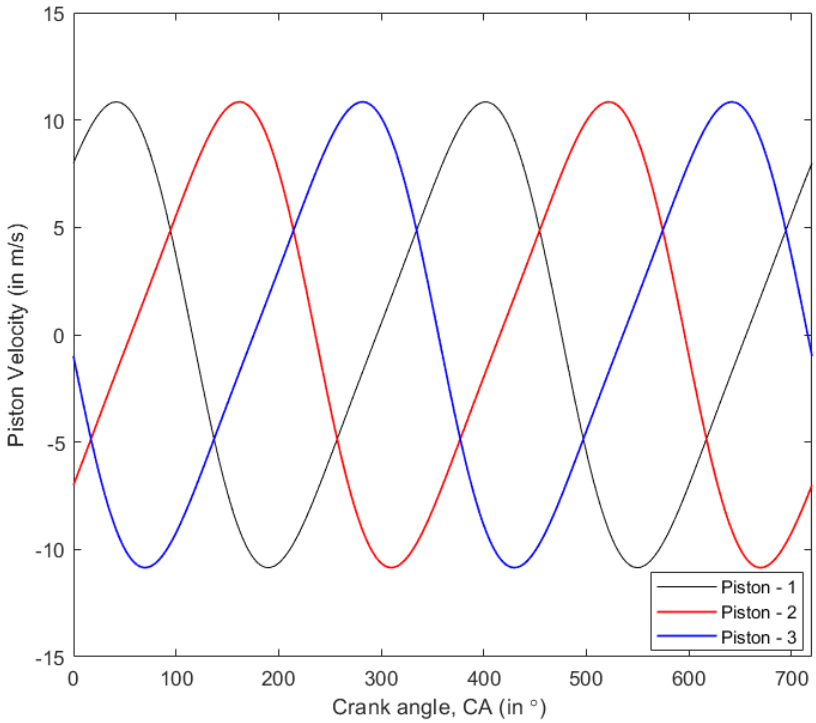

Figure 5.5: Piston velocity input data

Contributions to the crankcase flow through continuous blow-by and ventilation were neglected and preliminary analyses were performed with closed domain as shown in Fig. 5.3. However, this model diverged due to mass conservation error of overset meshing. The model could not be optimized by modifying different settings used, such as discretization techniques or solver settings. Hence, a stagnation inlet and mass flow outlet are attached as shown in Fig. 5.6. This modification represents blow-by and ventilation flows of real engines. Due to the lack of availability of data for both blow-by and ventilation configurations at the company, these attachments could not be constructed accurately. However, they aid in resolving the convergence issue. Based on trial and error, pressure difference of 20 kPa across the inlet is found to be suitable to achieve faster stabilization of flow within the crankcase. The simulation is initially run with a frozen solver for piston motion and the flow across inlet-outlet is allowed to stabilize. When the mass imbalance reduces to a negligible value (~ 0.1%) piston motion is activated. The simulation is then run for 12 cycles (8640 ° CA) to achieve pressure convergence within the crankcase.

No measurement data is available at the company, of parameters like crankcase pressure, temperature or velocity, which makes validation of this CFD model impossible. Hence, pressure and mass flow rates are quantified within the crankcase and qualitative observations are compared with literature to show that the model produces realistic results. To determine pressure fluctuation within the crankcase, pressure probes

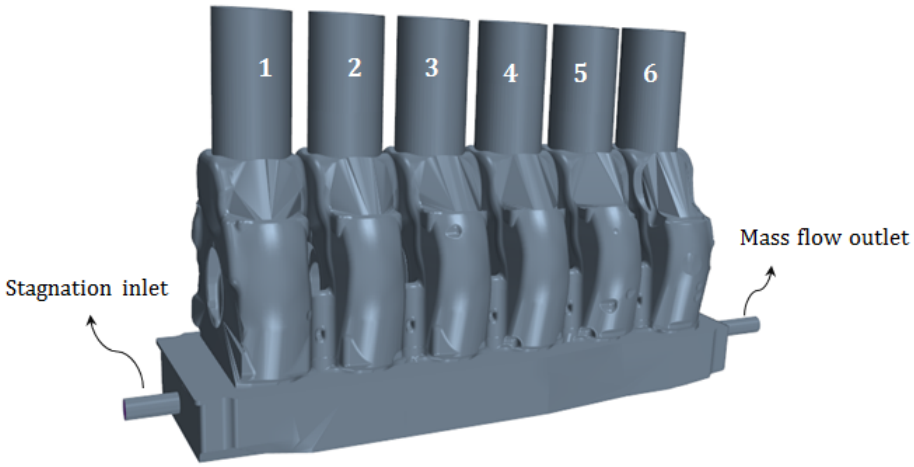

Figure 5.6: Modified geometry with inlet and outlet attachments

are constructed as shown in Fig. 5.7. Surface average values of absolute static pressures are computed on these planes and is monitored as a function of crank angle. This is followed by quantification of velocity components' variation within the crankcase.

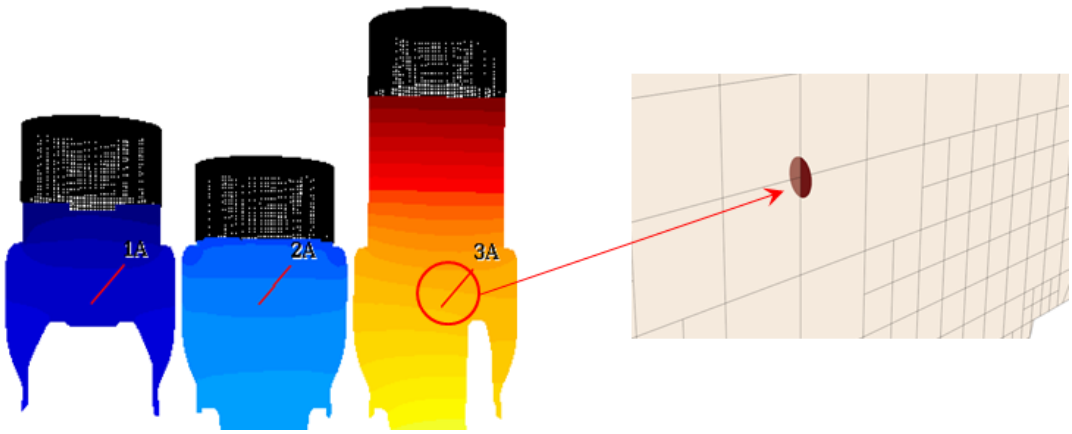

Figure 5.7: Pressure measurement locations

Mesh sensitivity

Effect of grid size on pressure fluctuation is investigated by constructing two more grids with base sizes 4 x 10^{-3} m (fine) and 6 x 10^{-3} m (coarse). Results obtained in cylinder 1 are presented in Fig. 5.8, and with every refinement of 1 x 10^{-3} m, absolute pressure decreases by 0.4% at each crank angle. Similar results are observed in other cylinders as well. This difference is negligible and the initial grid is considered to be reliable, as the overall trend remains the same.

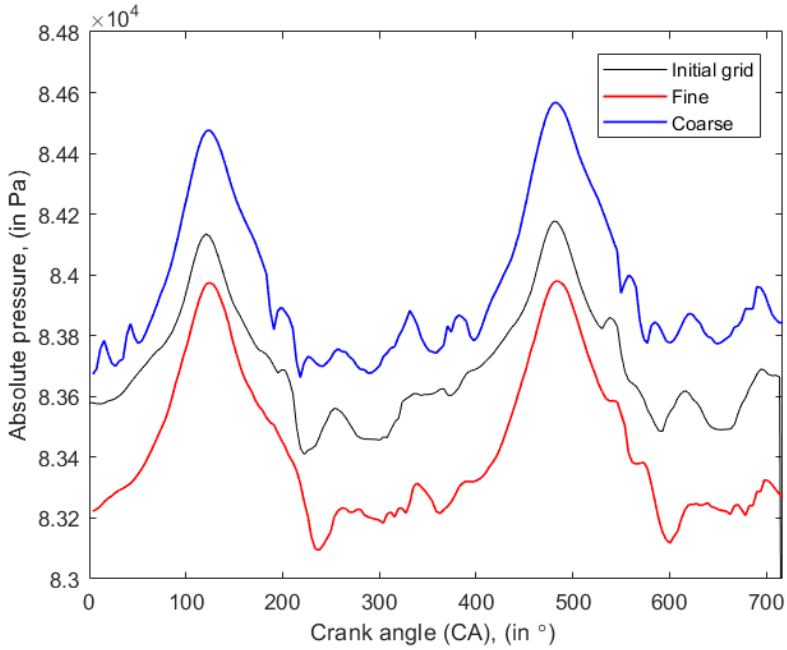

Figure 5.8: Mesh sensitivity analysis results

5.1.2. Results

Pressure fluctuations and breathing effect

Results are presented in Fig. 5.9. Due to the symmetric nature of piston motion, only the results in cylinders 1, 2 and 3 are given. As mentioned in section 2.2.4, in an ideal closed cylinder configuration, pressure variation is polytropic and varies inversely as volume. Also, the fluctuating trend is sinusoidal. For the present case, all 6 pistons are in motion and the breathing between the bays influences pressure. This leads to the type of variations observed in Fig. 5.9 where pressure is in phase with piston motion because of mass exchange between the cylinders, as observed in literature [63]. Absolute total pressure does not differ much from the results presented in Fig. 5.9, as the dynamic quantity contributes only a maximum of about 0.04 kPa.

Pressure under piston 2 is most affected because of two-way communication with cylinders 1 and 3. Δp_{max} jumps are about 0.2 – 0.4 kPa (±0.03 kPa) in cylinder 2 within a single stroke (eg. 180° CA to 360° CA). In cylinders 1 and 3 (also 4 and 6), Δp_{max} 0.7 kPa (±0.03 kPa). This higher amplitude is due to limited breathing area available under those pistons, hindering gas flow from one side. This can be understood with the help of average mass flow rate quantified along the planes between the cylinders (Fig. 5.10 (a)).

Mass flow rate results are presented in Fig. 5.10 (b). On one side, crankcase walls are present near cylinder 1 and all of the flow has to pass through the plane P1 resulting in higher magnitude. P2 is the plane between cylinder 2 and 3, and mass flow across this plane is higher because of breathing between cylinders 2 and 3, and the breathing between 1 and 2. The lowest exchange is observed across plane P3 which separates cylinders 3 and 4. Since, piston motions in both these cylinders are symmetric, they inhale and exhale at the same time, cancelling mass exchange and resulting in very small contribution that comes from other two cylinders.

Velocity components results

As mentioned in section 2.3, to study the impact of turbulent atmosphere on oil jet breakup, it is important to estimate velocity components' fluctuation as a function of crank angle. Relative magnitude of the

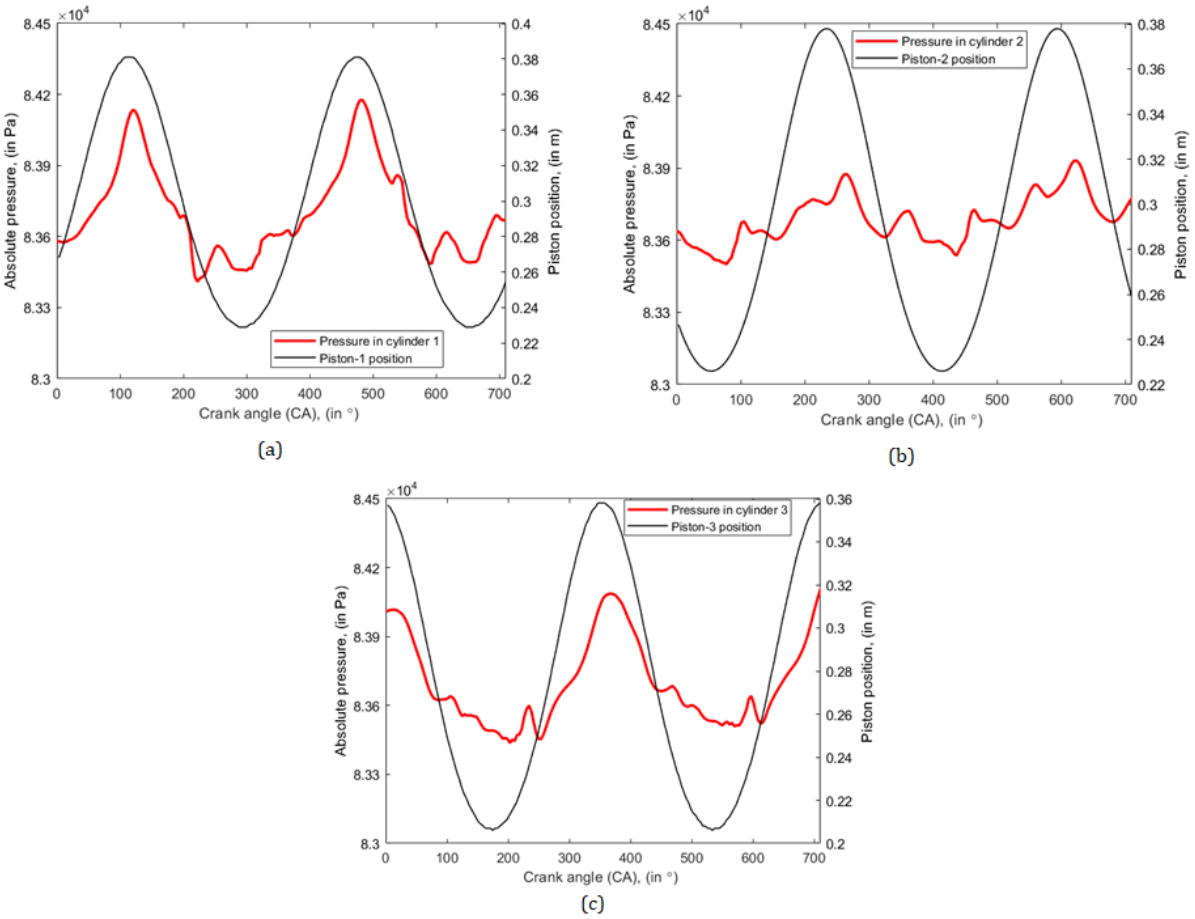

Figure 5.9: Pressure fluctuation as a function of Crank angle, in (a) cylinder 1, (b) cylinder 2 and (c) cylinder 3

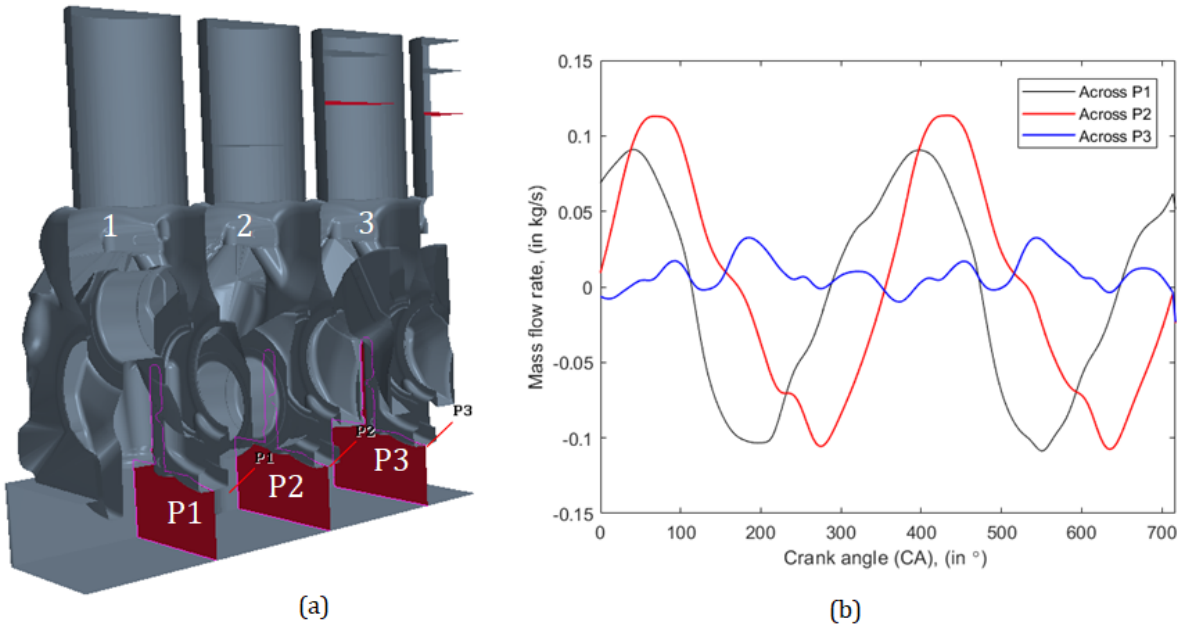

Figure 5.10: (a) Planes constructed for estimating breathing effect and (b) mass flow rate across these planes

velocities aid in identifying which component(s) has(have) a major impact on piston cooling jet evolution. This identification process is carried out based on following results. Fig. 5.11 shows the velocity components estimated inside all three cylinders. Clearly, V_x is greater than the other two in all cylinders because of reciprocating nature of pistons. The amplitude of fluctuation in V_x is lowest in cylinder 1 ($\Delta V \sim 8$ m/s). In cylinders 2 and 3, it is approximately the same ($\Delta V \sim 12$ m/s). V_y and V_z are small due to the radial components exists when the piston changes its direction at BDC and TDC. In cylinder 1, V_y is almost zero. However, in other two cylinders, it is higher and has a maximum of around ± 2 m/s. V_z varies around zero in all three cases.

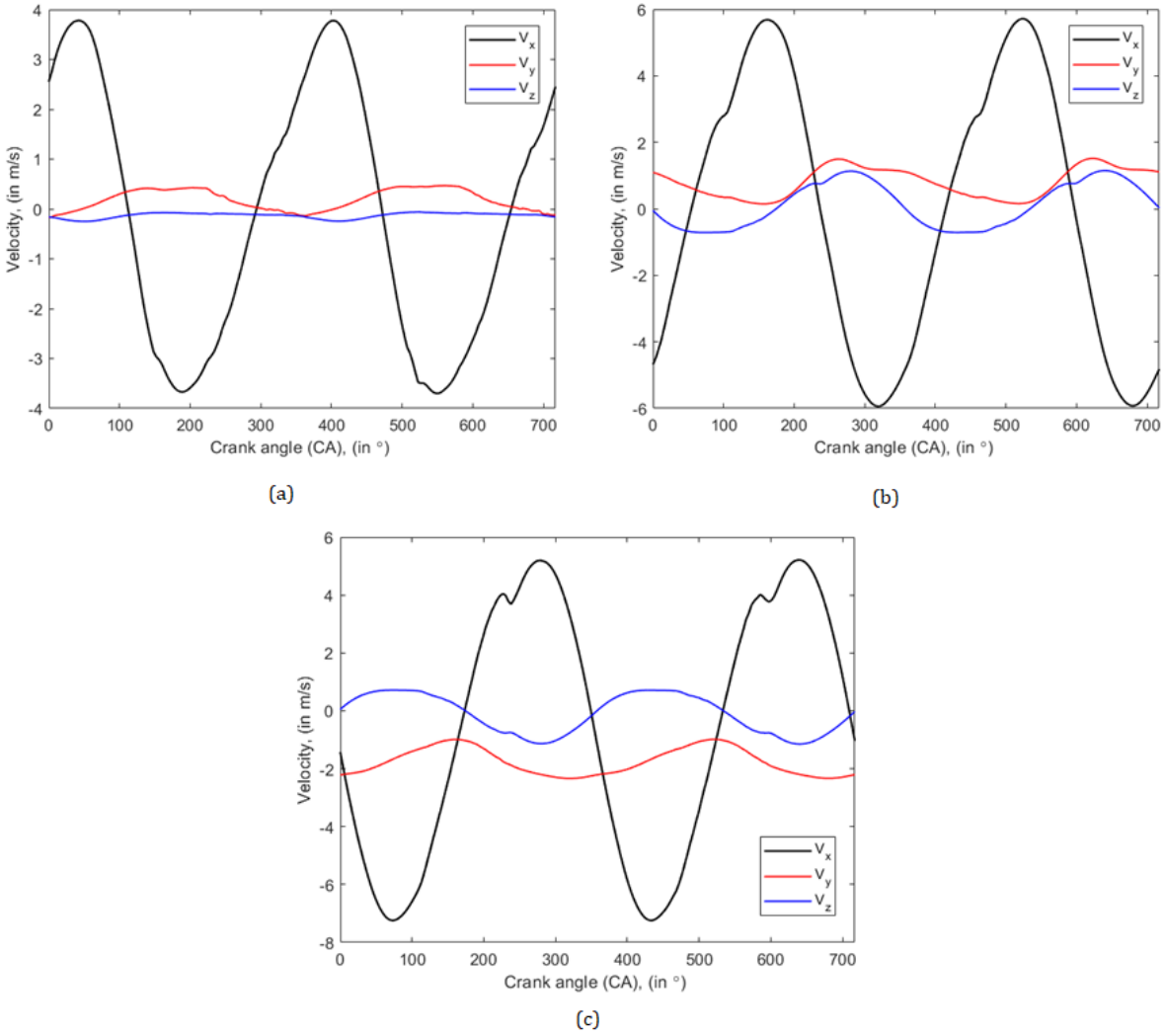

Figure 5.11: Velocity components versus crank angle in cylinder (a) 1, (b) 2 and (c) 3. (Change picture to matlab format)

5.1.3. Estimation of effect of surrounding flow on oil jets

Results presented in the previous section indicate that the component V_x is significantly higher than the other two. This is along the same direction as the axis of oil jets. Thus, co-axial air flow (when piston is moving up) and counter-axial air flow (when piston is coming down) will have the highest degree of influence on jet evolution within the crankcase.

Flow rate (L/min)	**Liquid velocity, V_L (m/s)**	V_g (m/s)	$V_{g,cf}$ (m/s)	M (x 10^3)	M_{cf} (x 10^5)
3	7.1	5.5	1	1.4	0.41
4	9.4	5.5	1	2.4	0.71
5	11.8	5.5	1	3.7	1.12
6	14.1	5.5	1	5.3	1.61
7	16.5	5.5	1	7.3	2.20

Table 5.2: Liquid to gas momentum ratio for different liquid flow rates

For liquid jets with co-axial and cross-flows, it is important to determine the magnitude of inertial force of each phase to anticipate the type of impact on jet breakup process. Table - 5.2 gives momentum ratio M and M_{cf} (given by (2.35) and (2.37) respectively) for all simulated oil flow rates using LES. Axial air flow velocities (V_g) given in the table, are estimated by taking the average of (absolute) maximum of V_x obtained in all three cylinders. Cross air flow velocity, $V_{g,cf}$ is also determined in a similar manner using V_y and V_z. From the table, for each oil flow rate $M >> 1$, similar to the estimation made in section 2.3.3. The magnitudes of M are higher than those in table 2.2 and the impact of co-axial flows on oil jets will be low according to literature. Table-2 also shows the liquid-to-gas momentum M_{cf} and the liquid momentum is higher by several orders of magnitude ($M_{cf} \sim 10^4 - 10^5$) when compared to cross-flow momentum. Thus, cross flow effects on liquid jet evolution process can be neglected.

5.2. LES of oil jets in turbulent atmosphere

Results obtained from crankcase turbulence analysis show that the air flow due to reciprocating piston is dominant along the axis of piston cooling jets. Hence, in this section, evolution of oil jets with co-axial and counter axial flow is investigated. With co- or counter-axial flows, laminar jet may have minor impacts on its surface structure without introduction of aerodynamic induced breakup [78]. Influence of aerodynamics on transitioning and turbulent jets with low speed co-axial flows, is unknown. Disturbance due to aerodynamic interactions can have minor impacts on jet structure until initial detachment. Further downstream, although air flow may not entirely modify the primary breakup mechanism due to the significantly higher inertia of the liquid phase, its effect on detached ligaments and droplets may be present. Droplets that form post primary breakup can get carried by the air stream away from the jet with both co-axial and counter-axial flows, as mentioned in section. 2.3.3. This in turn, will affect the amount of oil entering the gallery and the flow rate efficiency. For jets in transition, ligaments and droplets that pinch-off may have similar experience. The air stream can also disturb protruding elongated ligaments and increase surface breakup. Thus, even though the estimations suggest otherwise, it is important to study the impact of surrounding air flow to see how oil jet evolution is affected especially post initial detachment.

5.2.1. Computational setup

Domain used for the analysis is same as that given in Fig.3.3, and mesh settings given by Table 3.1 are maintained. Computational constraints limit the analysis to using these grid sizes, which, according to section 4.5, provide insufficient resolution to capture varying droplet sizes of the actual oil jet. Velocity inlet conditions are used for allowing air flow into the domain. Values are specified from those obtained in table 5.2 as components, with V_x = 5.5 m/s (co-axial) and V_x = -5.5 m/s (counter axial). V_y and V_z are maintained at zero and all other simulation settings are maintained the same (section. 3.2.3).

Variation in jet structure due to surrounding flow is examined in section 5.2.2, followed by quantitative comparison of flow rate efficiency and droplet sizes in section 5.2.3. First, oil at 7 L/min (turbulent case) is tested to determine the impact of co-axial and counter-axial flows on primary and secondary breakup. Based on the results obtained, the analysis is extended to the 3 L/min (Laminar) and 5 L/min (transitioning) cases whose results are presented in section 5.2.4.

5.2.2. Qualitative results - 7 L/min

Jet structures for the three cases are compared in Fig. 5.12. Until BDC, no significant change can be observed with co-axial or counter-axial flows as primary breakup continues to occur near its vicinity. Jet characteristics after breakup are similar to earlier observations without airflow and this is reflected in flow rate efficiency and droplet size results shown in Tables 5.3 and 5.4 respectively.

Case	**7 L/min**
Quiescent atmosphere	97(±0.45)
Co-axial flow	97.2(±0.52)
Counter-axial flow	95.5(±0.65)

Table 5.3: Flow rate efficiency at BDC. Results in comparison with quiescent atmosphere case

Case	**Mean** (x10^{-3} m)	**Minimum** (x10^{-3} m)	**Maximum** (x10^{-3} m)
Quiescent atmosphere	0.34(±0.02)	0.22(±0.02)	1.60(±0.10)
Co-axial flow	0.32(±0.02)	0.22(±0.01)	1.45(±0.04)
Counter-axial flow	0.31(±0.03)	0.21(±0.20)	1.5(±0.10)

Table 5.4: Droplet sizes at BDC. Results in comparison with quiescent atmosphere

Similarity of results until BDC between the three cases show that primary breakup is controlled by turbulence level of the jet. As estimated in section 5.1.3, liquid phase inertia dominates over the surrounding flow and these observations are consistent with literature [16, 79, 81]. Moving downstream, especially in the upper half of the cylinder, disintegrated liquid structures get affected as droplet formation due to Rayleigh breakup (pinch-off) at ligament tips and surface stripping increase due to increased aerodynamic interactions. Near TDC, jet structure is clearly modified, especially for the counter-axial case (Fig. 5.13 (c)). The jet is more chaotic and appears to have increased disintegration mainly because the counter flowing direction of the air medium adds to the disruptive factors of breakup.

This can be better understood by considering the relative inertia between droplets and surrounding air flow, similar to the parameters M and M_{cf}. However, the same cannot be used as they do not account for a characteristic length scale, such as nozzle diameter or droplet sizes, which are also important to compute inertial forces. Thus, Weber number given by (2.1.5) is calculated for both phases and its liquid-to-gas ratio $\frac{We_L}{We_g}$ is determined. Until primary breakup, where jet retains its intact nature, reference length scale is the nozzle diameter and this ratio is ~ 500. In the upper half of the engine cylinder, where droplets are involved, mean droplet diameter is considered to be the reference length and the ratio is found to be ~ 50. This reduction in order of magnitude of $\frac{We_L}{We_g}$ is a result of decreased inertial force of liquid phase due to disintegration and spreading. This allows gas phase to have higher impact on the detached structures influencing secondary breakup more, leading to the observations presented in Fig. 5.12 and in the following section.

Increase in local spreading will result in more spillage and lesser flow rate efficiency for gallery cooling. Droplet production at this location is also modified and these have to be further verified with parametric quantification, which are presented in the following section. Although, figures Fig. 5.12 and Fig. 5.13 do not show significant variation for co-axial case, quantitative results in the following section show some differences.

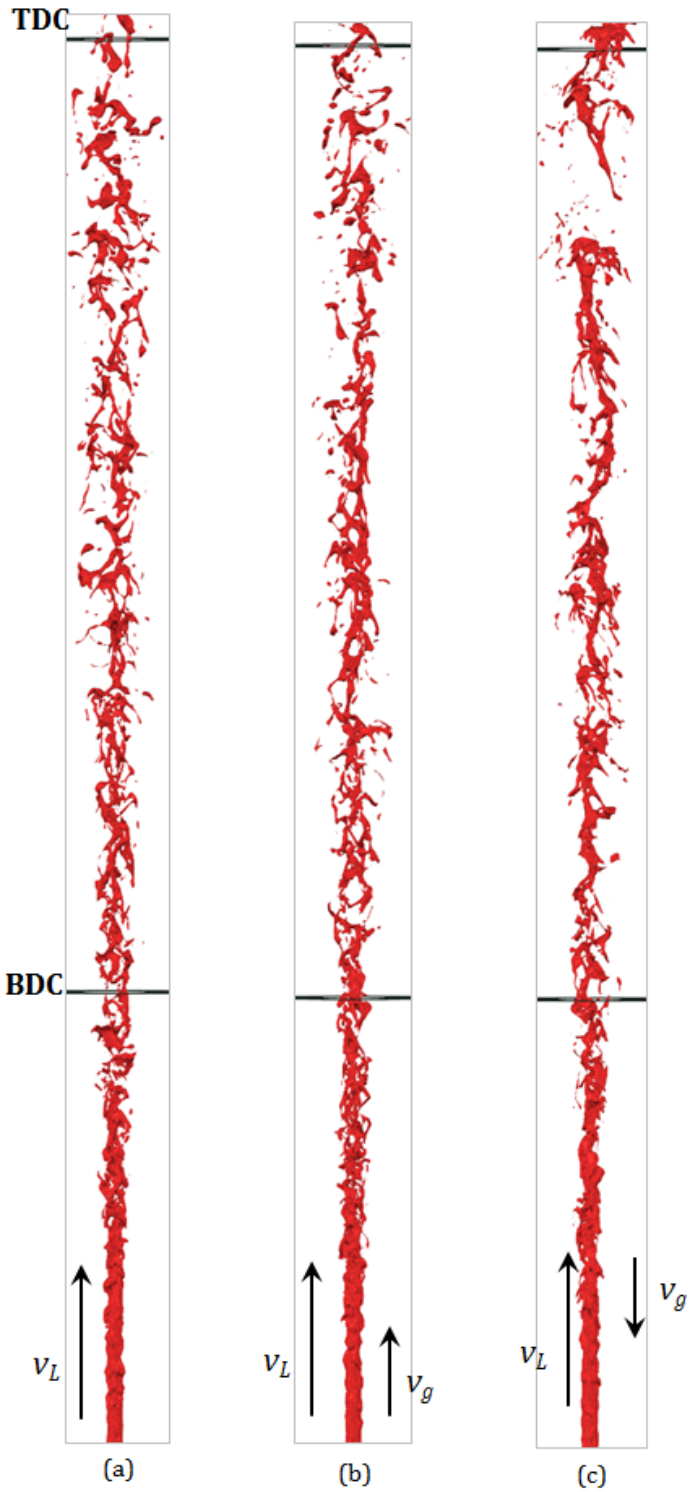

Figure 5.12: Oil jet at 7 L/min (a) in Quiescent atmosphere, (b) with co-axial flow and (c) with counter-axial flow

5.2.3. Quantitative results - 7 L/min

Flow rate efficiencies are quantified at five locations from BDC to TDC (Fig. 4.7), and results from different cases are presented in Fig. 5.14. Both co-axial and counter-axial atmospheres affect the amount of oil entering the gallery orifice at each measurement location and the impact increases from BDC to TDC. Among

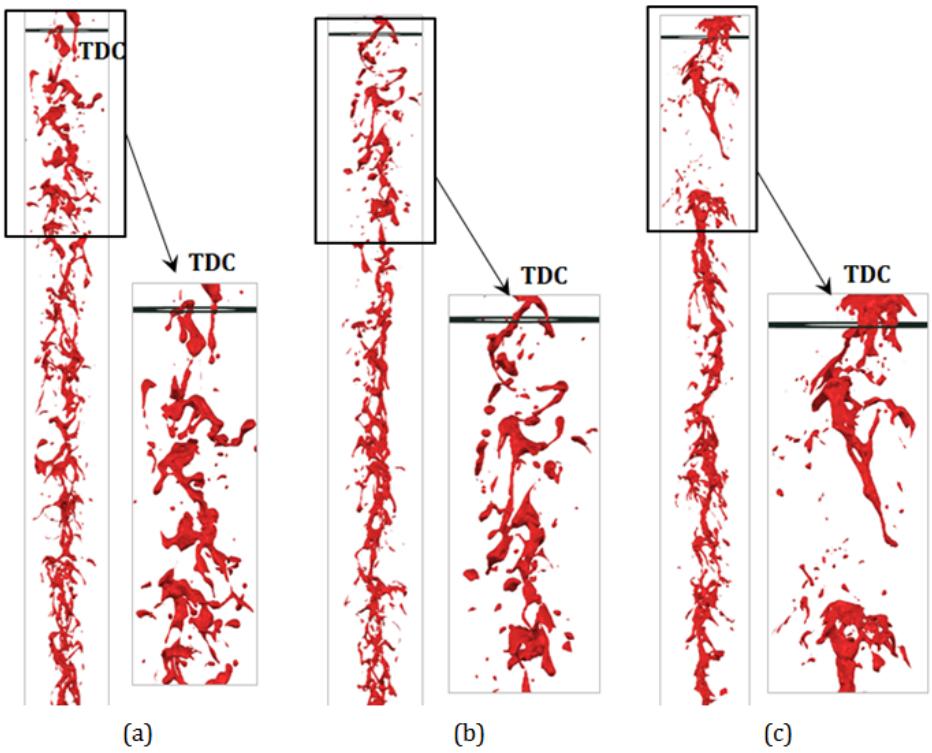

Figure 5.13: Oil jet at 7 L/min near TDC (a) in Quiescent atmosphere, (b) with co-axial flow and (c) with counter-axial flow

these cases, counter-axial flow has higher effect due to increased interactions, as discussed previously.

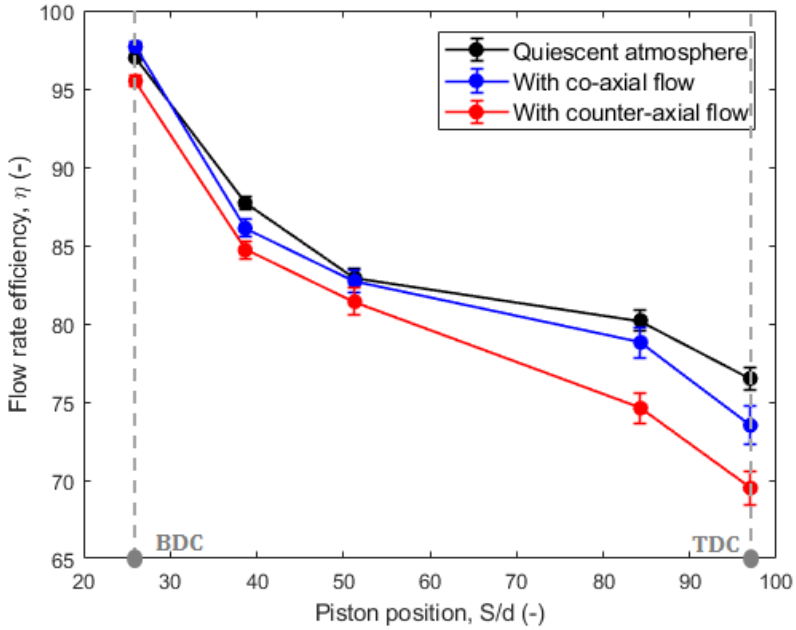

Figure 5.14: Comparison of flow rate efficiencies for the three different surrounding flow conditions

At BDC, the impact is least as the efficiencies vary by < 1% with co-axial flow and by < 1.5% with counter-axial flow, when compared with quiescent atmosphere case. This difference is enhanced, and at TDC, results

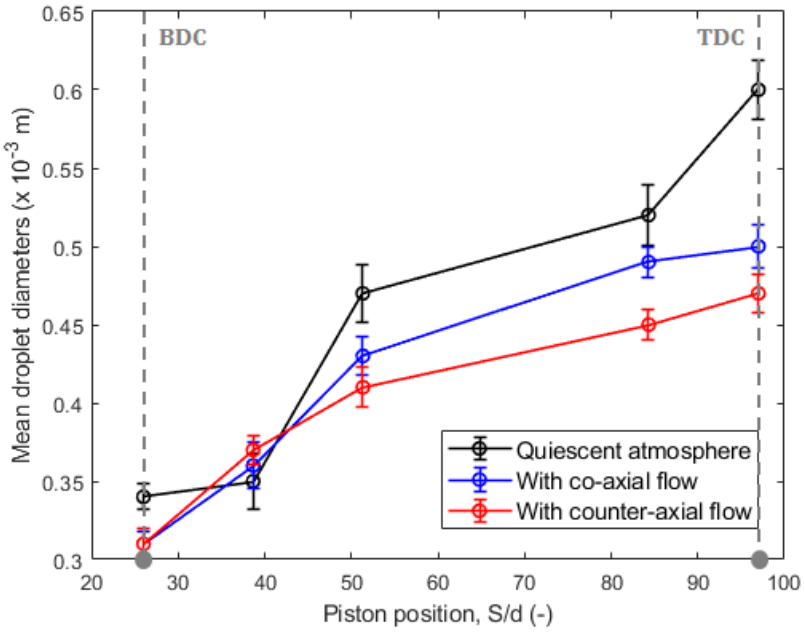

Figure 5.15: Comparison of mean droplet sizes for the three different surrounding flow conditions

are maximum affected with 4% lesser (relative) amount of oil in co-axial and 9% lesser in counter-axial case. Droplet size results from Fig. 5.15 also show similar behavior where mean diameter for the turbulent atmosphere cases are lower. At TDC, mean size decreases from quiescent atmosphere result by ~ 17 % for co-axial and by ~ 22 % for counter-axial flow, showing evident impact of surrounding flow on secondary breakup. Although current grid size may not be sufficient to resolve droplets of the actual flow, these observations are acceptable qualitatively and on the basis of order of magnitude of diameters.

Thus, both gallery and spray cooling techniques are affected, especially in the upper half of engine cylinder. The tested turbulent atmospheres have a negative impact on gallery cooling as they reduce η, whereas spray cooling is impacted positively, as increased secondary breakup can enhance spray impingement heat transfer. Analysis is extended to 3 L/min and 5 L/min case only with counter-axial flow, since that is found to have relatively higher influence based on the resulted obtained thus far.

5.2.4. Results for oil at 3 L/min and 5 L/min

Fig. 5.16 and 5.17 compare jet structures at 3 L/min and 5 L/min respectively, for quiescent atmosphere and counter-axial cases. No significant variation in the overall characteristics of the jet and nature of breakup can be noticed for both flow rates. Jet structures for the 3 L/min (Laminar case) remain mostly undisturbed until BDC, beyond which undulating patterns are modified in the sinuous wave region upon interaction with counter-axial air flow. High amplitude and shorter wavelength perturbations are observed over the jet surface in Fig. 5.16 (b) and these disturbances almost reach the centerline near TDC. However, these modifications do not result in primary breakup as the jet remains intact even post TDC due to its cohesive nature. This shows the dominance of liquid phase inertial force over that of the counter-axial air flow and the cohesive forces that dampen the development of interface perturbations. For the jet at 5 L/min, similar consistency between quiescent and counter-axial cases can be observed. Only near the TDC, aerodynamic interactions have some impact and they enhance disruptive forces leading to increased surface breakup (strip-off). Nevertheless, these deviations are minor and they do not impact the amount of oil entering the gallery orifice drastically, as flow rate efficiencies remain within the error bars plotted in the results of Fig. 3.19.

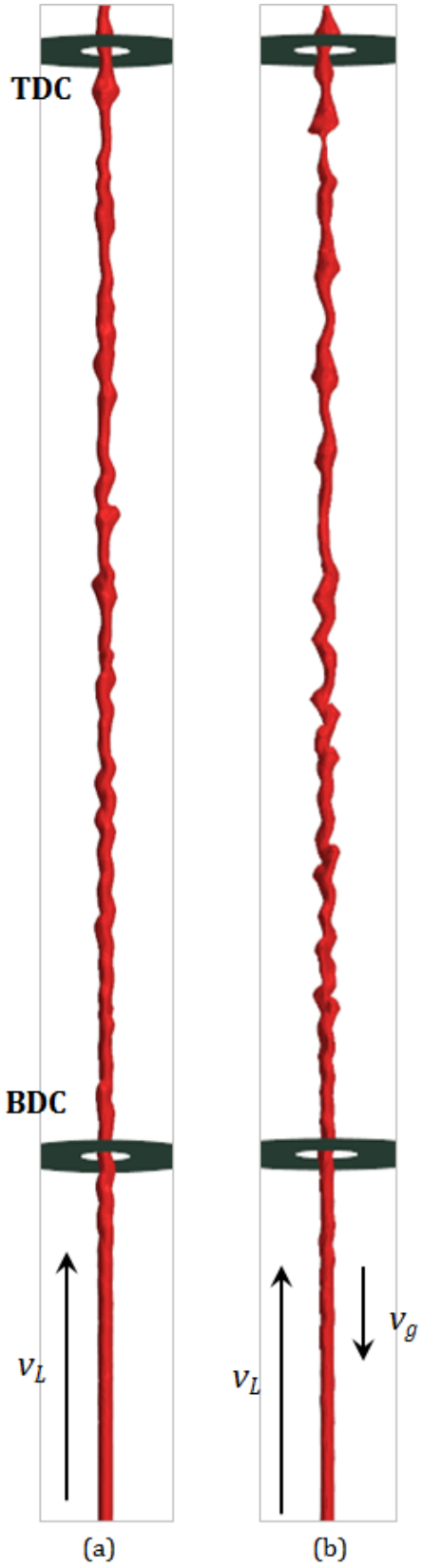

Figure 5.16: Oil jet at 3 L/min (laminar) (a) in Quiescent atmosphere and (b) with counter-axial flow

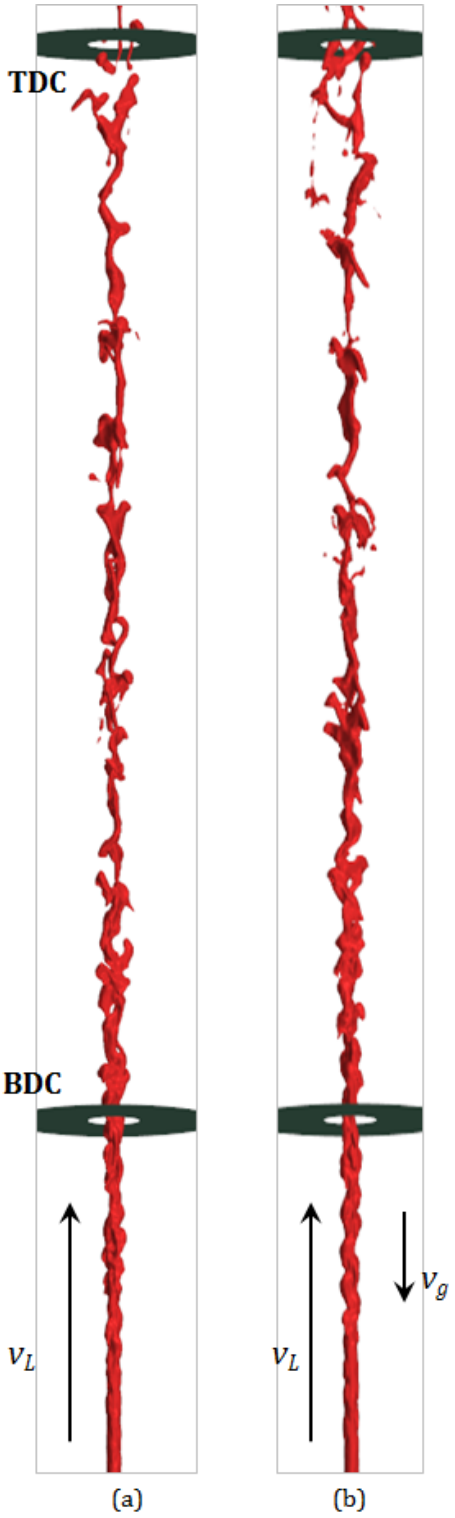

Figure 5.17: Oil jet at 5 L/min (Transitioning) (a) in Quiescent atmosphere and (b) with counter-axial flow

5.3. Conclusions

In this chapter, effect of crankcase turbulence on oil jet breakup is investigated. This is achieved by quantifying the flow field variation in the crankcase, and then employing the results as boundary condition for LES analysis to explore the effects on primary and secondary breakup of oil jets. Following paragraphs list

out the main conclusions obtained from the study,

Crankcase turbulence

Reciprocating piston motion affects pressure and velocity fields within the crankcase throughout an engine cycle. Pressure changes are in-phase with piston motion in all cylinders due to bay-to-bay breathing, and has maximum amplitude in cylinders 1 and 3 (also 4 and 6). Velocity fluctuation in the crankcase is maximum along the direction of piston motion (V_x) which allows for testing oil jets with co-axial and counter-axial air flow only. Cross-flow effects can be neglected. The model used for crankcase analysis has to be optimised by identifying appropriate blow-by (inlet) and ventilation (outlet) configurations, and using solver settings that produce the least overset mass conservation error.

Effect of surrounding flow on oil jets

Effect of surrounding flow on primary breakup is tested initially for oil jet at 7 L/min. Until BDC, jet structures and quantitative results of droplet sizes and flow rate efficiencies do not vary significantly from quiescent atmosphere, as anticipated through initial estimations. Liquid phase inertia dominates in this region and breakup physics is controlled by turbulence developed at the nozzle exit. This ensures similar levels of cooling until BDC irrespective of the surrounding flow condition.

Both gallery and spray cooling parameters are affected post BDC, especially in the upper half of the cylinder, as the aerodynamic effects are enhanced and the inertial force of turbulent atmospheres augment disruption and secondary breakup. Oil jet with co-axial and counter-axial flow has a degrading effect on gallery cooling and an upgrading effect on spray cooling with the counter-axial flow having the greater magnitude of impact. Results obtained from this study are using a coarser mesh size and a grid refinement analysis similar to section 4.5 is necessary to accurately quantify the deficit in droplet sizes corresponding to actual flow conditions. However, present results are representative of actual droplets in the order of magnitude and can be considered as preliminary values. Results obtained for oil jet at other flow rates with counter-axial air flow are similar to quiescent atmosphere and the air stream does not impact gallery or spray cooling properties.

From an engineering perspective, these results demand proper manufacturing of nozzles as their geometrical perfection is the main factor that governs flow development until primary breakup, dependant on which, level of secondary breakup and impact of aerodynamics exist. With this, required type of oil jet (either laminar or turbulent) at the exit can be obtained and the necessary amount of gallery and/or spray cooling, essential to control the piston surface, can be achieved.

6

Conclusions

The primary motivation behind this research work is to fill the knowledge gap at the company on the piston cooling technique. The complicated process is split up as shown in Fig. 6.1 and the first isolated component is studied extensively using LES and VOF methodologies. Oil jet characteristics at different flow rates are investigated qualitatively and quantitatively, by studying its evolution, first in quiescent atmosphere and then in turbulent atmosphere. Importance of grid size in multi-phase simulation involving droplets is stressed upon and through critical evaluation of results, the need for grid refinement is addressed. Parameters relevant to both types of cooling techniques are quantified and these results will serve as main inputs for future studies on spray cooling and gallery cooling as indicated in the figure. Main conclusions obtained from each and every sub-topic of this project are summarized in the following sections.

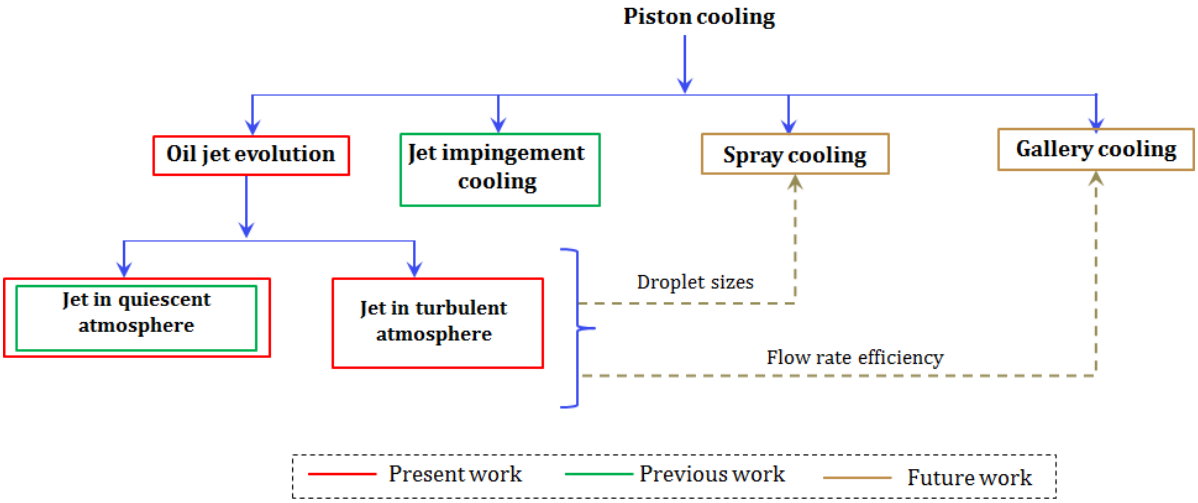

Figure 6.1: Piston cooling study at DAF split into previous, present and future work

6.1. Validation and oil jet characteristics

First, the study focused on improving the CFD model built by Celik [3]. This is achieved by realizing the significance of grid resolution for LES and droplet capturing through a detailed literature review. Several criteria are selected to assist mesh generation process and a model with better resolution than Celik is constructed for validation and preliminary analyses. With this, two test cases, turbulent water jet from literature [16] and flow rate experiment of DAF [65], are reproduced. Results of water jet show excellent qualitative con-

sistency with literature and typical physics at corresponding operating conditions. Quantitative agreement of breakup length and droplet sizes with experiment and/or correlations indicate that the grid resolution used is sufficient for the present test case.

LES results of test case – 2 are found to validate the flow rate efficiency (η) experiment with appreciable levels of accuracy. The model is able to reproduce the decreasing trend in η which is due to the increasing turbulent nature of the jets. Qualitative investigation of typical oil jet characteristics show a clear transition to turbulence with increase in flow rate. Summary of the observations is briefed in appendix D. Based on their structures, four zones are observed: undisturbed, sinuous wave, pre-breakup and post breakup zones and each jet exhibits properties of at least two of them. At higher flow rates, disruptive forces (jet turbulence) are enhanced and this augments disintegration leading to a chaotic and spreading jet, resulting in lesser amount of oil entering the gallery. Intermediate flow rates, that lie in the transitioning zone, are found to have similar characteristics like wave and protruding ligaments, surface breakup, and complete detachment from the liquid core at TDC.

6.2. Assessment of grid resolution

For both validation cases, results of LES quality satisfy the necessary condition (2.28) making the simulation reliable based on industrial standards. However, the sufficient condition (2.27) remains unsatisfied near the jet exit in some cases and around the interface. Presence of poor quality cells within the jet region is an indication of inadequacy of the present grid in resolving large scale turbulent eddies which control the breakup and droplet formation process. This calls for a grid refinement study. Further, observations in transitioning oil jets such as elongated ligament protrusions, lack of primary breakup till TDC, and droplet size results of turbulent jets, deviate from expected results. This could be due to numerical droplet coalescence caused by insufficient grid size combined with VOF model constraints and can be verified only by testing finer grids. These reasons make grid refinement analysis indispensable.

A small domain with periodic boundary conditions is used to test three different grids. For laminar and transitioning cases, jet structures do not vary significantly with refinement and the observations made with the full LES model are attributed to flow physics. For the turbulent case, grid refinement enables more disintegration and the finest grid is able to resolve smaller structures. Overall droplet sizes reduce and the increase in size along flow direction observed with full LES model minimizes with improved grid resolution. However, the level of refinement required to capture all the structures of the actual piston cooling jet at this operating condition is still unknown. LES quality metric results also improve with resolution as percentage of poor quality cells are much less than 1 % for the finest grid.

6.3. Oil jet in turbulent atmosphere

As mentioned in chapters 1, 2 and 5, atmosphere into which oil is injected in real engines is turbulent due to various moving parts within the crankcase. Reciprocating piston is found to be the dominant contributor for the flow and hence, a separate CFD analysis with RANS and piston motion, is performed to estimate pressure/velocity fluctuations within an engine cycle. Pressure results show consistency in trend with literature, validating the CFD model. Velocity components within the crankcase are quantified and the results show that the (co-axial) component, along piston axis (or oil jet axis) is significant and others can be neglected based on relative magnitude. Consequently, this leads to LES analysis of oil jet with co-axial and counter axial flows.

Preliminary estimations of momentum ratio of liquid-to-gas phase indicate significant dominance of liquid inertia and the effect of surrounding flow on jet structure until primary breakup is expected to be negligible. This is confirmed by LES analysis where both the jet structures and quantitative results show no substantial change when compared with quiescent atmosphere case. Effect on secondary breakup is unavailable from literature and this is studied with full LES model on turbulent jet for both co-axial and counter-axial cases. Results indicate that turbulent atmosphere affects secondary breakup, especially near TDC, as

the aerodynamic interactions enhance disintegration leading to reduced efficiency for gallery cooling and smaller droplets for spray cooling. The magnitude of impact is higher for the counter-flow case and it is important to perform a refinement study to identify the actual flow (droplet) properties at different piston positions.

6.4. Engineering perspective

This section gives a brief overview of how the present work contributes to better understanding of piston cooling technique within the company.

Nozzle design

From this study, at piston cooling operating conditions, the governing factor of oil jet evolution is found to be its turbulence level. Jet turbulence at the nozzle exit controls the nature of flow development, especially until occurrence of primary breakup. Post initial detachment, secondary breakup may exist and only beyond this stage, aerodynamics/atmospheric interactions affect the jet structure and ligament/droplet formation. Thus, from an engineering standpoint, the results demand for accurate designing and manufacturing of nozzles as their geometry has significant influence on the type of flow that is produced at the exit.

Pumping power

Once the remaining sub problems (from Fig. 6.1) are covered, it is possible to optimize the entire piston cooling process by identifying operating conditions that give maximum cooling at minimum pumping power and by making efficient usage of engine oil. The will eventually lead to reduction in the size of pump, reduced pressure losses between pump and oil gallery and less power consumption. On the whole, this will improve engine performance and provide higher fuel efficiencies, as the source for pump is derived from engine output power.

7

Recommendations for future work

Recommendations are divided into two sections. First, challenges faced during the present study are outlined with probable suggestions on how to improve them., in section 7.1. This is followed by recommendations for future work on spray and gallery cooling techniques in section 7.2.

7.1. Present work

Oil jet in quiescent atmosphere

Improvement in grid resolution is a standard recommendation associated with LES and this will provide better results. With respect to multi-phase flow, irrespective of the investigations performed in this study, the level of refinement required to produce grid independent solution in terms of droplet sizes still remains to be an open question and warrants the need for grid refinement studies.

However, the main limitation with the full LES model is the grid size which upon refinement demands high computational power. Hence, a better way of performing this investigation has to be identified. An effective method is to use a small, periodic domain as done in the present work (section 4.5). With this model it is possible to reconstruct the entire liquid jet as the domain can slide from nozzle exit to the TDC location. Even with fine grids, this configuration does not demand huge computational resource when compared with full LES model. Disadvantages of using this type of setup is that, the dynamic nature of the domain does not allow collection of enough number of samples required for post-processing LES results such as droplet sizes or flow rate efficiencies. Hence, its application is limited to transient or instantaneous solutions.

Actual piston cooling jet nozzles are present closer to the liner walls and the domain into which oil jet is injected is not symmetric as considered in the present study. Thus, future work can also incorporate this to study interaction of the flow/droplets with wall boundary which will demand attention towards accurate near wall modelling.

Crankcase turbulence

In this project, analysis performed to estimate crankcase flow properties are done with a simplified model where only reciprocating piston is considered as the contributor to the flow filed variation. There is no data available at the company or any material in literature that can be used for validating this CFD model. To this end it is important to optimize the model on several fronts. Firstly, the overset meshing method used for modelling piston motion has serious mass conservation issues which can be rectified only by modifying the geometry and/or simulation settings. In this study, this is dealt with by using a crankcase with inlet and outlet. Although, they represent typical blow-by and ventilation flows, lack of knowledge about their actual

configurations at the company poses a challenge for improving this model. Therefore, an optimization analysis is recommended with focus on geometry optimization, identifying best physics models, discretization techniques and other solver settings. Following this, sensitivity analyses can be performed to identify suitable grid and appropriate turbulence modelling strategy. After arriving at the best possible model, analysis can be extended to incorporate crankshaft and connecting rod rotations to quantify how these dynamics contribute to the pressure field and cross-flow velocity components within the crankcase, which will be useful for further studies on oil jet in turbulent atmosphere. Apart from overset meshing, other strategies like mesh morphing can also be adopted to perform this study.

Oil jet in turbulent atmosphere

During the present study, the initial plan for studying oil jet in turbulent atmosphere was to use the pressure fluctuations obtained from crankcase flow for an entire engine cycle, as boundary conditions in the full LES model. However, the time scales involved in simulating a complete engine cycle is significantly different from time scales associated with LES. For example, a step change in boundary condition in full LES requires 10 hours to converge and to simulate complete 720 ° CA with current time-step demands 45 days of computational time. Also, modifying the boundary pressure to higher values ($\sim$ 0.5 kPa) introduces convergence issues and demands for further reduction in CFL. Thus, only boundary velocities were modified to study the effect of co-axial and counter axial flows. It is possible to overcome this difficulty if a better method (like small domain analysis or modified domain as in section 5.2) is identified to perform grid refinement study with LES, as mentioned in previous paragraphs. Such a model will reduce the computational time drastically enabling simulation of complete engine cycle.

7.2. Future work

Spray cooling

Further studies on spray cooling will make use of droplet size results (section) obtained from the present study. To reduce computational effort, this can be performed by modelling liquid phase droplets within the Lagrangian framework in StarCCM+, where certain number of dispersed liquid particles (parcels) are solved for through the gas phase continuum. This requires CDF values of droplet size as input, given in section 4.3. It is important to note that these results are representative of the actual droplets in terms of orders of magnitude. The work should focus on accurate modelling of droplet wall interaction for which the Bai-Gosman wall impingement model is recommended. This model selects the wall interaction automatically from different options like rebound, evaporate, stick etc., based on the droplet Weber number and surface temperature. Also, selection of appropriate injector types, fluid film model, primary/secondary atomization methods are necessary and this can be achieved by thorough literature study and with some initial analyses.

Gallery cooling

Flow rate efficiency results at different piston positions, obtained from LES analysis in the present study can be used to determine the amount of oil present within the gallery. The main challenge associated with gallery cooling investigation is to combine heat transfer and sloshing flow into one dynamic simulation which may be computationally expensive. A possible way of limiting the computational time is by using moving reference frame rather than adopting mesh motion strategies. If the latter is opted for, overset method is not recommended as it will be cumbersome to identify the optimized geometry/simulation settings required to get rid of mass conservation errors. Instead, mesh morphing technique can be used.

Nozzle configuration

Based on the conclusions given in section 6.4, a study to investigate the effect of nozzle configuration on oil jets can be performed. Different properties such as nozzle diameter, shape and surface roughness, can affect the turbulence generated within the oil flow which can modify its evolution post nozzle exit and hence

impact relevant cooling parameters. This can be analysed and the study can be carried out with CFD where similar methodologies such as LES and VOF with more importance to near wall modelling, are applied.

Bibliography

[1] Liu, Z. (2010). *Overview of heavy-duty diesel engines.* In Advanced Direct Injection Combustion Engine Technologies and Development: Diesel Engines (pp. 269-288).

[2] Easter, J., Jarrett, C., Pespisa, C., Liu, Y. C., Alkidas, A. C., Guessous, L., Sangeorzan, B. P. (2014). *An area-average correlation for oil-jet cooling of automotive pistons.* Journal of Heat Transfer, 136(12), 124501.

[3] Celik. H (2018), *CFD analysis of piston cooling jets,* Master Thesis, Delft University of Technology, [Online]. Available at: TUDelft Repository, http://resolver.tudelft.nl/uuid:ae6fc82c-152d-4428-99d5-d531cc3ae6ba.

[4] Jääskeläinen Hannu (2017). *Piston cooling,* DieselNet Technology Guide. Retrieved from: https://www.dieselnet.com/tech/combustionpiston-cool.phpcrit.

[5] Liu, H. (1999). *Science and Engineering of Droplets: Fundamentals and Applications.* William Andrew.

[6] Lin, S. P., Reitz, R. D. (1998). *Drop and spray formation from a liquid jet.* Annual review of fluid mechanics, 30(1), pp 85-105.

[7] Pan, Y., Suga, K. (2006). *A numerical study on the breakup process of laminar liquid jets into a gas.* Physics of fluids, 18(5), 052101.

[8] McCarthy, M. J., Molloy, N. A. (1974). *Review of stability of liquid jets and the influence of nozzle design.* The Chemical Engineering Journal, 7(1), pp 1-20.

[9] Rayleigh, L. (1878). *On the instability of jets.* Proceedings of the London mathematical society, 1(1), pp 4-13.

[10] Rayleigh, L. (1879). *On the capillary phenomena of jets.* Proc. R. Soc. London, 29(196-199), pp 71-97.

[11] Weber, C. (1931). *Zum zerfall eines flüssigkeitsstrahles.* ZAMM-Journal of Applied Mathematics and Mechanics/Zeitschrift für Angewandte Mathematik und Mechanik, 11(2), pp 136-154.

[12] Taylor, G. (1963). *Generation of ripples by wind blowing over a viscous fluid.* Reprinted in The Scientific Papers of Sir Geoffrey Ingram Taylor, Vol. 3.

[13] Wu, P. K., Faeth, G. M. (1993). *Aerodynamic effects on primary breakup of turbulent liquids.* Atomization and Sprays, 3(3).

[14] Wu, P. K., Miranda, R. F., Faeth, G. M. (1995). *Effects of initial flow conditions on primary breakup of non-turbulent and turbulent round liquid jets.* Atomization and Sprays, 5(2).

[15] Desjardins, O., Pitsch, H. (2010). *Detailed numerical investigation of turbulent atomization of liquid jets.* Atomization and Sprays, 20(4), 311.

[16] Sallam, K., Faeth, G., Dai, Z. (1999). *Breakup of turbulent liquid jets in still gases.* In 30th Fluid Dynamics Conference (p. 3759).

[17] Phinney, R. E. (1973). *The breakup of a turbulent liquid jet in a gaseous atmosphere.* Journal of Fluid Mechanics, 60(4), pp 689-701.

[18] Reitz, R. D., Bracco, F. V. (1982). *Mechanism of atomization of a liquid jet.* Physics of Fluids, 25(10), pp 1730-1742.

[19] 17. Sallam, K. A., Dai, Z., Faeth, G. M. (1999). *Drop formation at the surface of plane turbulent liquid jets in still gases.* International journal of multiphase flow, 25(6-7), pp 1161-1180.

[20] Kowalewski, T. A. (1996).*On the separation of droplets from a liquid jet.* Fluid dynamics research, 17(3), pp 121-145.

[21] Hiroyasu, H. (1982). *The breakup of high speed jet in a high pressure gaseous atmosphere.* In Proceedings of 2nd International Conference on Liquid Atomization and Spray Systems (pp. 69-74).

[22] Grant, R. P., Middleman, S. (1966). *Newtonian jet stability.* AIChE Journal, 12(4), pp 669-678.

[23] Chigier, N., Farago, Z. (1992). *Morphological classification of disintegration of round liquid jets in a coaxial air stream.* Atomization and Sprays, 2(2).

[24] Wu, P. K., Tseng, L. K., Faeth, G. M. (1992). *Primary breakup in gas/liquid mixing layers for turbulent liquids.* Atomization and Sprays, 2(3).

[25] Sallam, K. A., Dai, Z., Faeth, G. M. (2002). *Liquid breakup at the surface of turbulent round liquid jets in still gases.* International Journal of Multiphase Flow, 28(3), pp 427-449.

[26] Sallam, K. A., Faeth, G. M. (2003). *Surface properties during primary breakup of turbulent liquid jets in still air.* AIAA journal, 41(8), pp 1514-1524.

[27] Rajendran, S., Jog, M. A., Manglik, R. M. (2012). *Experimental investigation of liquid jet breakup at low Weber number.* In ILASS Americas, 24 th Annual Conference on Liquid Atomization and Spray Systems.

[28] Skilone, D. J. (2009). *Characterization of Pre-and Post-breakup Liquid Jets.* Master Thesis, The Pennsylvania State University.

[29] Gulec, Y., 2015. *Numerical study on gasoline direct injection sprays* (Master's thesis, Izmir Institute of Technology).

[30] Mishra, Y.N., 2018. *Droplet size, concentration, and temperature mapping in sprays using SLIPI-based techniques.* Division of Combustion Physics, Department of Physics, Lund University.

[31] Moallemi, N. (2014). *Numerical and experimental investigation in the instability and the breakup of capillary water jet* (Doctoral dissertation, University of British Columbia).

[32] Levich, V. G. (1962). *Physicochemical hydrodynamics.* Prentice-Hall, Englewood Cliffs, NJ, pp 636-656.

[33] Hoyt, J. W., Taylor, J. J. (1977). *Turbulence structure in a water jet discharging in air.* Physics of Fluids, 20(10), pp S253-S257.

[34] Chen, T. F.,Davis, J. R. (1964). *Disintegration of a turbulent water jet.* Journal of the Hydraulics Division, 90(1), pp 175-206.

[35] Faeth, G. M., Hsiang, L. P., Wu, P. K. (1995). S*tructure and breakup properties of sprays.* International Journal of Multiphase Flow, 21, pp 99-127.

[36] Harmon Jr, D. B. (1955). *Drop sizes from low speed jets.* Journal of the Franklin Institute, 259(6), pp 519-522.

[37] Miesse, C. C. (1955). *Correlation of experimental data on the disintegration of liquid jets.* Industrial Engineering Chemistry, 47(9), pp 1690-1701.

[38] Anderson, J. D., Wendt, J. (1995). *Computational fluid dynamics* (Vol. 206). New York: McGraw-Hill.

[39] Versteeg, H. K., Malalasekera, W. (1995). *Computational fluid dynamics. The finite volume method.*

[40] Hirt, C. W., Nichols, B. D. (1981). *Volume of fluid (VOF) method for the dynamics of free boundaries.* Journal of computational physics, 39(1), pp 201-225.

[41] User Guide, StarCCM+, v13.02, *Chapter: Using the Volume Of Fluid (VOF) Multiphase Model*, pp 4624-4710.

[42] Darwish, M.; Moukalled, F. (2006). *Convective Schemes for Capturing Interfaces of Free-Surface Flows on Unstructured Grids.* Numerical Heat Transfer Part B.

[43] Muzaferija„ S.; Peric„ M.; Sames„ P; Schelin, T. (1998). *A two-fluid Navier-Stokes solver to simulate water entry.* Twenty-Second Symposium on Naval Hydrodynamics.

[44] Nieuwstadt, F. T., Westerweel, J., Boersma, B. J. (2016). *Turbulence: introduction to theory and applications of turbulent flows.* Springer, Ch: The Characteristics of Turbulence, pp 60-65.

[45] Pope, S.B., 2001. *Turbulent flows.*. Cambridge University press. Cornell university.

[46] El Houssami, M., 2017. *Development of a numerical and experimental framework to understand and predict the burning dynamics of porous fuel beds*, Doctoral Dessertation, The University of Edinburgh

[47] S. Hickel and S. Hulshoff (2018), *CFD3 - Large Eddy Simulation*, Lecture notes, Technical University of Delft.

[48] User Guide, StarCCM+, v13.02, *Chapter: Scale resolving simulations*, pp 3669-3671.

[49] Sagaut, Pierre (2006). *Large Eddy Simulation for Incompressible Flows* (Third ed.). Springer

[50] Leonard, A. (1974). *Energy cascade in large-eddy simulations of turbulent fluid flows.* Advances in Geophysics A. 18. pp. 237–248.

[51] Nicoud, F., Ducros, F. (1999). *Subgrid-scale stress modelling based on the square of the velocity gradient tensor.* Flow, turbulence and Combustion, 62(3), pp 183-200.

[52] Ducros, F., Nicoud, F., Poinsot, T. (1998). *Wall-adapting local eddy-viscosity models for simulations in complex geometries.* Numerical Methods for Fluid Dynamics VI, 293-299.

[53] User Guide, StarCCM+, v13.02, *Chapter: WALE Subgrid Scale model*, pp 7048.

[54] Baggett, J. S., Jimenez, J., Kravchenko, A. G. (1997). *Resolution requirements in large-eddy simulations of shear flows.* Annual research briefs, pp 51-66.

[55] Celik, I. B., Cehreli, Z. N., Yavuz, I. (2005). *Index of resolution quality for large eddy simulations.* Journal of fluids engineering, 127(5), 949-958.

[56] Moghe, S. S., Janowiak, S. M. (2016, October). *Large Eddy Simulation of Cylindrical Jet Break-Up and Correlation of Simulation Results With Experimental Data.* In ASME 2016 Internal Combustion Engine Division Fall Technical Conference (pp. V001T06A008-V001T06A008).

[57] Jarrin, N., Benhamadouche, S., Laurence, D., Prosser, R. (2006). *A synthetic-eddy-method for generating inflow conditions for large-eddy simulations.* International Journal of Heat and Fluid Flow, 27(4), 585-593.

[58] Xiao, F., Dianat, M., McGuirk, J. J. (2017). *An LES turbulent inflow generator using a recycling and rescaling method.* Flow, turbulence and combustion, 98(3), 663-695.

[59] User Guide, StarCCM+, v13.02, *Chapter: Synthetic eddy method*, pp 3689-3693

[60] Jääskeläinen, H. (2012). *Crankcase Ventilation.* DieselNet Technology Guide. [Online] Available at: https://www.dieselnet.com/tech/enginecrank.php.

[61] Ranganathan, R. P. (1999). *Engine crankcase pumping flow model.* SAE transactions, pp 310-341.

[62] Edelbauer, W., Diemath, A., Kratochwill, H., Brenn, G. (2009). *Simulation of the ventilation losses in the crankcase of an internal combustion engine.* Progress in Computational Fluid Dynamics, an International Journal, 10(1), pp 1-18.

[63] Fogliarino, M. (2014). *Crankcase pressure control in an internal combustion engine*: GT-Power simulation. Master Thesis. University of Windsor, Canada.

[64] Arisawa, H., Nishimura, M., Watanabe, H., Ueshima, A., Arima, K., Yamasaki, A. (2009). *Study on Similarity of Pumping Flow in Engine Crankcase* (No. 2009-32-0051). SAE Technical Paper.

[65] Lakshminarayanan, P. A., Senthilkumar, P. K. (2013). *Blowby, Breathing and Oil Slobbering from Small Engines* (No. 2013-26-0123). SAE Technical Paper.

[66] S. Hickel (2017), *CFD 1 - Introduction to CFD*, Lecture notes, Technical University of Delft.

[67] User Guide, StarCCM+, v13.02, *Chapter: Reynolds-Averaged Navier-Stokes (RANS) Turbulence models*, pp 3581.

[68] Wilcox, D. C. (2008). *Formulation of the k-ω turbulence model revisited.* AIAA journal, 46(11), 2823-2838.

[69] Menter, F. R. (1994). *Two-equation eddy-viscosity turbulence models for engineering applications.* AIAA journal, 32(8), 1598-1605.

[70] User Guide, StarCCM+, v13.02, *Chapter: Wall treatment*, pp 3694.

[71] *Understanding overset meshes and interface options.* [Online]. Available at: https://thesteveportal.plm.automation.siemens.com/articles/enUS/FAQ/Understanding-overset-mesh-interface-options

[72] Chan, W., Gomez, R., Rogers, S., Buning, P. (2002). *Best practices in overset grid generation.* In 32nd AIAA Fluid Dynamics Conference and Exhibit, pp. 3191.

[73] Tramel, R., Nichols, R., Tramel, R., Nichols, R. (1997,). *A highly efficient numerical method for overset-mesh moving-body problems.* In 13th Computational Fluid Dynamics Conference, p. 2040.

[74] Berton, A., D'Orrico, F., Sideri, M. (2017). *Overset grids for fluid dynamics analysis of internal combustion engines.* Energy Procedia, 126, 979-986.

[75] Nasif, G. G. (2014). *CFD Simulation of Oil Jets with Application to Piston Cooling.*Doctoral Dessertation. University of Windsor, Canada.

[76] Mayer, W. O. H., Branam, R. (2004). *Atomization characteristics on the surface of a round liquid jet.* Experiments in fluids, 36(4), pp 528-539.

[77] Xiao, F., Dianat, M., McGuirk, J. J. (2014). *LES of turbulent liquid jet primary breakup in turbulent coaxial air flow.* International Journal of Multiphase Flow, 60, pp 103-118.

[78] Kim, D., Desjardins, O., Herrmann, M., Moin, P. (2007, May). *The primary breakup of a round liquid jet by a coaxial flow of gas.* In ILASS Americas 20th annual conference on liquid atomization and spray systems (Vol. 20).

[79] Dimela, N. (2017). *Numerical simulations of primary break-up in two-phase* flows. Doctoral Dessertation. Imperial College London, London.

[80] Wu, P. K., Kirkendall, K. A., Fuller, R. P., Nejad, A. S. (1997). *Breakup processes of liquid jets in subsonic crossflows.* Journal of Propulsion and Power, 13(1), pp 64-73.

[81] Mazallon, J., Dai, Z., Faeth, G. (1998, January). *Aerodynamic primary breakup at the surface of nonturbulent round liquid jets in crossflow*. In 36th AIAA Aerospace Sciences Meeting and Exhibit (p. 716).

[82] Pai, M. G., Bermejo-Moreno, I., Desjardins, O., Pitsch, H. (2009). *Role of Weber number in primary breakup of turbulent liquid jets in crossflow*. Center for Turbulence Research Annual Research Briefs 2009, 145-158.

[83] Sallam, K. A., Aalburg, C., Faeth, G. M. (2004). *Breakup of round nonturbulent liquid jets in gaseous crossflow*. AIAA journal, 42(12), pp 2529-2540.

[84] User Guide, StarCCM+, v13.02, *Chapter: Multiphase models*, pp 4063-4710.

[85] A. van Veen, "15-469 (*Flow efficiency measurement*)," DAF Library, 2015.

[86] Herrmann, M. (2011). *On simulating primary atomization using the refined level set grid method*. Atomization and Sprays, 21(4).

[87] Salim, S. M., Cheah, S. (2009). *Wall Y strategy for dealing with wall-bounded turbulent flows*. In Proceedings of the international multiconference of engineers and computer scientists (Vol. 2, pp. 2165-2170). Hong Kong.

[88] Munson, B. R., Okiishi, T. H., Huebsch, W. W., Rothmayer, A. P. (2013). *Fluid mechanics*. Singapore: Wiley.

A

Scalability results

This analysis is performed with oil jet at 7 L/min as it requires the maximum computational time. The simulation is run with different number of cores. Current computational facility at DAF consists of 476 cores and the simulation appears to be scalable even at full load. Thus, all LES cases are run with the same setting.

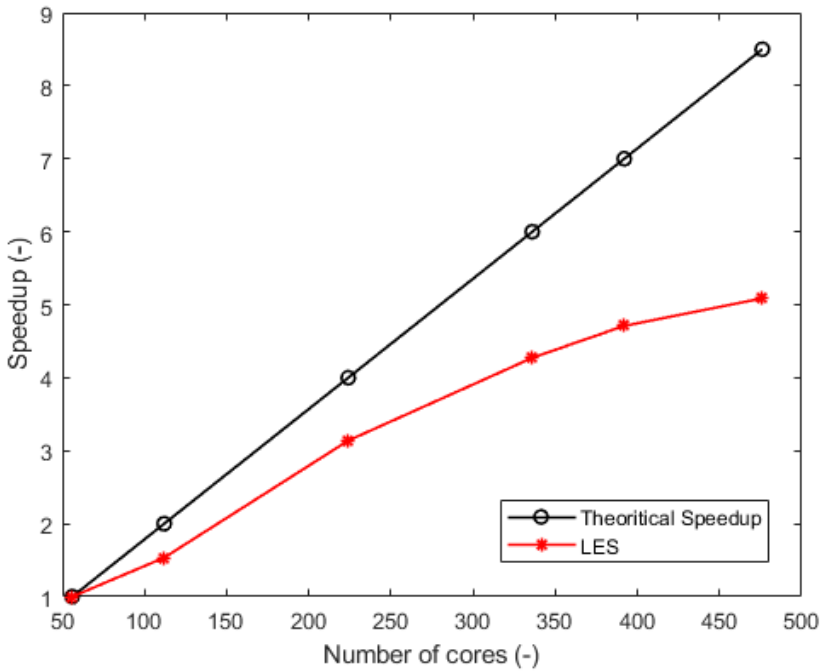

Figure A.1: Precursor simulation geometry [3]

B

Precursor simulation

A precursor simulation with RANS is used to obtain inlet boundary conditions for LES analysis. The model exemplifies flow within an infinitely long pipe and the aim is to obtain fully developed turbulent flow within the domain. The geometry used is a simple cylinder representing the nozzle used for piston cooling (Fig. B.1). Length of the domain is maintained at 5d and periodic boundary conditions are used as shown in the figure.

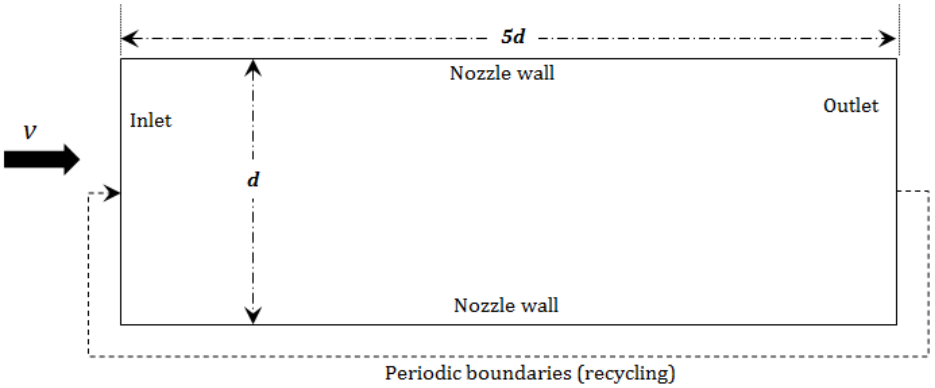

Figure B.1: Precursor simulation geometry [3]

Structured mesh with refinement near the nozzle region is generated as shown in Fig.C.4. Mass flow inlet is specified and Realizable k-epsilon turbulence modelling strategy is used. Results such as velocity profile, turbulence intensity and turbulent length scale are exported to the LES model and values of Kolmogorov and Taylor micro scales are used for LES grid construction.

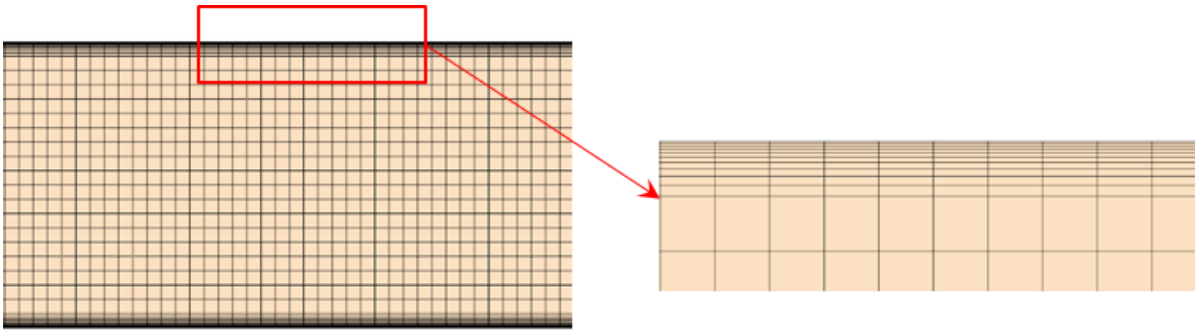

Figure B.2: Mesh schematic used for precursor simulation

C

LES Quality results

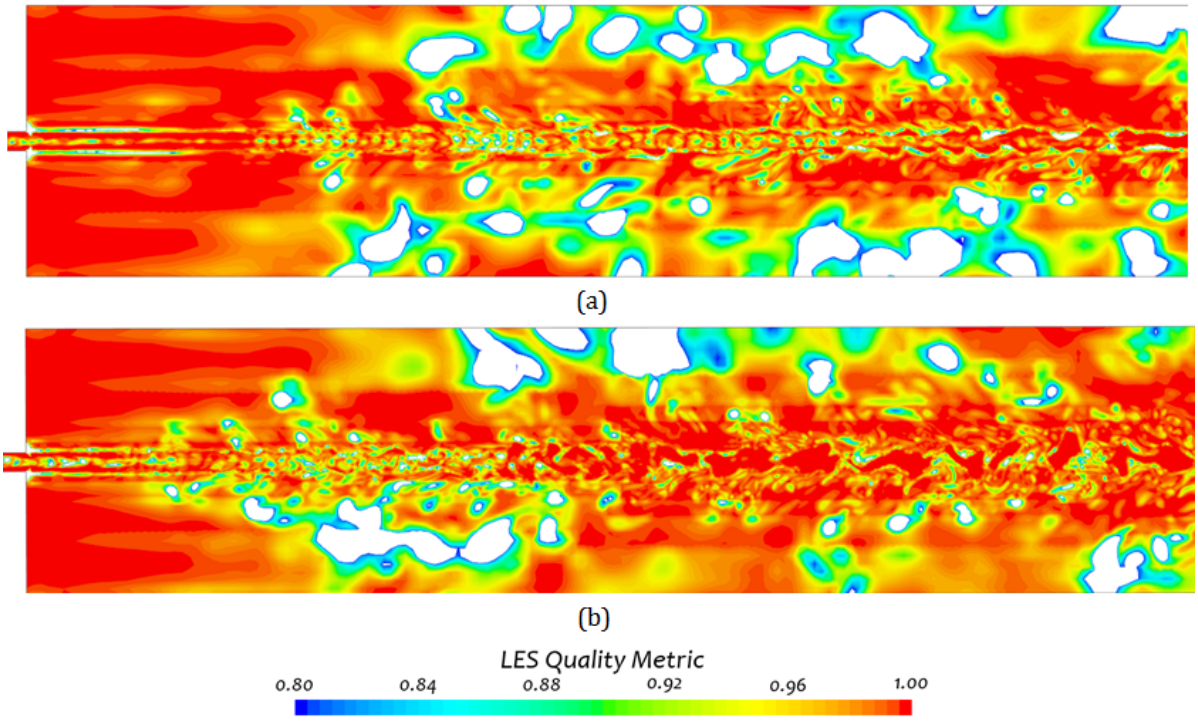

Figure C.1: LES quality metric (sufficient condition) for oil jet at (a) 3 L/min and (b) 4 L/min

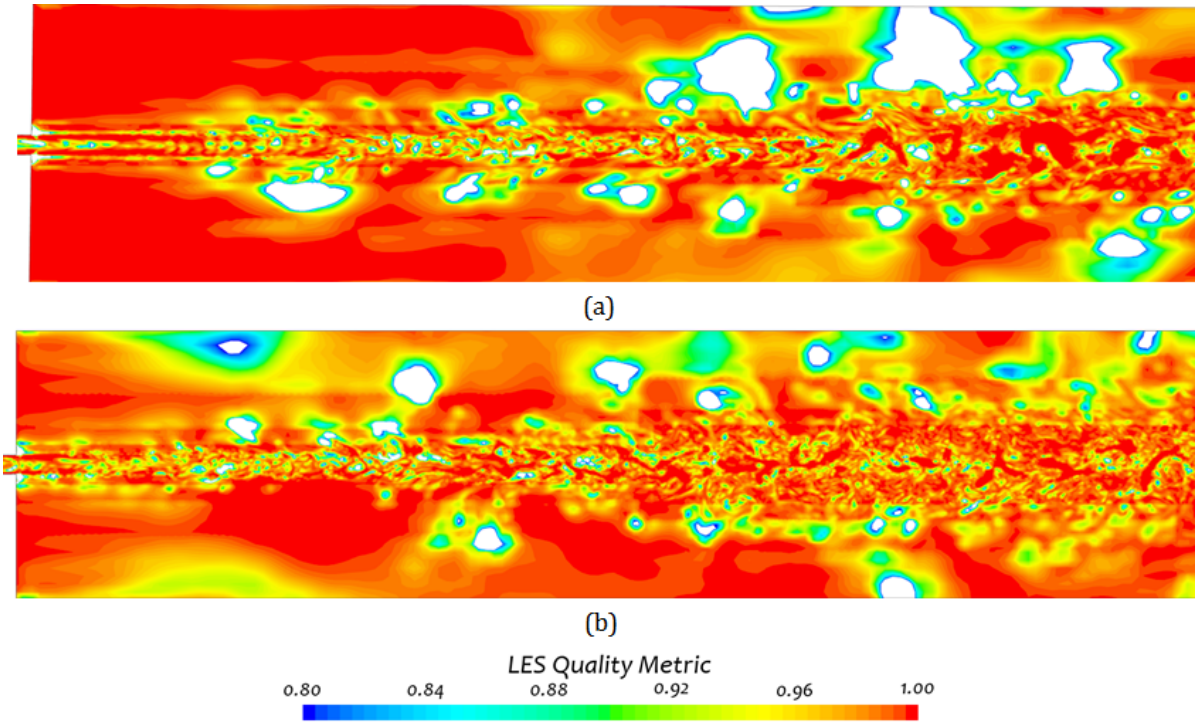

Figure C.2: LES quality metric (sufficient condition) for oil jet at (a) 5 L/min and (b) 6 L/min

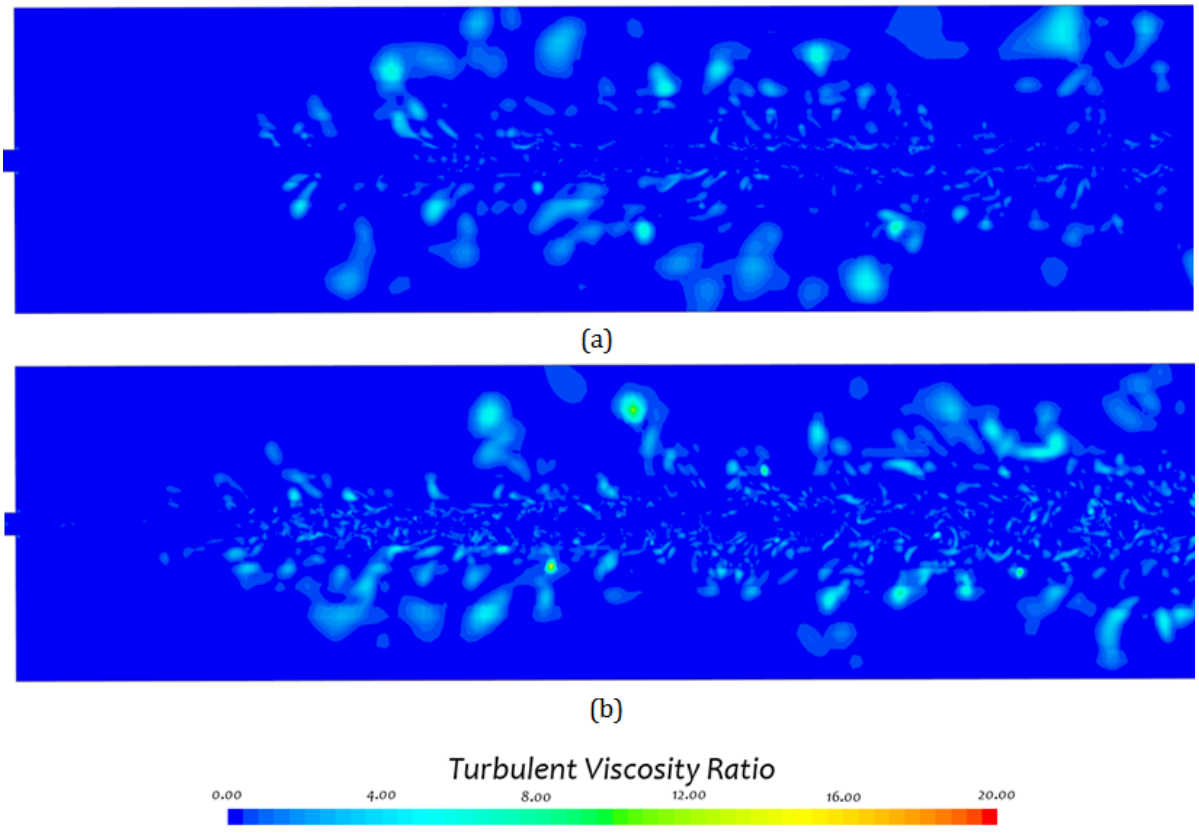

Figure C.3: Turbulent viscosity ratio (necessary condition) for oil jet at (a) 3 L/min and (b) 4 L/min

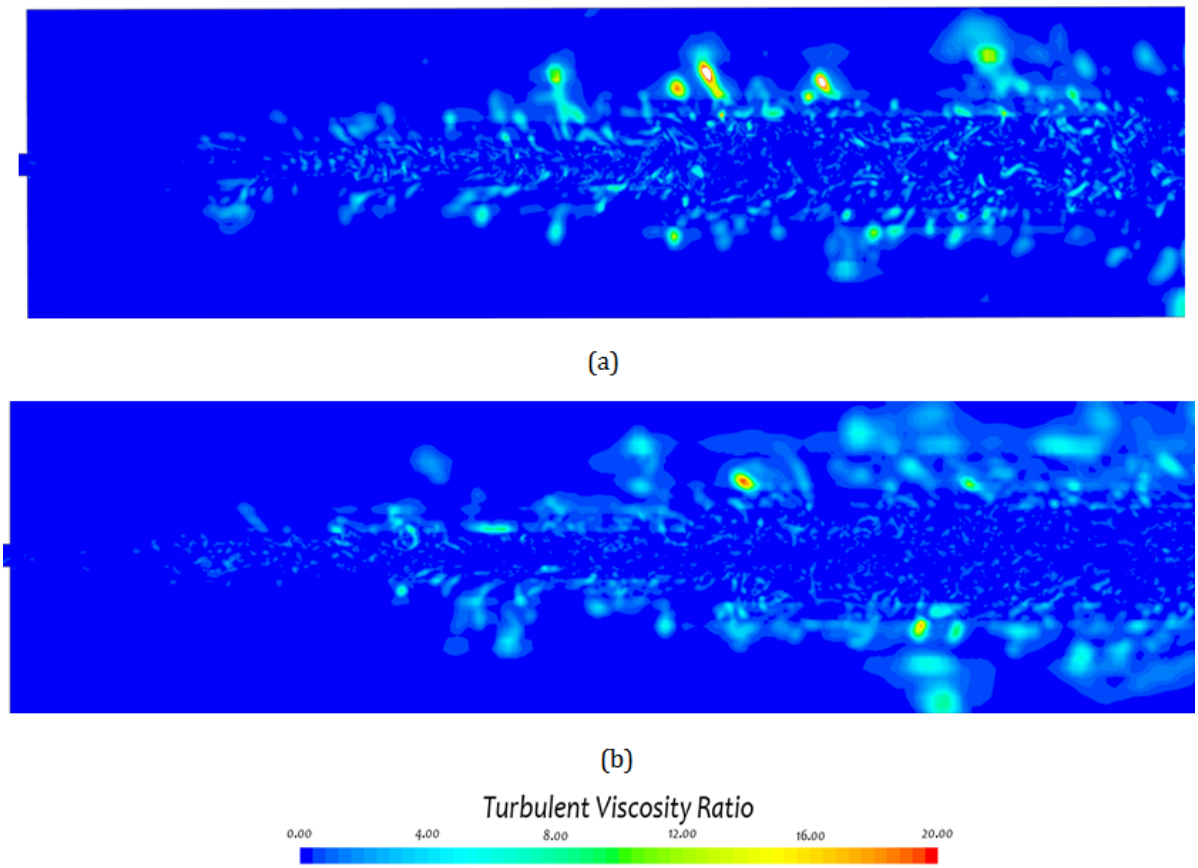

Figure C.4: Turbulent viscosity ratio (necessary condition) for oil jet at (a) 5 L/min and (b) 6 L/min

D

Summary of Jet characteristics

Jet structure of all the tested cases can be referred from Fig. 4.2.

3 L/min

	BDC	**S/4**	**S/2**	**3S/4**	**TDC**
Jet velocity, in m/s	6.04(±0.07)	5.93(±0.09)	5.91(±0.05)	5.89(±0.04)	5.79(±0.10)
Jet appearance/ properties	Intact, surface waves	Intact, surface waves, non-axisymmetric	Intact, short wavelength and large amplitude waves	Intact, short wavelength and large amplitude waves	Intact, short wavelength and large amplitude waves
Flow rate efficiency	100(±0.45)	100(±0.61)	100(±0.80)	99(±0.92)	99(±0.94)

Table D.1: Characteristics of the laminar jet, at 3 L/min

4 L/min

	BDC	**S/4**	**S/2**	**3S/4**	**TDC**
Jet velocity, in m/s	8.31(±0.1)	8.26(±0.15)	8.23(±0.15)	8.13(±0.09)	8.00(±0.2)
Jet appearance/ properties	Intact, short wavelength and large amplitude waves	Intact, short wavelength and large amplitude waves	Intact, pre-breakup, protruding ligaments, chaotic	Intact, pre-breakup, protruding ligaments, chaotic	Primary breakup and protruding ligaments
Flow rate efficiency	99.5(±0.95)	99(±0.75)	98(±0.93)	97(±0.97)	97(±1.52)

Table D.2: Characteristics of transitioning jet, at 4 L/min

5 L/min

	BDC	**S/4**	**S/2**	**3S/4**	**TDC**
Jet velocity, in m/s	10.65(±0.21)	10.59(±0.15)	10.54(±0.15)	10.07(±0.27)	9.79(±0.05)
Jet appearance/ properties	Intact, short wavelength and large amplitude waves	Intact, pre-breakup, protruding ligaments, chaotic	Intact, pre-breakup, protruding ligaments, chaotic	Intact, pre-breakup, protruding ligaments, chaotic	Primary breakup ligaments few drops
Flow rate efficiency	99(±0.1)	96.5(±0.55)	94(±0.81)	92(±1.01)	90(±1.7)
Mean drop size	-	-	-	-	0.66 x 10^{-3} m

Table D.3: Characteristics of transitioning jet, at 5 L/min

6 L/min

	BDC	**S/4**	**S/2**	**3S/4**	**TDC**
Jet velocity, in m/s	12.66(±0.08)	14.59(±0.07)	12.51(±0.08)	12.45(±0.08)	12.38(±0.09)
Jet appearance/ properties	Disturbed, wavy, pre-breakup	pre-breakup, protruding ligaments, chaotic	pre-breakup, protruding ligaments, chaotic	pre-breakup, protruding ligaments, surface breakup	Primary breakup ligaments and few drops
Flow rate efficiency	98(±0.12)	97.2(±0.28)	93.8(±0.76)	89.5(±0.89)	83.8(±1.25)
Mean drop size	-	-	-	-	0.70 x 10^{-3} m (±0.02) (Fig. 4.8)

Table D.4: Characteristics of transitioning jet, at 6 L/min

7 L/min

	BDC	**S/4**	**S/2**	**3S/4**	**TDC**
Jet velocity, in m/s	14.68(±0.08)	14.62(±0.07)	14.56(±0.08)	14.51(±0.08)	14.44(±0.08)
Jet appearance/ properties	Disturbed, wavy, primary breakup	Post-breakup, ligaments, droplets	Post-breakup, ligaments, droplets	Post-breakup, complete disintegration	Post-breakup, ligaments more droplets
Flow rate efficiency	97(±0.13)	87.7(±0.37)	82.9(±0.57)	80.2(±0.62)	76.5(±0.71)
Mean drop size	0.34 x 10^{-3} m (±0.04)	0.35 x 10^{-3} m (±0.08)	0.47 x 10^{-3} m (±0.08)	0.52 x 10^{-3} m (±0.09)	0.60 x 10^{-3} m (±0.09)
Dropsize distribution	Fig. 4.9	Fig. 4.10	Fig. 4.11	Fig. 4.12	Fig. 4.13

Table D.5: Characteristics of turbulent jet, at 7 L/min